UNIVERSITY COLLEGE LONDON

Faculty of Mathematics and Physical Sciences

Department of Physics & Astronomy

SHOCK CHEMISTRY IN STAR FORMING ENVIRONMENTS

Thesis submitted for the Degree of Doctor of Philosophy of the University of London

by

Jonathan Holdship

Supervisors:

Prof. Serena Vita

Prof. Jonathan Rawlings

Examiners:

Dr. Jennifer Hatchell

Dr. Jeremy Yates

October 31, 2017

For Kat, who would consider this enough.

I, Jonathan Holdship, confirm that the work presented in this thesis is my own. Where information has been derived from other sources, I confirm that this has been indicated in the thesis.

Abstract

Molecules are abundant in many astrophysical environments. The observation of these molecules and the modelling of the chemistry that leads to their formation is a powerful tool for improving our understanding of the regions in which they are found. In this thesis, a chemical model is developed and applied to astrophysical shocks to understand a number of processes in star forming regions. Shocks often result in discontinuous changes in the temperature and density of the gases they affect. The turbulent fragmentation theory of star formation suggests that such shocks are responsible for the over-densities that lead to the formation and collapse of prestellar cores from molecular clouds. Focusing on low mass objects, a chemical model of prestellar cores formed through shocks is developed and compared to models of similarly dense gas formed through gravitational freefall. Observational predictions of shock induced differences in the chemistry of these cores are reported and compared to the literature.

Not only are molecules abundant in the gas phase but they are also observed in solid state, frozen onto the surfaces of interstellar dust grains. This freeze out process is efficient in molecular clouds but the composition of these ices is poorly constrained for all but the most abundant molecules. Shocks represent a powerful tool to study these ices as they not only change the gas properties but can also sputter and shatter dust grains releasing frozen molecules into the gas phase.

Observations of sulfur-bearing molecules in a protostellar outflow, L1157-B1, are presented and analysed, giving an overview of the sulfur content of the recently shocked gas. The abundances of important sulfur molecules are then compared to chemical models of C-type shocks in an attempt to constrain the main solid state form of sulfur before the shock and the shock properties of the observed outflow.

Acknowledgements

First of all, I would like to thank Serena Viti for her support and advice. If the completion of this thesis has gone smoothly, she played a huge role in that. I've been given the leeway to focus my own work and guidance when I've lost direction and for that I'm very grateful. Beyond my direct supervision, I want to thank Izaskun Jimenez-Serra, Claudio Codella and Bertrand Lefloch for their help with much of the work in this thesis. I've covered a lot of topics and that wouldn't have been possible without their expertise.

Thank you to my family for their encouragement every step of the way to completing my PhD. From Mum teaching me how to write, to Dad trying to make me love Maths, I've always felt what I'm doing was worthwhile. Thank you to my friends, who certainly didn't help this thesis get finished but did make my PhD a fantastic experience.

Finally, I want to thank Kat for her love and support throughout the past few years. Every day of it has been great and she has even made writing up unbelievably stress free.

When you look up out at night,
You're fortunate enough to drink in a vista,
One hundred billion flares display a glowing history

Redshift - Enter Shikari

Contents

This page was intentionally left blank

List of Figures

This page was intentionally left blank

List of Tables

Chapter 1

Introduction

1.1 Overview

It is popularly thought that the expanse between stars is empty, a near perfect vacuum. This is not the case. Astronomers observe gas and dust in a variety of conditions and the field of astrochemistry has arisen to study the chemistry that appears to take place throughout the galaxy. The matter between stellar systems is known as the Interstellar Medium (ISM) and ranges from the very diffuse (particle density of $\sim 10^2\,\mathrm{cm}^{-3}$) to the much denser gas of protostellar objects ($\sim 10^{10}\,\mathrm{cm}^{-3}$). Table 1.1 is an adaptation from Williams and Viti (2013) giving a summary of the components of the ISM. These components are produced by a complex interplay of gravity, hydrodynamics and radiation as the gas interacts and stars form, evolve and explode.

Table 1.1: Regions in the ISM and their typical densities and temperatures taken from Williams and Viti (2013).

Region	n_H / cm^{-3}	T / K
Coronal gas	$<10^{-2}$	5×10^5
HII regions	>100	1×10^4
Diffuse gas	100 - 300	70
Molecular clouds	10^4	10
Prestellar cores	10^5-10^6	10 - 30
Star-forming regions	10^7 - 10^8	100 - 300
Protoplanetary disks	10^4(outer)-10^{10}(inner)	10(outer) - 500 (inner)
Envelopes of evolved stars	10^{10}	2000 - 3500

Since the discovery of the first molecules (CH, CH^+ and CN) in space (Merrill et al. 1937), it has become clear that studying these cold astrophysical regions is dependent on the observation of molecules and understanding the chemistry controlling them. From CO, which traces the column density of cold molecular gas to SiO, a clear indicator of shocks, molecular observations give great insight into the regions in which they are detected.

It is the radiative properties and varied chemistry of these species that enable their use as molecular tracers. CO is particularly useful due to two features: a near constant abundance of 10^{-4} relative to H_2 Liu et al. (2013) and a ground state rotational transition with an excitation temperature of only 5.5 K. This means it can be observed easily in cold gas and gives a good estimate of the gas column density. CS is also a useful species due to its radiative properties. Most transitions have a high critical density, $4 \times 10^5\,\mathrm{cm}^{-3}$ to $7 \times 10^7\,\mathrm{cm}^{-3}$ (Gómez-Ruiz et al. 2015), and so upper states are not well populated at low densities. See Section 1.6.1 for a discussion of critical densities.

As well as providing tracers for specific physical conditions, molecules offer another route to understanding observed regions. SiO is a tracer that is useful because of its chemistry; it forms rapidly in the gas-phase if atomic silicon is available. A large amount of silicon is locked in dust (Henning 2010) but a strong shock can sputter this silicon making it available to form SiO (Jiménez-Serra et al. 2008). Thus, the observation of a large amount of SiO in the gas-phase is indicative of shocked gas.

The abundance of any chemical species is a product of all the chemical reactions that create or destroy that species and the efficiency of these reactions is a function of the physical characteristics of the region. Chemistry is also time-dependent; unless equilibrium can be reached chemical abundances are dependent on the history of the gas as well as the current physical conditions. As a result, detailed chemical models coupled with physical models can provide answers to insights into processes like star formation.

The following sections of this introduction give an overview of the chemistry and physics that is most relevant to the work presented in the thesis.

1.2 Gas-Phase Chemistry

Gas in the ISM consists almost entirely of neutral or molecular hydrogen with other elements present in only small fractions of the hydrogen abundance, the most abundant being: He (0.085); C (2.7×10^{-4}); O(4.9×10^{-4}); N(6.8×10^{-5})(Asplund et al. 2009).

Nevertheless, given enough time and the right physical conditions, a wealth of molecules can be generated from this gas. However, since many reactions between neutral species have energetic barriers, some driver is required to initiate chemistry.

In diffuse clouds, UV light is a major driver. UV photons typically have energies hν<13.6 eV as hydrogen can be ionized by photons with higher energies and so flux from those photons drops rapidly with distance from stars as these photons are efficiently absorbed by hydrogen. As a result, any element with an ionization potential lower than 13.6 eV is likely to experience some degree of ionization. C, S and Cl fall into this category and the ion-neutral reactions that follow are an important driver of chemistry in diffuse clouds. Take for example C:

$$C + h\nu \rightarrow C^+ \tag{1.1}$$

$$C^+ + H_2 \rightarrow CH_2^+ + h\nu \tag{1.2}$$

The first reaction is efficient as C has an ionization potential of 11.3 eV and the second is radiative association reaction with a barrier of only 23 K. CH_2^+ is then able to react efficiently with the three most abundant species in diffuse clouds, H_2, H, and e^-, in a series of reactions that create radicals. For example,

$$CH_2^+ + e^- \rightarrow CH + H \tag{1.3}$$

$$CH_2^+ + H_2 \rightarrow CH_3^+ + H \tag{1.4}$$

$$CH_3^+ + e^- \rightarrow CH_2 + H \tag{1.5}$$

These radicals are able to go on to react much more efficiently than most neutral species leading to astrophysically relevant species such as CO through the reaction of CH and O.

As the density of an absorbing species in a gas increases, the likelihood of a photon traveling through the gas without absorption decreases. Regions in which it is unlikely a photon can travel without absorption are referred to as optically thick. Dark molecular clouds are an example of this and in such clouds UV photons will not be able to penetrate very far into the gas without being absorbed. As a result, chemistry driven by UV radiation is not efficient due to the lack of high energy photons. In these regions, cosmic rays (CRs) drive much of the chemistry. A CR is likely to have energy of the order of a MeV and

therefore can cause multiple ionization events, each requiring ∼10 eV (Williams and Viti 2013), without much effect on the CR. As a result, the effect of CRs is not strongly depth dependent even in very dense clouds. The high energy also means that CRs can ionize species that UV light cannot such as H, He and H_2. The ionization of H_2 is important because it leads to the reaction.

$$H_2^+ + H_2 \rightarrow H_3^+ + H \tag{1.6}$$

and H_3^+ is a highly reactive species that forms many important species including OH^+ and HCO^+. From here, ever larger species can be produced though models show that species with more than a few heavy atoms (C, O, N etc.) are not produced in notable abundances in the gas-phase (Williams and Viti 2013). For the production of these molecules, formation on dust grains is typically invoked.

1.3 Dust and Surface Chemistry

Dust in the form of carbonaceous and silicate material as well as large carbon molecules (PAHs) is present in interstellar gas at a relatively fixed gas to dust mass ratio of 100:1 (Savage and Mathis 1979). Dust is vital to chemistry in many ways, the first of which is that dust is responsible for UV attenuation, reducing the efficiency of the UV driven chemistry discussed above. Secondly, the dust grains provide surfaces on which reactions can take place, often catalyzing reactions.

Dust grain surfaces are not bare. At temperatures typical for molecular clouds (∼10 K) atoms, molecules and ions colliding with the grain surfaces are likely to be adsorbed either physically or chemically. As a result, dust grains build up "ice mantles" over time. The main constituents of these ice mantles are H_2O, CO and CO_2 along with hydrogenated molecules such as HCO, H_2CO and CH_3OH. These likely form on the grain as O, C and CO freeze and react with hydrogen atoms which can diffuse rapidly around the dust atoms (Watanabe and Kouchi 2002). In denser clouds, freeze out is more efficient. In these cases, not only are mixed ices of the above molecules observed but it is expected from models, experiments and observations that other molecular species form single layer surfaces over the ices.

Chemistry on the grains is understood to progress through three main mechanisms:

- Eley-Rideal - A gas-phase molecule collides with an adsorbed molecule causing a reaction.
- Langmuir-Hinshelwood - Both species are adsorbed and diffuse across the grain surface until they can react.
- Harris-Kasemo - A gas-phase molecule adsorbs to the surface but is able to move quickly before thermalizing. In this time, it may meet another adsorbate and react.

These processes are important as they allow more complex species to be formed in the ices than would be possible in the cold gas-phase. It is important to note that the relative importance of these processes is not well known in general. However, the Langmuir-Hinshelwood mechanism is the most well studied (see review by Herbst and van Dishoeck 2009 and references within).

One particularly vital surface chemistry process is the formation of molecular hydrogen. The formation rate of molecular hydrogen is well constrained by observations (Jura 1975; Gry et al. 2002) and higher than the expected rate of gas-phase formation (Vidali 2013). This is because the formation of H_2 can result in the produced molecule being excited to a vibrational level of the electronic ground state that is above the dissociation limit. Due to the low densities in the ISM and even dark clouds, this is unlikely to be stabilised. As a result, grain surface formation in which the excess energy from the reaction can be transferred to the grain is invoked. This is necessary as the estimated rate of H_2 formation is so high that almost every hydrogen atom arriving at a grain surface should leave as part of a molecule (Duley and Williams 1986).

The energy released by H_2 formation does not disappear. In fact, there are another set of grain surface chemical processes that are important in the ISM. Energy released in reactions such as H_2 formation and energy deposited by UV photons or cosmic rays can all provide enough energy to an adsorbed molecule to release it from the grain and into the gas-phase (See Roberts et al. 2007 and references within). These desorption processes are important because without them, chemical models predict almost complete depletion of molecules from the gas-phase in dense clouds, whereas observations show abundances of many species are maintained (Willacy and Langer 2000).

There is a lot of uncertainty in our understanding of the above processes but laboratory experiments of chemistry on interstellar ice analogues are making headway (eg. Ioppolo et al. 2008). Of course, they are themselves subject to uncertainties in how we apply results

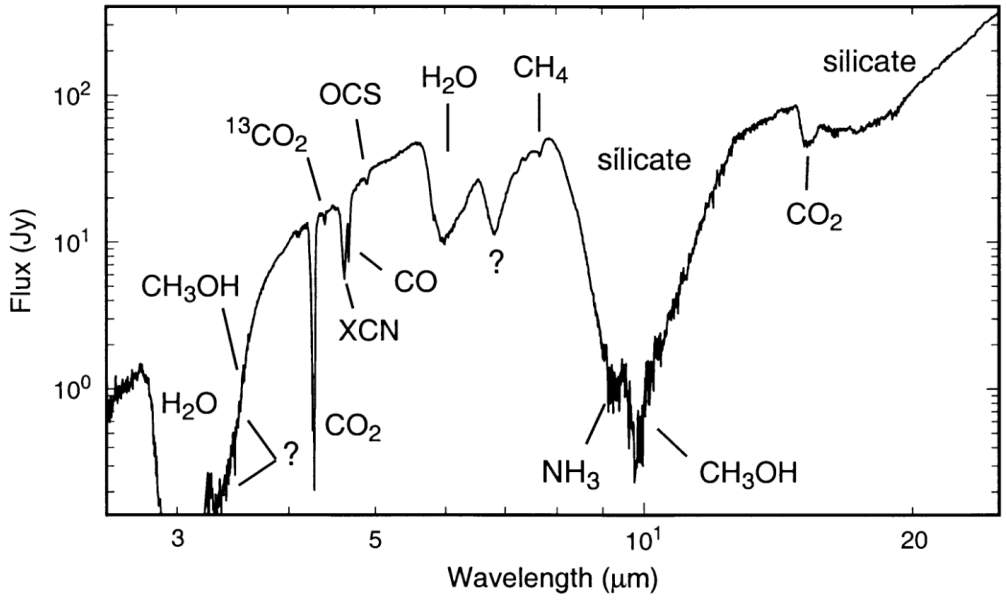

Figure 1.1: Absorption spectrum towards W33A, an embedded protostar taken from Gibb et al. (2000).

in laboratory conditions to interstellar dust. This is exacerbated by the fact the contents of ice mantles are difficult to observe and thus it is hard to constrain the chemistry. This is particularly problematic in the case of species that are attached to the mantle surface in small abundances. However, with sufficient dust between a micrometer source and the observer, the ices can be seen in absorption. Figure 1.1 shows such an observation towards the young stellar object W33A which is embedded in a dusty envelope and shows clear absorption.

Beyond this, less direct methods must be used to investigate the contents of ice mantles in interstellar environments. In particular, observations of regions with disrupted grain mantles including shocked regions where ices are sputtered and hot regions where sublimation occurs can provide constrains on grain surface abundances. In these cases, the much more well constrained gas chemistry can be used to calculate what must be entering the gas from the ices and thus what was in the ices before the disruption. For example, Belloche et al. (2017) found that gas-phase abundances of CH_3NCO around a high mass protostar could only be explained by their models if large amounts of HNCO was produced

on the grains.

1.4 Molecular Clouds & Star Formation

1.4.1 Clouds and Cores

Molecular clouds are dense ($10^4\,\mathrm{cm}^{-3}$), cold (10 K) regions of the ISM ranging from dark clouds of ∼1 pc containing anything from 5 to 500 solar masses to giant molecular cloud complexes of ∼100 pc which contain ∼10^6 $M_\odot$. They were originally detected by their visual extinction (Lynds 1962), by counting stars and noting deviations below the average. This is still a common procedure, though done with extinction in the near-infrared (eg. Lombardi et al. 2006). Despite this apparent lack of stars, molecular clouds are actually the location in which stars form.

Molecular clouds are turbulent and magnetized (Elmegreen and Scalo 2004) as well as extremely inhomogeneous. Though often treated in chemical models as clouds of constant density, molecular clouds are observed (André et al. 2010; Hacar et al. 2013) to contain substructure, largely in the form of dense filaments with radii of ∼ 0.1 pc. Stars are observed to form along these filaments (Konyves et al. 2015) and there is evidence star forming clusters are located at the intersections of filaments from observations (Schneider et al. 2012) and models (Myers 2011).

Regardless of how these structures are formed, they must be gravitationally unstable in order for star formation to proceed. A simple diagnostic for this is to combine the mass of a critical Bonnor-Ebert sphere (Bonnor 1956) with the critical mass of a magnetically supported core (McKee 1989):

$$M_{crit} = \frac{1.18 C_s^4}{\sqrt{G^3 P_0}} + 2k_\phi \phi \tag{1.7}$$

where C_s is the sound speed, P_0 the surface pressure, ϕ is the magnetic flux and G is the gravitation constant. k_ϕ is a constant with the value $1.925 \times 10^{15}\,\mathrm{g\,cm^{-1}\,\mu G}$ based on work by Mouschovias and Spitzer (1976). This gives a measure of the required mass for an object to have a larger gravitational force than the combined thermal and magnetic pressure, though it does neglect turbulent support. Despite increasing the critical mass in the above equation, MHD models show that both turbulence and magnetic fields lead to the formation of sheets and filaments within molecular clouds even if gravity is neglected

(Matsumoto et al. 2015). It therefore appears that these factors both hinder the collapse of prestellar cores and help their initial formation by creating structures of sufficient density to collapse.

Cores are not necessarily the precursors to single stars, as theoretically it is reasonable to assume a large core can fragment as it collapses (Dyson and Williams 1980). However, observations (eg. André et al. 2010) of the distribution function of core masses, the core mass function (CMF) are remarkably similar to the initial mass function (IMF), the distribution function of stellar masses at the moment they reach the main sequence (Geha et al. 2013). As a result, many authors postulate a simple relationship between the mass of starless cores and the mass of the stars they produce such as a one-to-one relationship André et al. (2010).

1.4.2 Core Evolution

Initially, bound cores collapse isothermally and do so as long as the opacity of the gas is low. Over time the density of the gas increases and the gas starts to heat up as the opacity likewise increases. During this short phase, the core ceases to collapse as the rising temperature leads to an increase in internal pressure. This stage is known as the first hydrostatic core and has not yet been firmly detected (Enoch et al. 2010). Once the temperature reaches 2000 K, the molecular hydrogen in the centre of the core dissociates changing the specific heat of the gas and allowing it to continue to collapse as a protostar (Larson 1969).

At this point, a young stellar object evolves through a sequence of evolutionary stages and are referred to as Class 0, I, II or III protostars depending on their observational characteristics and assumed stage. Class 0 objects are still deeply embedded in an envelope of gas from which they accrete, so much so that their SEDs often resemble a simple 30 K blackbody. At this stage the envelope has more mass than the protostar (Barsony 1994). Accretion onto the protostar leads to Class I objects with reduced envelopes, it is also believed to be the driver behind the outflows observed from Class 0 and I protostars (see Section 1.4.3). Over time, the envelope is cleared and a thick disc is formed. Objects with large discs and weak outflows are Class II objects and Class III objects are those that have mostly cleared their discs and have lost their outflows. Both Class II and III objects are visible at optical frequencies due to the clearing of the envelope (Lada 1987). At this point the protostar will continue to evolve onto the main sequence where it begins to fuse

hydrogen at its core.

1.4.3 Outflows

In the early stages of their evolution, young stellar objects are observed to drive jets and outflows though the precise driving mechanism is unknown (Reiter et al. 2017). These are bipolar streams of gas along the rotation axis of the protostar that can be differentiated by their opening angles and speeds. Jets have speeds of order $100\,\mathrm{km\,s^{-1}}$ and opening angles $\sim5^\circ$ whereas outflows are slower ($\sim10\,\mathrm{km\,s^{-1}}$) and driven over wider angles. Outflows are molecular in nature and observed in tracers such as CO (Gueth et al. 1996; Hatchell et al. 2007; Kauffmann et al. 2011) and SiO (Gueth et al. 1998; Tafalla et al. 2016), though they are often bright in other molecules (Lefloch et al. 2010; Busquet et al. 2014; Podio et al. 2015).

These outflows are important to the star formation process as they are responsible for removing $\sim1/3$ of the mass (Matsushita et al. 2017) and large amounts of angular momentum (Wardle and Konigl 1993; Tomisaka 2002) from the protostellar system allowing gas to accrete onto the protostar. Further, they inevitably impact the surrounding gas and are thus an important source of turbulence in molecular clouds. Given the speeds of these outflows, the impact between the outflow gas and the surrounding molecular cloud is supersonic and leads to the formation of bright shocks that are rich in molecular species (Benedettini et al. 2013).

From a chemical stand point, these outflows are extremely interesting because the shocks they form disrupt the ice mantles of the dust grains. They are one of the few environments in which grain surface species can be studied by the gas-phase chemistry that is initiated when the ice is sublimated. However, to model this chemistry and constrain the abundances of the sublimated material, an understanding of shock waves and their effect on the physical variables that control the chemistry is required.

1.5 Shocks

Shock waves are pressure driven disturbances in a medium traveling faster that the signal speed for compressive waves, they lead to irreversible changes in the medium (Draine 2011). It is easy to demonstrate how they are relevant in astrophysical environments. If

we consider the sound speed for an ideal gas,

$$C_s = \sqrt{\frac{\partial P}{\partial \rho}} = \sqrt{k_b T/\mu} \tag{1.8}$$

where P, ρ and T are the gas pressure, density and temperature respectively, k_b is the Boltzmann constant and μ is the average mass of each gas particle. For gas comprised of molecular hydrogen, the sound speed varies from $0.2\,\mathrm{km\,s^{-1}}$ to $2\,\mathrm{km\,s^{-1}}$ over 10 K to 1000 K. As noted in Section 1.1, this covers the majority of the ISM. Therefore, a pressure change must only travel at $\sim$1 $\mathrm{km\,s^{-1}}$ in order to shock gases in the ISM and such speeds are easily reached by protostellar outflows, supernovae ejecta and stellar winds from massive stars.

From a chemical point of view, shocks in the ISM have extraordinary effects. Primarily, they discontinuously increase the density and temperature of the gas activating chemical pathways that were infeasible in the pre-shock gas. For example, the reactions

$$O + H_2 \rightarrow OH + H \tag{1.9}$$

$$OH + H_2 \rightarrow H_2O + H \tag{1.10}$$

have barriers of $\sim$0.1 eV and so only becomes efficient once gas temperatures reach $\sim$ 1000 K (Williams and Viti 2013). Such temperatures are high for the ISM but often reached within shocks.

Another effect of shocks on chemistry in the ISM is the sputtering of the ice mantles of dust grains, a process of great interest to observers and chemical modellers. Sputtering is the injection of material directly from the solid phase to the gas-phase due to bombardment of energetic particles on the solid. The ice mantles of interstellar dust, particularly in dense molecular clouds, are abundant in molecular species and, as a result, sputtering in a shock greatly increases the chemical complexity of the gas-phase.

The precise effects of shocks depend on both the properties of the medium and the shock wave. Typically, the density and temperature of the gas increase discontinuously and only conservation of mass, momentum and energy can be considered across the shock front. It is useful to define the Mach number M, the ratio of the shock speed (v_s) to the sound speed, when considering the effects of a shock. For a large enough Mach number, the strong shock limit is reached and the density change across the shock is limited to a

maximum value with the temperature continuing to increase with the Mach number,

$$\rho_1 = \frac{\gamma+1}{\gamma-1}\rho_0 \tag{1.11}$$

$$T_1 = \frac{2(\gamma-1)}{(\gamma+1)^2}\frac{\mu v_s^2}{k_b} \tag{1.12}$$

where γ is the adiabatic index and μ is the average molecular mass in atomic mass units. However, this only applies to adiabatic shocks. Should the gas be able to efficiently cool by radiation, the strong shock limit no longer applies. In such cases, the temperature T_1 is equal to T_0 and the density can be increased arbitrarily according the the relation,

$$\rho_1 = M^2\rho_0 \tag{1.13}$$

where M is the Mach number. These conditions are easily reached in molecular clouds and consequences for star formation are discussed in Chapter 3.

1.5.1 MHD Shocks

The discussion of shocks above completely neglects the effects of ionization and magnetic fields on the behaviour of the fluids. However, the majority of the ISM is partially ionized (electron fractional abundance X_e=10^{-4}-10^{-7}) and permeated by magnetic fields. The low ionization fraction means that neutral species are likely to collide with each other many times for each ion-neutral collision and so the neutral species can reach Maxwellian velocity distributions independently of the ions. The large range of the coulomb interaction means ions likewise experience many coulomb scatterings before colliding with a neutral, again equilibrating. These two fluids are only weakly coupled by the rare ion-neutral reactions and it is therefore more accurate to consider this gas as two fluids (See Draine 2011).

As a result, these two fluids move separately in a shock. The neutrals move at the shock velocity and the ions move at the magnetosonic speed given by,

$$V_{ims} = \frac{B_0}{\sqrt{4\pi\rho_i}} \tag{1.14}$$

where ρ_i is the density of the ionic fluid. If the magnetosonic speed is larger than the shock velocity then the ionic fluid moves ahead of the shock in what is known as a "magnetic precursor". Note that the low ionization fraction (ρ_i) and strong magnetic fields $\left(B_0 \sim \sqrt{\frac{n_H}{cm^{-3}}}\mu\mathrm{G}\right)$ of the ISM combine to give large magnetosonic speeds. The larger the

magnetosonic speed, the larger the dissipation region over which the the ions are ahead of the neutrals and able to heat and compress the gas ahead of the shock front. For a large enough B_0 the hydrodynamic variables become continuous due to the large region over which this occurs. Two fluids shocks that retain the discontinuity are referred to as J-type or "Jump" shocks and those that become continuous are referred to as C-type shocks (Draine 1980). Due to the nature of the ISM, these J and C-shocks are more accurate descriptions of astrophysical shocks.

1.6 Radiative Transfer

1.6.1 Rotation Diagrams and LTE

In the above sections, studying the abundances of chemical species from observations and modelling is discussed. However, whilst chemical models do give abundances, observations provide measurements of the emitted flux from an object in specific frequency intervals. In sub-millimeter astronomy, the measured quantity is the antenna temperature as a function of frequency. The antenna temperature is the temperature of a resistor that would produce the same amount of power as the antenna is receiving in a given frequency range. This can be related to the source brightness at that frequency by the antenna theorem (Kraus 1982),

$$T_a = \frac{\lambda^2}{2k}(\frac{\Delta\Omega_s}{\Delta\Omega_a})B_\nu \tag{1.15}$$

where λ is the wavelength, k is the Boltzmann constant, $\Delta\Omega_s$ is the source size, $\Delta\Omega_a$ is the antenna beam size and B_ν is the brightness. It is then useful to combine these with the equations for optical depth and brightness (Williams and Viti 2013),

$$B_\nu = \frac{h\nu/k}{e^{\frac{h\nu}{kT}} - 1}\left(\frac{1 - e^{-\tau}}{\tau}\right)\tau \tag{1.16}$$

$$\tau = \frac{h}{\Delta v}N_u B_{ij}\left(e^{\frac{h\nu}{kT}} - 1\right) \tag{1.17}$$

where h is the Planck constant, T is the gas temperature, τ is the optical depth, B_{ij} is the Einstein coefficient for stimulated emission and N_u is the column density of the upper state along the line of sight. Δv is a velocity range corresponding to the Doppler shift from some central frequency that would describe the frequency range of the emission. These

equations can be combined and rearranged to give the upper state column density as a function of the measured total emission,

$$N_u = \frac{8\pi k\nu^2}{hc^3 A_{ij}} W \left(\frac{\Delta\Omega_s}{\Delta\Omega_a}\right) \left(\frac{1-e^{-\tau}}{\tau}\right) \tag{1.18}$$

where W is the integrated emission, the antenna temperature integrated over a velocity range and A_{ij} is the Einstein coefficient for spontaneous emission. This equation ultimately relates quantities measured by the telescope and characteristics of the emission line such as its frequency and Einstein coefficients to the amount of the molecule in the excited state along the line of sight. If local thermodynamic equilibrium (LTE) is assumed, then the population levels of each excited state should be described by a Boltzmann distribution,

$$N_u = \frac{N}{Z} g_u \exp(\frac{-E_u}{kT}) \tag{1.19}$$

where N is the total column density of the molecule, Z is the partition function, g_u is the upper state degeneracy and E_u is the upper state energy. If multiple transitions are measured then their upper state column densities will follow this relationship in LTE, which is best expressed in log form as $ln(N_u)$ becomes a linear function of E_u,

$$ln(\frac{N_u}{g_u}) = -\frac{E_u}{kT} + ln(N) - ln(Z) \tag{1.20}$$

Therefore, by measuring multiple transitions of a single species, the gas temperature and species' column density can be derived in LTE assuming the source size and opacity are corrected for. It is also possible to evaluate how well these assumptions hold and to understand the affect each has when they break down. The graphical form of this analysis is called the rotation or excitation diagram and a full discussion of the method can be found in Goldsmith and Langer (1999).

A simple diagnostic of the LTE assumption, the critical density of each transition can be evaluated. This is the density at which the collisional excitation rate equals the spontaneous de-excitation rate and is a function of the radiative properties of the species and the gas temperature. If the gas density is above the critical density it can be assumed that the excitation of the transition is coupled to the gas temperature.

1.6.2 The Radiative Transfer Problem

Thermodynamic equilibrium between the gas temperature and molecular excitation levels is rarely the case at the densities observed in star forming regions. Radiative transfer models provide the bridge between the two when such an equilibrium cannot be assumed. In these models, the method is to solve the radiative transfer equation,

$$\frac{dI_\nu}{ds} = j_\nu - \alpha_\nu I_\nu \tag{1.21}$$

where I_ν is the intensity of light at frequency ν, j_ν is the emission coefficient and α_ν is the absorption coefficient over a distance s. This must be solved simultaneously with the population levels of the emitting states, a computational intensive task.

The source function, $S_\nu = j_\nu/\alpha_\nu$ is the emissivity per unit optical depth which can be combined with the definition of the absorption coefficient, $\alpha_\nu = d\tau_\nu/ds$ to give the radiative transfer equation in integral form,

$$I_\nu(\tau) = I_\nu(0)e^{-\tau_\nu} + \int_0^{\tau_\nu} S_\nu(\tau_\nu^{'})e^{-(\tau_\nu - \tau_\nu^{'})}d\tau_\nu^{'} \tag{1.22}$$

where both the source function and τ in equation 1.22 are dependent on the population levels. For a transition from an upper to a low state, the emission and absorption coefficients can be given by,

$$j_{ul} = n_u A_{ul} \tag{1.23}$$

$$\alpha_{ul} = n_l B_{lu} - n_u B_{ul} \tag{1.24}$$

where n gives the population density of the upper (u) or lower (l) states, A_{ul} is the Einstein coefficient for spontaneous decay from the upper to lower state and B is the Einstein coefficient for radiative excitement or de-excitement from the lower to upper or vice-versa. These can be combined to give the source function,

$$S_{ul} = \frac{n_u A_{ul}}{n_l B_{lu} - n_u B_{ul}} \tag{1.25}$$

which may also have an additional term for dust emission and clearly requires values for the population densities. These can be found by assuming statistical equilibrium between

the levels which as expressed as,

$$\frac{dn_i}{dt} = \sum_{j>i}[n_j A_{ji} + (n_j B_{ji} - n_i B_{ij})J_\nu] - \sum_{j<i}[n_i A_{ji} + (n_i B_{ij} - n_j B_{ji})J] + \sum_{j\neq i}[n_j C_{ji} - n_i C_{ij}] = 0 \tag{1.26}$$

where C_{ji} is the collisional Einstein coefficient for de-excitation, C_{ij} is the equivalent for excitation and J_ν is the mean intensity at a given frequency,

$$J_\nu = \frac{1}{4\pi}\int I_\nu d\Omega d\nu \tag{1.27}$$

taken over a solid angle Ω. Solving simultaneously for equations 1.27, 1.26, 1.25 and 1.22 is the radiative transfer problem and many approaches to simplifying and solving it are available in the literature. In particular, the level populations and the mean intensity are position dependent and so assumptions about the source structure must be made or the radiative transfer problem must be solved for a gridded model of the source.

1.7 This Thesis

This thesis is concerned with the observation and chemical modelling of regions associated with star formation. In Chapter 2, chemical modelling is discussed in detail with a focus on UCLCHEM, the gas-grain chemical model that was redeveloped over the course of this PhD and used for all of the work that follows. In Chapter 3, the formation of low mass stars and, more particularly, brown dwarfs is investigated. Chemical modelling is used to suggest molecules that would be indicative of star formation induced by low velocity shocks in molecular clouds. Chapter 4, moves away from low mass stars to the regions they affect. Material ejected from forming stars impacts the surrounding gas causing shocks and observations of H_2S in one such shock are analysed and modelled. Chapter 5 expands on this with additional observations of six more sulfur bearing species. Finally, Chapter 6 gives an overall summary of the work presented in this thesis and discusses possibilities for future investigation.

This page was intentionally left blank

Chapter 2

UCLCHEM

The work presented in this chapter is based on the paper by Holdship et al. (2017), in collaboration with S.Viti, I.Jimenez-Serra, A.Makrymallis and F.Priestley.

2.1 Introduction

Chemistry is ubiquitous in astrophysical environments. Molecular clouds, the cold cores in which stars form, and the warm gas surrounding protostars all exhibit chemistry of varying degrees of complexity and with different dominant chemical pathways. Understanding this chemistry is vital to the study of our own origins as well as understanding the physical structure and processes involved in star formation.

Beyond this, chemistry is a useful tool for understanding the physical conditions of the region being studied. This requires well constrained chemical networks and accurate physical models so that uncertainties in the predictions of the model are much smaller than the uncertainties in the measured abundances of molecules. With the current state of the art models, networks are generally capable of putting broad constraints on the physical conditions such as maximum gas temperatures or minimum densities and this can be of use in poorly understood regions.

Chemical modelling is typically performed by the use of rate equations. The rate of each reaction in a network of chemical reactions is calculated and used to determine the rate of change of a set of chemical species. This coupled set of ordinary differential

equations (ODEs) is integrated to give the abundance of each species at any given time. These models typically centre around gas-phase reactions provided by databases such as KIDA (Wakelam et al. 2012) and UMIST (Millar et al. 1997). Each of these databases provides a chemical code, respectively Nahoon and RATE13, which solve these networks for simple gas conditions and include other processes such as H_2 formation on the dust grains and the self-shielding of CO and H_2 from UV radiation.

This, of course, does not account for all astrochemical processes and many groups use more or less complicated chemical models for different purposes. In radiation-hydrodynamic models, it is common to reduce the network to gas-phase H, C and O based species to reduce chemical integration time whilst reproducing the abundances of major coolants such as CO given by more detailed chemical models. This improves the treatment of thermodynamics in those models without making them prohibitively computationally expensive. On the other hand, the modelling of dense prestellar cores or the formation of complex organic molecules requires much larger chemical networks and the addition of processes involving dust grains.

For example, Astrochem (Maret and Bergin 2015) includes freeze out of species onto dust grains and the non-thermal desorption of species from those grains due to UV radiation and cosmic rays making it suitable for modelling a wider range of regions than a simple gas-phase model. By further including thermal desorption, star-forming regions with high gas/dust temperature conditions can be modelled. As the temperature of the core rises, the material on the grains sublimates and proper treatment of this sublimation is required. Astrochem implements these processes, with desorption from the grain surfaces occurring according to the binding energy of each species onto the grain.

UCLCHEM is a chemical model that was first developed to study the sublimation of species from the ices in hot cores (Viti and Williams 1999) using linear temperature increases and setting the rate of the thermal desorption from the grains by the binding energy of each species. However, Collings et al. (2004) demonstrated through temperature programmed desorption experiments that multiple desorption events can occur for each species frozen on the dust grains at different temperatures dependent both on the species and on the rate of change of the temperature. This was included in UCLCHEM along with more realistic, observationally derived temperature profiles (Viti et al. 2004).

Another environment where proper grain surface as well as gas-phase chemical treatment has proven useful is in shocked gas. In these systems, sublimation from the grain

surface is dominated by sputtering, the collisional removal of surface material. The physical modelling of these shocks is an active area of research (eg. Van Loo et al. 2013; Anderl et al. 2009) and codes for this modelling are publicly available (Flower and Pineau des Forêts 2015). These models have been successful in reproducing observations of shocked regions. For example, L1157-mm is a protostar driving a bipolar outflow (Gueth et al. 1997) and the bowshocks associated with that outflow are well studied. For one of these bowshocks, L1157-B1, Gusdorf et al. (2008) reproduced the SiO emission using an MHD hydrodynamical model of a continuous or C-type shock coupled with a reduced chemical network of 100 species.

As noted, reduced chemical networks often produce similar abundances to much more complex networks when simple species such as H_2O and CO are considered and this is sufficient for many applications (eg. Schmalzl et al. 2014). Similarly, a simplified physical model may reproduce the shock features that are useful for chemistry and so a full chemical model can be run without fully solving the MHD equations. Jiménez-Serra et al. (2008) produced a parameterized C-shock that produced a shock structure in good agreement with more complicated MHD models. This was combined with the chemical code UCLCHEM to study the chemistry in shocked environments (Viti et al. 2011). Using this parameterization with a large chemical network has been met with some success in the bowshock L1157-B1 (Viti et al. 2011; Holdship et al. 2016; Lefloch et al. 2016) despite being computationally inexpensive.

The simplicity of these models means they could be used to link observed molecular lines with the underlying chemistry to get a sense of the physical properties of the shock. Conversely, emission from a source with well constrained physical properties could be used to improve uncertain parts of the chemical network. The reaction rates of species on dust grains being a prime example. For example, in Chapter 4 observations of the L1157-B1 bowshock are used to constrain sulfur chemistry on ice grains by identifying likely sulfur carriers. Ideally, chemical models could be ran over large parameter spaces to find the most likely values for uncertain parts of the network when a region has large amounts of observational data available.

To this purpose UCLCHEM has been developed over many years with numerous papers discussing major updates and applications (see Viti et al. 2004; Roberts et al. 2007). There have also been benchmarking efforts in the past (Viti et al. 2001) comparing the code to other similar models. The rewriting and development and use of the code has underpinned

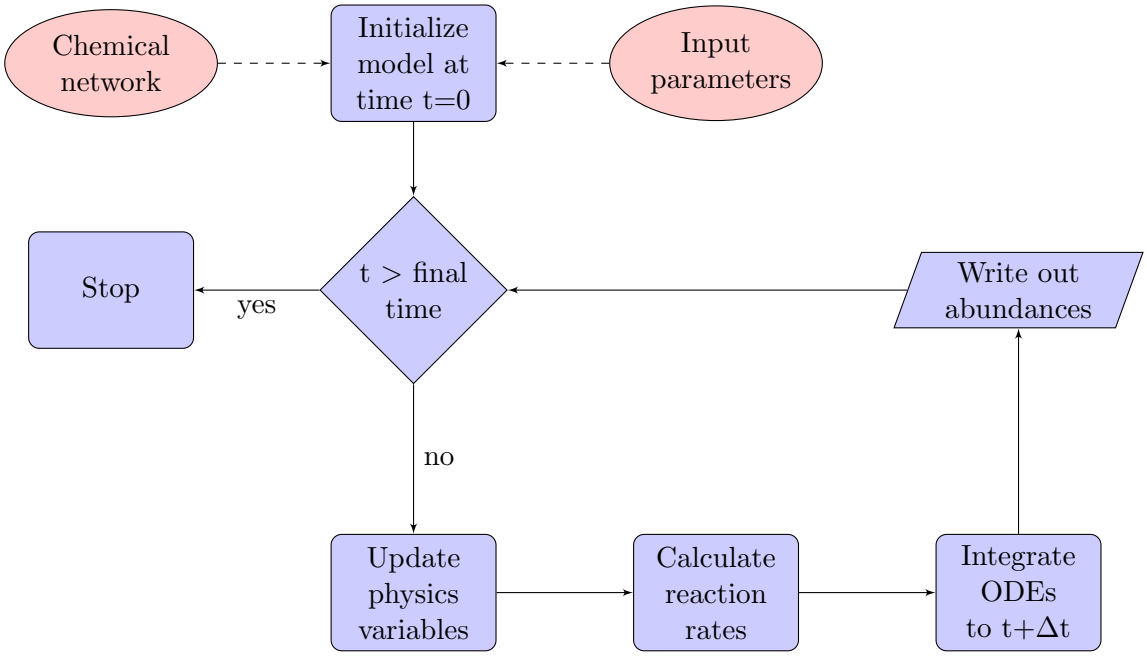

Figure 2.1: Flow chart describing the algorithm followed by UCLCHEM.

all of the work contained in this thesis. In this chapter, an overview of UCLCHEM and work done to make it available for public release is presented.

2.2 Chemical Model

At its core, UCLCHEM is a code that sets up and solves the coupled system of ODEs that gives the fractional abundances of all the species in a parcel of gas. The ODEs are created automatically from the network (see Sec. 2.3.4). There is one ODE per species and each is a sum over the rates of every reaction that involves the species. At each time step, the rates of each reaction are recalculated and the third party ODE solver DVODE (Brown et al. 1989) integrates to the end of the time step. The basic overview of the code is shown in Figure 2.1 and each component is discussed in detail in the sections below.

Each type of reaction requires a different rate calculation and so UCLCHEM is limited by the kinds of reactions that have been coded for. The subsections below detail each type of reaction and physical process currently included.

2.2.1 Gas-Phase Reactions

Gas-phase reactions make up the largest part of the chemical network. Two body reactions, cosmic ray interactions and interaction with UV photons are all included in the code. For

two body reactions, the rate of each reaction is in $\mathrm{cm^3\,s^{-1}}$ and is calculated through the Arrhenius equation,

$$R_{AB} = \alpha \left(\frac{T}{300K}\right)^{\beta} \exp\left(\frac{-\gamma}{T}\right), \tag{2.1}$$

where α, β and γ are 'rate constants' determined through experiments or theoretical studies which apply over a range of temperatures. For cosmic ray protons, cosmic ray induced photons and UV photons the rates have units of $\mathrm{s^{-1}}$ and are given by,

$$R_{CRProton} = \alpha_{cr}\zeta \tag{2.2}$$

$$R_{CRPhoton} = \alpha_{cr} \left(\frac{T}{300K}\right)^{\beta} \frac{E}{1-\omega}\zeta \tag{2.3}$$

$$R_{UV} = \alpha_{rad} F_{UV} \exp(-kA_v) \tag{2.4}$$

where ω is the dust grain albedo, ζ is the cosmic ray ionisation rate and F_{UV} is the UV flux. α_{rad} and α_{cr} are dimensionless scaling factors for the overall radiation field and cosmic ray ionisation rates for a specific reaction, β takes the same meaning as above, E is the efficiency of cosmic ray ionisation events and k is a factor increasing extinction for UV light. This formulation of the reaction rates is taken from the UMIST database notes and more information can be found in Millar et al. (1997). These rates are then used to set up and solve a series of ordinary differential equations of the form,

$$\dot{Y}_{product} = R_{AB} Y_A Y_B n_H, \tag{2.5}$$

where Y is the fractional abundance of reactants A and B and $\dot{Y}$ is the rate of change of the product. n_H is the hydrogen number density. The density and second abundance dependency is dropped for reactions between single species and photons or cosmic rays. An equivalent negative value is added to the change in the reactants. Thus, each $\dot{Y}$ has units $\mathrm{s^{-1}}$ and is integrated through time to give the unitless Y values which are ratios of the species' density to the hydrogen nuclei density.

In addition to these reactions, the rate of dissociation of CO and $\mathrm{H_2}$ due to UV is reduced by a self-shielding treatment in the code. $\mathrm{H_2}$ formation is treated with the hard-coded reaction rate,

$$R_{H2} = 10^{-17}\sqrt{T} n_H Y_H, \tag{2.6}$$

where Y_H is the fractional abundance of atomic hydrogen. This rate is taken from Draine (1978) and performed well in chemical benchmarking tests (Röllig et al. 2007). It should be noted that, despite the self-shielding treatment and inclusion of UV photon reactions from UMIST, UCLCHEM is not a PDR code and should not be used to model regions where the UV field is sufficient to be considered a PDR. This is because, in regions where UV photons dominate the chemistry, proper treatment of the heating and cooling due to photons interacting with the gas and dust is required and therefore the radiative transfer problem needs to be solved simultaneously with the chemistry. Beyond a visual extinction of three, the ionization fraction of C is significantly reduced and the photo-dissociation of H_2 becomes negligible (Röllig et al. 2007) so proper treatment of the radiation can be neglected.

2.2.2 Freeze out

All species freeze out at a rate given by,

$$R_{fr} = 4.57 \times 10^4 \alpha_f \sqrt{\frac{T}{m}} a_g fr, \tag{2.7}$$

where a_g is the grain area and fr is a constant for the rate of freeze out (Spitzer and Arny 1978; Rawlings et al. 1992). Note that the freeze out rate increases with temperature due to the increased number of collisions between molecules and the dust grains. For temperatures >30 K the freeze out rate decreases with temperature as molecules are less likely to become bound. Freeze out is turned off in UCLCHEM at this stage. α_f is a branching ratio allowing the same species to freeze through different channels into several different species. Therefore, α_f allows the user to determine what proportion of a species will freeze into different products. This is used as a proxy for the relatively uncertain surface chemistry. For example, by freezing a portion of a species as a more hydrogenated species rather than explicitly including a hydrogenation reaction in the surface network. The values for α_f in each freeze out reaction should sum to 1 for any given species. fr allows the user to set the freeze out efficiency; it is left at 1.0 in this work so that non-thermal desorption alone accounts for molecules remaining in the gas-phase. The equation is multiplied by an additional factor, C_{ion}, for positive ions to reproduce the electrostatic

attraction to the grains,

$$C_{ion} = 1 + \frac{16.47 \times 10^{-4}}{r_g T}, \tag{2.8}$$

with r_g and T being the average grain radius and temperature respectively and the constant value taken from Rawlings et al. (1992).

2.2.3 Non-thermal Desorption

From Roberts et al. (2007), three non-thermal desorption methods have been included in UCLCHEM. Molecules can leave the grain surface due to the energy released in H_2 formation, incident cosmic rays, and by UV photons from the interstellar radiation field as well as those produced when cosmic rays ionise the gas.

$$R_{DesH2} = R_{H2form}\epsilon_{H2}M_x, \tag{2.9}$$

$$R_{DesCR} = F_{cr}A\epsilon_{cr}M_x, \tag{2.10}$$

$$R_{DesUV} = F_{uv}A\epsilon_{UV}M_x \tag{2.11}$$

Where R_{H2form} is the rate of H_2 formation, F_{cr} is the flux of iron nuclei cosmic rays and F_{uv} is the flux of ISRF and cosmic ray induced UV. The ϵ values are efficiencies for each process reflecting the number of molecules released per event. A is the total grain surface area and M_x is the proportion of the mantle that is species x. The values of these parameters are given in Table 2.1 and the assumptions used to obtain them are discussed in Roberts et al. (2007).

2.2.4 Thermal Desorption

As the temperature of the dust increases, species start to desorb from the ice mantles. Laboratory experiments (eg. Ayotte et al. 2001; Burke and Brown 2010) show that a species does not desorb in a single peak but rather in multiple desorption events. These events correspond to the removal of the pure species from the mantle surface, a strong peak at the temperature corresponding to the binding energy, and the "volcanic" desorption and co-desorption of molecules that have diffused into the water ice. Collings et al. (2004) showed that many species of astrochemical relevance could be classified as CO-like, H_2O-like or intermediate, depending on what proportion of the species is removed from the

mantle in each desorption event.

To the author's knowledge, UCLCHEM is the only publicly available chemical model that implements a treatment for this. Molecules are classified according to their similarity to H_2O or CO, controlling their desorption behaviour. Further, the user can now set the proportion of each molecule that enters the gas-phase in each event, allowing the thermal desorption treatment of each molecule to improve with the laboratory data available. The user only needs to compile a list of species, along with the binding energies and desorption fractions for each grain species, the rest of this process is set up automatically (see Sect. 2.3.4). Whilst any physics module could activate the desorption process at specific temperatures, this process is strongly linked to the cloud model discussed in Sect. 2.3.2.

2.2.5 Grain Surface Reactions

Proper treatment of reactions between molecules on the grain surfaces is subject of debate. As a result, UCLCHEM has implemented grain chemistry in three ways. The method used in the basic network supplied with the code, and in the network used for the applications below, is to include hydrogenation at freeze out. For example, 10% of CO freezing onto the grains is assumed to go on to form CH_3OH in the network used here and so it is immediately added to the grain abundance of CH_3OH.

More complicated treatments are possible without editing the code. By including reactions with modified version of the rate constants in the network, grain surface reactions can be treated in the same way as gas-phase reactions. Further, UCLCHEM calculates the rates of reactions by diffusion across the grain surfaces for reactions with a third reactant labelled "DIFF". In this case, the binding energy of the two actual reactants are used to calculate their diffusion rates and included in a modified rate equation according to the treatment of Occhiogrosso et al. (2014).

2.3 Physical Model

The chemical model requires the gas density, the temperature and the visual extinction of any modelled gas parcel. Coupled with some mechanism to sublimate grain surface molecules, the control of these variables is the requirement of any physical model used to understand an object's chemistry. UCLCHEM was originally developed for clouds and hot cores (Viti et al. 2004) and has been extended to consider C-type shocks (Viti et al. 2011).

As part of the work for this chapter, these models were separated into interchangeable code modules and the required inputs were greatly simplified. This made the code easier to understand and use before it was made generally available. An additional physical model was also created and is described in Chapter 3. Below, the physical models developed for UCLCHEM and used in this thesis are described.

2.3.1 Clouds - Phase 1

The "cloud" module is the main physics module of UCLCHEM. This sets up a line of parcels from the centre to the edge of a cloud of gas and controls the density, temperature and visual extinction of each effectively giving a 1D model of a cloud. The conditions at the outer edge of the cloud are set by an interstellar radiation field and a value of visual extinction at the cloud edge. The distance from the edge of the cloud and the densities of the parcels closer to the edge are used to calculate the visual extinction and hence the radiation field for each interior parcel but parcels are otherwise treated separately.

Most physical models have initial conditions similar to a dense cloud. If the collapse of a prestellar core or the passage of a shock through a molecular cloud is to be modelled, then the gas must initially have some density (typically of order $10^4 cm^{-3}$), some initial abundance for each species, and some amount of frozen material on the dust grains. In UCLCHEM and therefore all the models in this thesis, this is achieved by running the cloud model starting with solar elemental abundances taken from Asplund et al. (2009) and an extremely low density. The validity of this is discussed in Section 2.4.2. The gas then increases in density according to a freefall equation,

$$\frac{dn}{dt} = \left(\frac{n_H^4}{n_0}\right)^{\frac{1}{3}} \left[24\pi G m_H n_0 \left(\left(\frac{n_H}{n_0}\right)^{\frac{1}{3}} - 1\right)\right]^{\frac{1}{2}} \tag{2.12}$$

where n_H is the hydrogen nuclei number density, n_0 is the initial central density and m_H is the mass of a hydrogen nucleus. The chemistry is modelled until the required density and time has been reached for the main model. This gives a cloud of gas at the required density with gas and grain abundances for each species that are consistent with the network rather than assumed. From here, all other models can progress.

2.3.2 Clouds - Phase 2

In the cloud model, Phase 2 is used to model protostellar envelopes and hot cores/corinos. As discussed above, sublimation of species from the grain is dependent both on the temperature and rate of change of temperature. In the cloud model, the temperature of the gas as a function of time and radial distance from the protostar is calculated at each time step, and compared to pre-calculated temperatures to determine when major thermal desorption events should occur. The temperature profiles and desorption peaks are from Viti et al. (2004) where the time-dependent temperature profiles and desorption temperatures for a range of high stellar masses were calculated. This has since been extended with radial dependency and lower masses (Awad et al. 2010). Alternatively, a module that reads and interpolates the output of hydrodynamical codes can be used to post-process the chemistry of hydrodynamical models.

The cloud model can also be used to study cold gas. Gas in a steady state can be modelled by setting all the required parameters and turning collapse off. Further, a number of different collapse modes have been coded into the model. The standard collapse used to create a cloud for Phase 2 is the freefall collapse taken from Rawlings et al. (1992). Parameterizations for the collapse of a Bonnor-Ebert sphere (Bonnor 1956) are also included so that the collapse of cold cores can be studied. These are described in more detail in Priestley et al. (Submitted). Each collapse model calculates the density of a parcel by following the central density of the Bonnor-Ebert sphere with time and then scaling for the radial distance of a parcel from the centre of the core. The chemistry of each parcel is evolved separately so chemical abundances as a function of radius can be studied for different collapse modes and compared to observations of collapsing cores.

2.3.3 C-shock - Phase 2

The "C-shock" model is the parameterized model of continuous or C-type shocks from Jiménez-Serra et al. (2008) adapted for use in UCLCHEM. The parameterization calculates the evolution of the velocities of the ion and neutral fluids as a function of time and deduces the physical structure of the shock from simple principles and approximations. In addition to the changes in density and temperature, the shock model includes a treatment of sputtering. The saturation time, t_{sat}, is defined in Jimenez-Serra et al. (2008). It corresponds to the time at which the abundances of species sputtered from the icy mantles

change by less than 10% in two consecutive time steps in their calculations. This gives a measurement of the time-scales at which most of the material that should be sputtered from dust grains will have been released. As the timescales in which the mantles sputter are short in the typical conditions in molecular clouds (Jiménez-Serra et al. 2008) this is treated by releasing all of the mantle material into the gas-phase at t_{sat}. The equations used to calculate the saturation time do not depend on molecular mass and so t_{sat} is the same for all species. See Jiménez-Serra et al. (2008) Appendix B for more details.

Whilst sputtering is included, there are two major grain processes that are omitted. Grain-grain collisions in the shock can cause both shattering and vaporisation. Shattering is the breaking of grains in collisions and primarily has the effect of changing the dust grain size distribution. This produces hotter and thinner shocks as the increased collisional cross section of the shattered dust more strongly couples the ionic and neutral fluids resulting a shock with more J-type characteristics (Anderl et al. 2009). Vaporisation is the desorption of mantle species due to grain heating from collisions. The inclusion of grain-grain processes vastly increases the complexity of the code and would not allow the code to be run so quickly with low computing power. Shattering in particular is likely to greatly affect the abundance of Si-bearing species as the destroyed dust grains would add to the gas-phase abundances. It should be noted however, that in models where SiO is included in the mantle, Anderl et al. (2009) find SiO abundances that are consistent with this model. The interested reader is referred to recent work on grain-grain processes in shocks for a more detailed view of this (Guillet et al. 2011; Anderl et al. 2009).

The maximum temperature reached within the shock and the saturation timescales are important inputs for the parameterization. In order to make the shock code usable without a detailed knowledge of C-type shocks, polynomial fits were made to data in the literature so that these inputs could be calculated by the code. The maximum temperature is taken from the temperature-velocity curves in Draine et al. (1983) for different gas densities and the saturation times are from Jiménez-Serra et al. (2008). As a result, the user now only needs to specify a pre-shock density and the shock speed. The original parameterization well reproduces the temperature, density and velocity of the gas through the shock produced by the MHD models of Flower and Pineau des Forêts (2003) and Kaufman and Neufeld (1996)(Jiménez-Serra et al. 2008). The modified version in UCLCHEM was tested extensively against the original parameterization to ensure it produces the same results.

The model discussed here has been successfully used to explain the behaviour of

molecules like H_2O, NH_3, CS and H_2S in shocks like L1157-B1 (Viti et al. 2011; Gómez-Ruiz et al. 2015; Holdship et al. 2016). It forms the basis of the modelling work in this chapter and Chapters 4 and 5. The parameterization has been extensively tested against MHD C-shock simulations and performs well across a wide range of input parameters. Importantly, it is computationally simple. This allows the chemistry to be the main focus without the computational costs being too prohibitive to run large grids of models to compare quickly to observations.

2.3.4 Network-MakeRates

A network of all the included species and their reactions must be supplied to the model. For UCLCHEM this consists of two parts: the gas-phase reactions taken from the UMIST database and a user-defined set of grain reactions. Grain reactions include freeze out, non-thermal desorption and any reactions between grain species. The UCLCHEM repository includes the UMIST12 data file (Millar et al. 1997) and a simple set of grain reactions. Given that the code must be explicitly given the ODEs and told which species to sublimate and in which proportions for different thermal desorption events, creating a network is complex task. To solve this, a python script called MakeRates was created to produce the input required to run UCLCHEM from a list of species, a UMIST file and a user created grain file.

2.4 Shock Chemistry

2.4.1 How Can We Trace Shocks?

In this section, a general study of C-type shocks is presented motivated by earlier observational and modelling work by Viti et al. (2011) and Gómez-Ruiz et al. (2016). A primary concern of chemical modelling is the identification of tracer molecules, the observation of which can provide information on a quantity that is not directly observed. The aim of this section is to find molecules that trace shocks, particularly those sensitive to the shock properties.

This builds on the work of Viti et al. (2011) in which H_2O and NH_3 lines were used to determine the properties of a shock. Some molecules, such as H_2O trace the full shock as they are not destroyed in the hotter parts of the post-shock gas, which then dominates the high-J emission. Others, such as NH_3 may not and are instead destroyed in the

hotter parts of the post-shock gas. This behaviour depends on both the pre-shock density and the shock speed so the determination of which molecules fall into which category in varying conditions is a rich source of information. Groupings of molecules under different shock conditions (pre-shock density and shock speed) would allow comparisons to be made between groups when observing shocked gas.

2.4.2 Model Setup

For these models, Phase 1 starts from purely atomic gas at low density (n_H=10^2 cm^{-3}), which collapses according to the freefall equation (Eq. 2.12) starting with the solar elemental abundances from Asplund et al. (2009). It should be noted that it is not clear that solar abundances are always appropriate and certainly, in higher redshift galaxies or even towards the galactic centre, the average metallicity can change (Wilson and Rood 1994). For nearby star forming regions, it should be at least approximately correct. The cloud collapses to the initial density of Phase 2 and is held there until a chosen time. The grid run for this work used a Phase 1 of 6 Myr, which provided sufficient time for the required pre-shock densities to be reached.

Table 2.1 lists the physical parameters that were set for all models ran for this work. The Phase 1 models ran here used a temperature of 10 K, a radiation field of 1 Habing and the standard cosmic ray ionization rate of 1.3×10^{-17} s^{-1}. A radius of 0.05 pc is chosen for the cloud and this sets the Av by allowing the column density between the edge of the cloud and the gas parcel to be calculated assuming a constant density. An additional 1.5 magnitudes are added to the Av, an assumed value for the amount of extinction from the interstellar radiation field to the edge of the cloud. The final density of this Phase varied depending on the density required for Phase 2 (See Table 2.2).

In Phase 2, the C-shock occurs. Table 2.2 gives a full list of the C-shock models that were run. Note, not all of the listed variables are independent, t_{sat} and T_{max} are functions of the pre-shock density ($n_{H,0}$) and shock velocity (V_s). The T_{max}, V_s relationship is extracted from figures 8 and 9 of Draine et al. (1983) which give values of maximum temperature for pre-shock densities 10^4 and 10^6 cm^{-3}. Since no values are available when the pre-shock density is 10^5 cm^{-3} the maximum temperature is calculated as the average of the 10^4 and 10^6 values. The temperature and density profiles of the gas during this C-shock are shown in Fig. 2.2, using model 27 as an example.

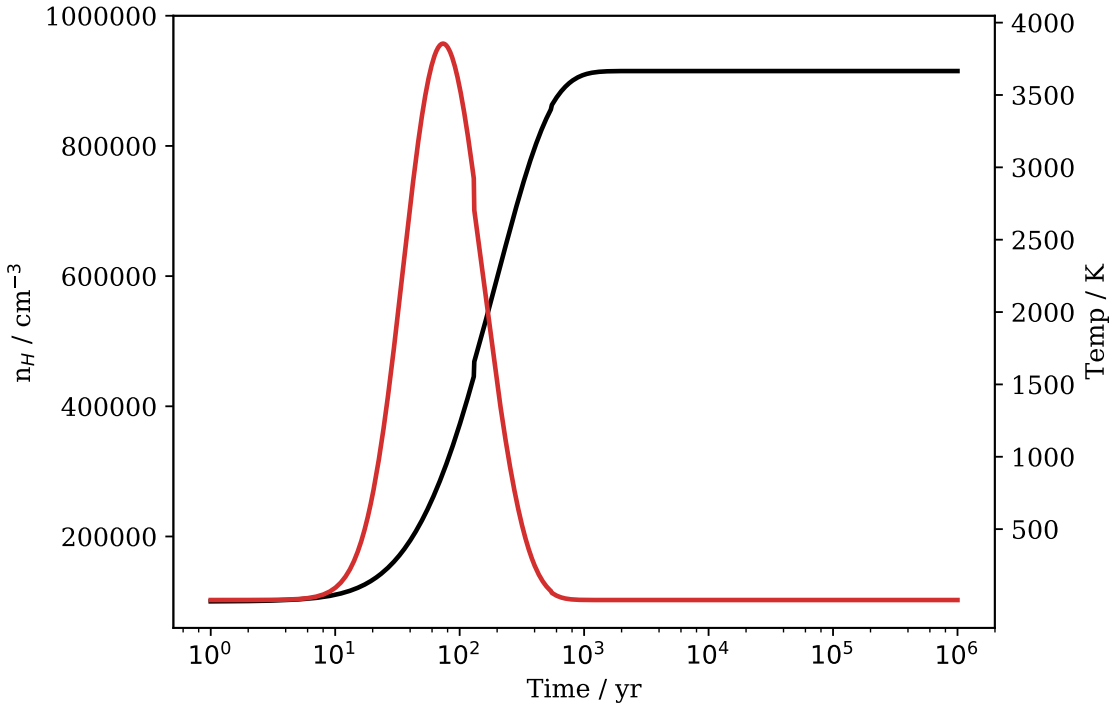

Figure 2.2: Neutral fluid temperature and density profiles of a typical model, in this case model 27 is shown. Temperature is shown in red and the density in black.

Table 2.1: List of Model Parameter Values

Variable	Value
Pre-shock Temperature	10 K
Initial Density	10^2 cm^{-3}
Freeze Out Efficiency	1.0
Radiation Field	1.0 Habing
Cosmic Ray Ionization Rate	1.3 $\times 10^{-17} s^{-1}$
Visual Extinction at Cloud Edge	1.5 mag
Cloud Radius	0.05 pc
Grain Surface Area	2.4 $\times 10^{-22}$ cm^2
H_2 Desorption (ϵ)	0.01
CR Desorption (ϕ)	10^5
UV Desorption (Y)	0.1

Table 2.2: List of Shock Variable Values

Model	$\log(n_{H,0})$	V_s / km s^{-1}	t_{sat} / yr	T_{max} / K	Z^*_{diss} / cm
1	10^3	10	975.7	323	3.70×10^{17}
2	10^4	10	97.6	323	3.70×10^{16}
3	10^5	10	9.8	301	3.70×10^{15}
4	10^6	10	1.0	279	3.70×10^{14}
5	10^3	15	746.5	584	5.55×10^{17}
6	10^4	15	74.7	584	5.55×10^{16}
7	10^5	15	7.5	555	5.55×10^{15}
8	10^6	15	0.8	525	5.55×10^{14}
9	10^3	20	586.13	869	7.41×10^{17}
10	10^4	20	58.61	869	7.41×10^{16}
11	10^5	20	5.86	893	7.41×10^{15}
12	10^6	20	0.59	916	7.41×10^{14}
13	10^3	25	483.09	1178	9.26×10^{17}
14	10^4	25	48.31	1178	9.26×10^{16}
15	10^5	25	4.83	1316	9.26×10^{15}
16	10^6	25	0.48	1454	9.26×10^{14}
17	10^3	30	425.83	1510	1.11×10^{18}
18	10^4	30	42.58	1510	1.11×10^{17}
19	10^5	30	4.26	1824	1.11×10^{16}
20	10^6	30	0.43	2137	1.11×10^{15}
21	10^3	35	402.8	1866	1.30×10^{18}
22	10^4	35	40.28	1866	1.30×10^{17}
23	10^5	35	4.03	2416	1.30×10^{16}
24	10^6	35	0.4	2966	1.30×10^{15}
25	10^3	40	402.47	2245	1.48×10^{18}
26	10^4	40	40.25	2245	1.48×10^{17}
27	10^5	40	4.02	3093	1.48×10^{16}
28	10^6	40	0.4	3941	1.48×10^{15}
29	10^3	45	413.29	2648	1.67×10^{18}
30	10^4	45	41.33	2648	1.67×10^{17}
31	10^5	45	4.13	3855	1.67×10^{16}
32	10^3	60	397.28	3999	2.22×10^{18}
33	10^4	60	39.73	3999	2.22×10^{17}
34	10^3	65	337.32	4497	2.41×10^{18}
35	10^4	65	33.73	4497	2.41×10^{17}

* Z_{diss}, the dissipation length is the length scale over which the shock dissipates, beyond which the model is no longer applicable.

2.4.3 Shock Tracers

Due to the fact freezing is efficient in cold, dense clouds, many species are highly abundant in the solid phase in the pre-shock cloud model used in this study. The result is that the fractional abundances of a similarly large number of species increase by orders of magnitude in shocks of any speed and can be used to determine whether a shock has passed. These are typically molecules that do not have efficient formation mechanisms in cold gas but are easily formed on the grain. Hydrogenated molecules in particular tend to fall into this category.

H_2O and NH_3 are highly abundant in the ices but not in the gas-phase in cold molecular clouds. Of the two, NH_3 is a more useful tracer of shocks due to the difficulties in observing H_2O from the ground. In the models, NH_3 has a fractional abundance of 10^{-14} in the pre-shock gas but can increase to 10^{-5} in a shock (see Figure 2.3). H_2S and CH_3OH similarly go from extremely low abundances in the pre-shock gas to X$\sim 10^{-5}$ in a shock. Fractional abundances as a function of shock speed for different pre-shock densities are shown in Fig. 2.3.

An important caveat to this is that the model assumes all of the grain surface material is released into the gas-phase unchanged. This may not be the case, as the collisions that cause sputtering may have enough energy to destroy molecules as they are released. Suutarinen et al. (2014) discuss this possibility in the context of CH_3OH being released from ice mantles. They find that more than 90% of CH_3OH is destroyed either in the sputtering process itself or in gas-phase reactions after sublimation. The latter is the focus of the next section of this work but it is not clear how much each process contributes to the destruction. However, the species presented here increase by over six orders of magnitude in gas-phase abundance due to sputtering, if even 1% survives the process then the enhancement is observable.

An attempt was made to identify species that vary in fractional abundance by orders of magnitude depending on the shock speed. This is in contrast to those shown in Fig 2.3 which show a steep change from no shock to a low velocity shock but no variation thereafter. Such species would allow for the possibility of determining shock properties directly from the abundance of certain molecules. Despite many species increasing in shocks, it was not possible to identify any such species. In the model, even the low velocity shocks (10 km s^{-1}) sputter the grains so all shocks can increase gas-phase abundances in this way.

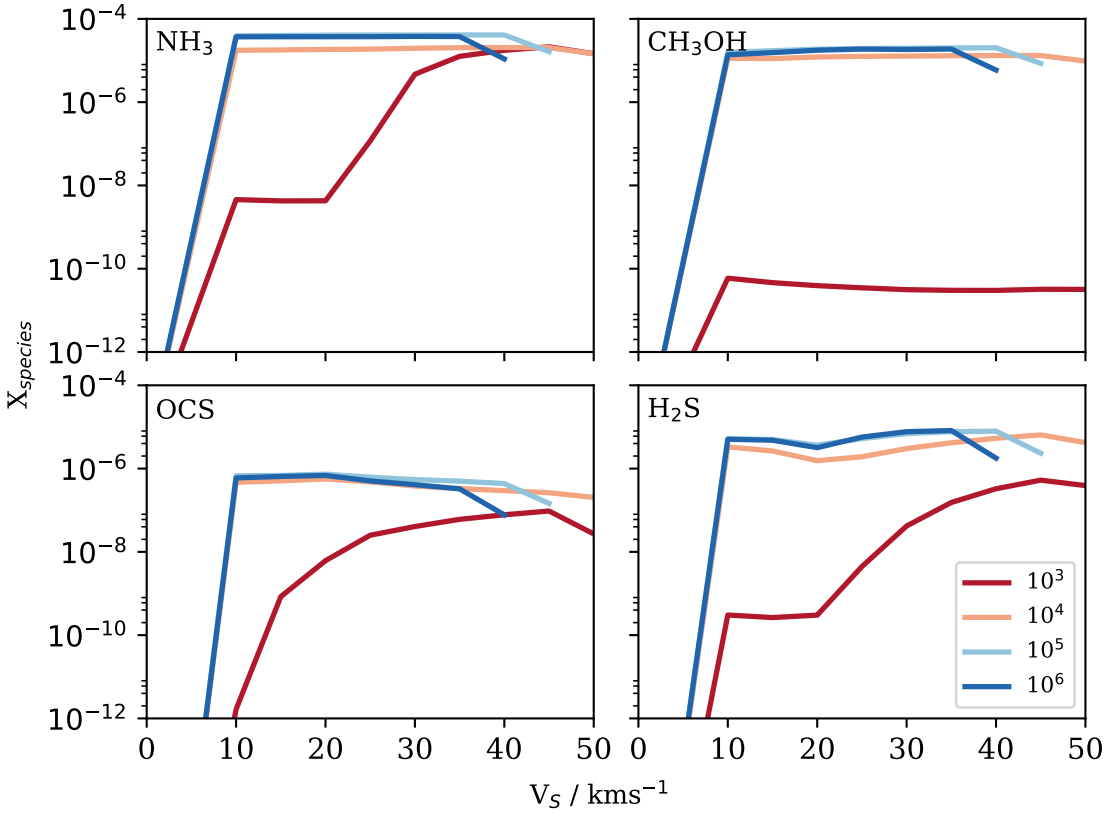

Figure 2.3: Average fractional abundance as a function of shock velocity for a number of molecules that have low gas-phase abundances in the pre-shock gas but show high abundance increases in shocks of any velocity. Each line shows a different pre-shock density, the log(n_H) values are given in the lower right plot. In the absence of other mechanisms capable of sublimating most of the species in the ices, high abundances of these molecules would indicate the passage of a shock.

Any variability due to gas temperatures reached in the shock is lost when an average over the whole shock is taken, with abundances varying by less than an order of magnitude.

It may not be possible to use the abundances directly to determine the shock velocity. However, UCLCHEM provides a useful input for the radiative transfer: a gas-phase abundance for the molecule as a function of the passage of the shock. Further, as discussed in Section 2.4.4, whilst bulk abundances are not sensitive to shock speed, line profiles can be used to provide further constraints.

2.4.4 Determining Shock Properties

The focus so far has been on average abundances across the whole shock, the observed abundance if one just resolves the shocked region. However, species can exhibit differences through the shock at different velocities even when the average is unchanged. If these

differences are ignored, the models can only be used to infer that a shock has passed. However, if the velocity profile of the emission is taken into account, much more can be learned from the models.

For example, Lefloch et al. (2010) presented NH_3 and H_2O profiles from the L1157-B1 region and showed that when scaled to be equal at their peak emission velocity, NH_3 dropped off much more quickly with increasing velocity. Viti et al. (2011) demonstrated that this is consistent with NH_3 being at lower abundance in the hotter gas, with chemical models showing that a shock with $v_s > 40$ km s^{-1} and pre-shock density of $n_H = 10^5$ cm^{-3} was sufficient to destroy NH_3 which, unlike H_2O does not efficiently reform in the gas-phase. As such, a divergence in the velocity profiles of these molecules can indicate such a shock.

Gómez-Ruiz et al. (2016) took this further and showed the difference in the terminal velocity of NH_3 and H_2O was correlated with the shock velocity inferred from the H_2O terminal velocity for a sample of protostellar outflows. Chemical modelling in the work corroborated this by showing more NH_3 being lost in faster shocks. In Chapter 4, it will be shown that H_2S exhibits the same behaviour as NH_3, dropping in abundance in high velocity gas. Given the promise of this method, molecules that exhibit this behaviour are explored so this analysis can be easily extended by observing lines of these molecules. It should be noted that the key assumption of the above studies is that the decrease in emission intensity with velocity between two molecules emitting from the same source is due to a similar change in abundance with velocity. Excitation effects will complicate this but when comparing optically thin emission scaled to match at peak velocity, it should hold as verified with radiative transfer modelling in Viti et al. (2011).

NH_3 and H_2S are unlikely to be the only molecules enhanced in shocks and subsequently destroyed in hot gas. Equally, species other than H_2O will remain enhanced throughout a shock and will thus be able to trace the whole post-shock region. H_2O can be difficult to observe with ground-based telescopes and so an alternative species showing a similar behaviour could be used as a proxy for H_2O. The modelling suggests two groups of molecules: shock-tracing (H_2O-like) and shock-destroyed (NH_3-like). Fractional abundances through a shock model for selected species from each categories are shown in Figure 2.4 to illustrate their behaviour. Observing molecules from each group and comparing their velocity profiles and abundances to the predictions of the model can constrain the shock properties.

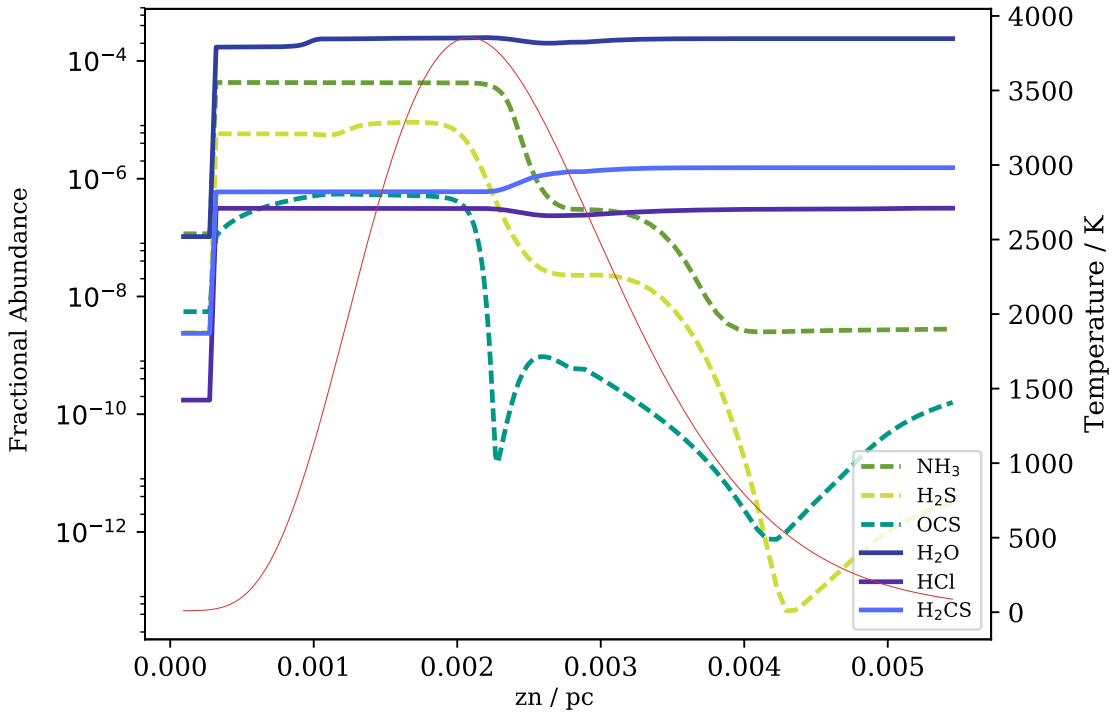

Figure 2.4: Fractional abundances as a function of distance into a shock for model 31. Species from each of the two groups are displayed as an illustration of their differences. The solid lines show H_2O-like molecules and the dashed show NH_3-like molecules. The neutral gas temperature profile is shown in red to show where the NH_3-like molecules start to fall in abundance.

A species does not necessarily fit one category or the other for all shock conditions. The behaviour is the result of temperature and density profiles of the shock and so depends on the shock speed and initial density. In Figure 2.5 all modelled pairs of shock speed and initial density are shown with lists of shock-tracing and shock-destroyed species in blue and red respectively. Species which exhibit more complicated behaviour and cannot be easily categorized are simply omitted. Some species, such as H_2O are almost always found to fall in one category, this allows them to be consistently used for a given purpose. ie. H_2O can be used to trace the full shock in most cases. However, some species will demonstrate a certain behaviour only in very specific conditions and can be used to limit possible shock properties when this is observed. For example, H_2O does not trace the full shock if the initial density is 10^3 cm^{-3} and the shock is low speed. Such species are displayed in bold in Figure 2.5.

The shock-destroyed and shock-tracing molecules are both enhanced by the sputtering caused by the shock. This is important as molecules that show low abundances in the pre-shock gas are unlikely to have large contributions from unshocked gas when a shocked

region is observed. For example, CO shows perfect shock-tracing behaviour but is also abundant in the pre-shock gas and its abundance is rather insensitive to shock interaction. As chemistry is the focus for this work, such species are omitted. However, note that high-J transitions of species such as CO are unlikely to be excited by ambient gas and so can be reliably used to trace the full extent of the shock.

2.5 Conclusions

This chapter presented and overview of chemical modelling and, in particular, the chemical model UCLCHEM. Chemical models are typically numerical solvers for large numbers of coupled ODEs and the way in which chemical networks are represented numerically was discussed. These models rely on large databases of experimental and theoretical fits to the rates of thousands of reactions and are therefore subject to large uncertainties. Nevertheless, as will be demonstrated in the following chapters, they do show success in reproducing observations of astrophysical environments.

A major purpose of chemical modelling, besides the interpretation of observations, is to provide molecular signatures of astrophysical procsses for future observations. In this chapter, UCLCHEM was used to produce molecular tracers that would help determine the properties of C-shocks. Shocks produce large and extremely fast changes in the temperature and density of gases and can also sputter material from the grain surfaces of interstellar dust. As a result, many species are both enhanced due to the sputtering and destroyed due to the high temperatures, these results are summarized in Figure 2.5. Whilst this work was exploratory, it is applied to observations of an astrophysical shock in Chapters 4 and 5.

Shock Speed / km s^{-1}

Pre-shock Gas Density / cm^{-3}

	10	15	20	25	30	35	40	45
10^3	320 **H_2O** HCl	580 **H_2O** HCl	870 **H_2O** HCl	1200 **C_3H_2** **CS**	1500 **C_3H_2** **CS**	1900 H_2O HCl **C_3H_2** H_2CN HS **CS**	2200 H_2O HCl HCN **C_3H_2** H_2CN HS	2600 H_2O HCl HCN **C_3H_2** H_2CN HS
10^4	320 H_2O HCl H_2CS CH_3OH NH_3 OCS H_2CO H_2S O_2 HCO HS NS	580 H_2O HCl H_2CS CH_3OH NH_3 OCS H_2CO H_2S O_2 HCO HS NS	870 H_2O HCl H_2CS CH_3OH NH_3 OCS NS H_2S O_2 CN HNO OH HCO HS NS	1200 H_2O HCl H_2CS CH_3OH NH_3 OCS NS H_2S O_2 CH CN HNO OH HCO HS NS	1500 H_2O HCl H_2CS CH_3OH NH_3 NS H_2S O_2 CH CN HNO OH HCO HS NS H_2CO	1900 H_2O HCl H_2CS CH_3OH NH_3 NS H_2S O_2 CH CN HNO OH HCO HS NS H_2CO	2200 H_2O HCl H_2CS CH_3OH NH_3 NS H_2S **HS** CH CN HNO HCO NS H_2CO **O_2**	2600 H_2O HCl H_2CS CH_3OH NH_3 NS H_2S **HS** CH CN HNO HCO NS H_2CO **O_2**
10^5	300 H_2O HCl H_2CS CH_3OH NH_3 OCS O_2 SO HNC HCN HCO	560 H_2O HCl H_2CS CH_3OH NH_3 OCS O_2 SO HNC HCN HCO	890 H_2O HCl H_2CS CH_3OH NH_3 OCS O_2 SO HNC HCN HCO	1300 H_2O HCl H_2CS CH_3OH NH_3 OCS O_2 SO HCN	1800 H_2O HCl H_2CS CH_3OH NH_3 OCS O_2 SO HCN HNC	2400 H_2O HCl H_2CS CH_3OH NH_3 OCS SO HCN **O_2** HNC	3100 H_2O HCl H_2CS CH_3OH NH_3 OCS SO HCN **O_2** HNC H_2CO	3900 H_2O HCl H_2CS HCN **O_2** HNC H_2CO CO_2 H_2S **NH_3** HNO HCO SO OCS **CH_3OH**
10^6	280 H_2O HCl H_2CS CH_3OH H_2S NH_3 OCS CO_2 O_2 SO HNC HCN HCO	530 H_2O HCl H_2CS CH_3OH H_2S NH_3 OCS CO_2 O_2 SO HNC HCN HCO	920 H_2O HCl H_2CS CH_3OH H_2S NH_3 OCS CO_2 O_2 SO HCN HCO OH	1500 H_2O HCl H_2CS CH_3OH H_2S NH_3 OCS CO_2 O_2 SO HCN HNC OH	2100 H_2O HCl H_2CS CH_3OH H_2S NH_3 OCS CO_2 SO HCN HNC OH	3000 H_2O HCl H_2CS CH_3OH H_2S NH_3 OCS CO_2 SO HCN **O_2** HNC OH H_2CO	3900 H_2O HCl H_2CS HCN **NH_3** **O_2** **CH_3OH** HNC H_2CO CO_2 H_2S HNO HCO SO OCS	

Figure 2.5: Shock tracers for all initial density, shock speed pairs from Table 2.2. The maximum gas temperature in Kelvin reached in each model is displayed in the relevant box. Species in blue are enhanced by the shock and trace its full extent. Species in red are enhanced initially by the shock but are destroyed as the shock increases the temperature. Species in bold are those which exhibit a given behaviour only for a small range of conditions, making them particularly useful for determining shock properties. The bottom right panel is left blank, a C-type shock cannot propagate at 45 km s^{-1} through a medium of density 10^6 cm^{-3}.

This page was intentionally left blank

Chapter 3

The Formation of Brown Dwarfs by Turbulent Fragmentation

The work presented in this chapter is based on the paper by Holdship and Viti (2016), in collaboration with S.Viti with the addition of Section 3.7.

3.1 Introduction

A brown dwarf is a substellar object with a mass less than 0.075 $M_{\odot}$; the limit below which hydrogen fusion cannot be sustained in the object's core. Since their discovery (Rebolo et al. 1995), the origin of brown dwarfs has challenged simple theories of star formation. Various theories have been put forward to explain how objects much smaller than the average Jeans mass in a molecular cloud can become gravitationally bound and unstable to collapse. This is particularly important because the brown dwarf to hydrogen-burning star ratio is observed to be as large as 1/4 (Lomax et al. 2016). There is also expected to be some overlap between the lowest mass brown dwarfs and highest mass planets. Precisely how brown dwarfs form may therefore be the main criterion for categorizing them.

For example, if brown dwarfs form by condensing out of the outer regions of a massive prestellar disk (Rice et al. 2003), then they would be hard to separate from giant planets. Other formation theories include ejection from a common envelope (Reipurth and Clarke 2001) in which several protostars fragmenting from a core accrete competitively leaving

one at much lower mass than the others. In simulations of three or more of these mutually bound objects, the lowest mass companion is regularly ejected. If this happens whilst the object is substellar, it will remain so as it will no longer have an envelope from which to accrete.

Another way brown dwarfs could form is through the photo-erosion of a prestellar core (Hester et al. 1996). If a star-forming core is overrun by a HII region, its outer layers will be ionized potentially liberating enough mass to leave an object with a total mass below the H-burning limit.

Whilst the above theories invoke a unique mechanism for forming substellar objects, there are those that treat brown dwarfs as simply the lowest mass range of the gravitationally bound objects that result from a universal star formation process. This is compelling because the IMF appears to be continuous across the H-burning limit and universal process would explain this quite readily (Whitworth et al. 2007). The theory considered in this chapter is that of turbulent fragmentation (Padoan and Nordlund 2002; Hennebelle and Chabrier 2008). In these theories, supersonic flows within molecular clouds are assumed to collide in isothermal discontinuous shocks. These shocks increase the gas density forming bound cores which may collapse to form stars. The range of core masses produced depend on the cloud's turbulent power spectrum and spans masses from the smallest brown dwarfs to the most massive stars. Both of the referenced works produce a core mass function consistent with theory and observation, implying that a universal star formation process could be responsible for all masses of stellar objects.

Differentiating between formation processes requires observations of brown dwarfs in the earliest phases of their evolution and few of these have been found. In principle, the physical characteristics of more evolved brown dwarfs could be used to identify the formation process. However, this has its difficulties. For example, a brown dwarf having a small disc could imply formation through ejection as the disc is expected to be truncated by the gravitational interaction. Unfortunately, simulations by Bate (2012) have shown that whilst most discs are truncated to $<$40 AU, discs can extend as far as 120 AU. This means that despite recent ALMA observations (Ricci et al. 2014) of three brown dwarfs which found all had disks $>$70 AU, ejection cannot be ruled out though it does seem disfavoured.

Several candidate proto-brown dwarfs have been found in the follow up of the Very Low Luminosity Objects (VeLLOs) first discovered by Spitzer (Kauffmann et al. 2005). A

recent candidate from SMA observations by Palau et al. (2014), is a good example of a brown dwarf mass object in the earliest phases of its evolution. Its mass is very likely in the brown dwarf range and it has many features that are found in low mass stars at the same phase. The similarity of these 'proto-brown dwarfs' to low mass protostars seems to imply that both sets of objects form in the same way. This view favours more universal theories of star formation such as the turbulent fragmentation scenario as they would produce both low mass stars and brown dwarfs through the same mechanism.

Whilst using physical clues to find the main route for brown dwarf formation has proven difficult, it may be possible to differentiate the formation processes chemically. The molecular abundances in a proto-brown dwarf formed from material in the disk of a massive star is likely to be different to that of a proto-brown dwarf formed in a shocked region of a molecular cloud.

This chapter focuses on an adaptation of UCLCHEM to include a simple model that simulates the formation of a brown dwarf through turbulent fragmentation. The aim of the work is to present molecular tracers that could be used to identify a pre-brown dwarf core that has formed through shock compression of gas in a molecular cloud. Chemical abundances are highly sensitive to the cloud density so the fast increase that accompanies a shock in a molecular cloud should give rise to certain molecules having abundances incompatible with a less violent density increase such as a freefall collapse.

In Section 3.2, the physical model is described. In Section 3.3, the effect of changing model parameters on the fractional abundance of molecules is explored. In Section 3.5 observational predictions for the pre-brown dwarf cores are made. Section 3.7 then demonstrates the veracity of this model by comparing to chemical post-processing of MHD simulations of a core collapsing through turbulent fragmentation. A summary of the chapter is given in Section 3.8.

3.2 The Physical Model

In order to model the formation and initial collapse of a brown dwarf mass core, the cloud model of UCLCHEM was adapted to include an instantaneous phase of density increase. The chemical model follows the abundances of 164 gas-phase species and 50 grain surface species through a network of 2432 reactions for a parcel of gas in a collapsing molecular cloud. By running several of these parcels at points along a line of sight in a molecular

cloud, a one dimensional model can be built up. The physical model comprises three phases, in which the density of the gas changes in different ways. Density is given here as the total number of hydrogen nuclei per cubic centimetre.

Phase 1 is the first phase of the cloud model described in Chapter 2. In this phase, the gas density increases in freefall from n_0=$1 \times 10^2\,cm^{-3}$ up to a final density typical of a molecular cloud, usually $10^4\,cm^{-3}$. Whilst the density is then held at this value, the model continues to run for a further 1 or 10 Myr. This allows the age of the cloud to be varied. The temperature is set to 10 K or 30 K in this phase and held constant throughout. The purpose of Phase 1 is to produce a molecular cloud for the next two phases where the gas and grain abundances are consistent with the network rather than assuming the conditions and abundances of a molecular cloud.

In Phase 2, the formation of cores by turbulent fragmentation is simulated. We consider a bound core that is formed as supersonic flows within a molecular cloud collide. In this process, the centre of the core forms first and grows outwards as gas is deposited onto it. The radius of the core would grow at a rate given by the velocity of the flow. To model this, the density and chemistry of 10 points are followed, spaced evenly between the centre and edge of the core. The innermost point (i_{point}=0) is immediately increased to the post-shock density and each point afterwards is increased to the same density at a time given by its distance from the centre and the shock speed,

$$t_{shock} = \frac{i_{point}}{N_{points} - 1} \left(\frac{r_{shock}}{M_s C_s} \right) \tag{3.1}$$

where r_{shock} is the radius of the final, post-shock core and i_{point} is a counter ranging from 0 to $(N_{points} - 1)$. The post-shock density, n_{shock}, is taken to be the critical density of a Bonnor-Ebert sphere of the mass chosen for the model,

$$n_{shock} \sim 10^3 cm^{-3} \left(\frac{M_{BD}}{3.3 M_\odot} \right)^{-2} \left(\frac{T}{10K} \right)^3 \tag{3.2}$$

where M_{BD} is the core mass, this equation was given and numerically tested by Padoan and Nordlund (2004). The final density is proportional to M_s^2 in an isothermal shock, thus the Mach speed of the shock is set by the required post-shock density in this model. A sound speed of C_s=0.2 kms^{-1} is assumed and magnetic field effects are neglected.

In the third phase of density increase, each point begins to collapse according to the same freefall equation as Phase 1 immediately after reaching n_{shock}. This means that

the innermost points in the core are already collapsing by the time the shock reaches the outer points. This collapse is to a maximum density of $10^8\,\mathrm{cm}^{-3}$, beyond which three body chemical reactions become non-negligible. The chemical network used does not include these reactions.

These shocks were considered to be isothermal so the temperature set in Phase 1 (typically 10 K) is kept constant. However, an isothermal shock does have an associated temperature increase that is short-lived enough that it does not affect the shock structure. A short period of increased temperature immediately following the shock was included to test the effect this would have. A typical post-shock temperature for a strong shock at the shock speeds used in these models is 125 K (Draine 2011). Including a temperature increase up to 500 K did not significantly alter the results and so the period of temperature increase was subsequently left out of the model.

The fractional abundances of molecular species and the density of each point are averaged for each time step giving the average density and species' fractional abundances for a line extending from the centre to the edge of a core. Whilst UCLCHEM keeps track of a total of 214 species, we focus on five molecules in particular: CO, HCO^+, CS, NH_3 and N_2H^+. These molecules are chosen as they are amongst the most commonly observed molecules in molecular clouds (see Section 3.7).

To explore the effect of varying initial conditions, eight sets of parameters were used in Phase 1 to produce different starting points for phases two and three. Table 3.1 lists the sets of conditions reached in Phase 1. Throughout this chapter, the models and figures are labelled according to the following nomenclature: N-M$_{BD}$. N refers to the model number in Table 3.1, giving the parameters used in Phase 1 for that model. M$_{BD}$ is the mass of the core chosen to be modelled. For example, 1-0.07 refers to a Phase 1 run at 10 K to produce a cloud of age 1 Myr limited to a density of $10^4\,\mathrm{cm}^{-3}$ which is subsequently used for the initial conditions to simulate the creation of a 0.07 $\mathrm{M}_\odot$ core.

3.3 Exploring Parameter Space

It is important to know how sensitive the model is to the initial conditions of the cloud. To this end, eight variations of Phase 1 were explored each with varying cloud age, density and temperature.

The age of the cloud, taken as the amount of time elapsed since the cloud reached its

Table 3.1: List of final conditions reached by Phase 1 models. Each Phase 2 model uses the final output of a Phase 1 model as its initial conditions.

Model	**Temp / K**	**Final Density / cm^{-3}**	**Time / Myr**
1	10	10^4	1
2	10	10^5	1
3	30	10^4	1
4	30	10^5	1
5	10	10^4	10
6	10	10^5	10
7	30	10^4	10
8	30	10^5	10

final Phase 1 density, was tested at 1 Myr and 10 Myr. Changing the age of the cloud leads to larger freeze out for older clouds and thus lower initial gas-phase molecular abundances at Phase 2. However, these changes were less than an order of magnitude on average and are almost completely lost in the post-shock gas.

The density of the cloud has a larger effect. Not only are the initial abundances for Phase 2 different, but the shock itself is also less violent. The density increase required to create a bound core of the chosen mass is smaller for higher density clouds and thus the shock is slower. However, the differences in molecular abundances diminish throughout Phase 2 and are lost in the freefall collapse after the shock.

Of the three cloud properties varied, temperature has the largest effect. It affects chemistry by changing the rates of reactions and, in particular, freeze out. At 30 K, collisions are more frequent between molecules and dust grains than they are at 10 K. However, it is still cold enough that molecules adsorb to the grain surface, thus the overall freeze out rate increases. The main difference then is that the abundances of each molecule shown in Figure 3.1 are two orders of magnitude lower than in other equivalent models.

Temperature also affects the shock speed. Higher temperature gas must be more dense to be gravitationally bound and so higher temperature models must have faster shocks to produce higher densities. During the shock, molecular abundances vary by more than two orders of magnitude on average. However, before and after the shock abundances differ by less than an order of magnitude and so many of the results presented in this chapter are unaffected. This is discussed further in Section 3.5.

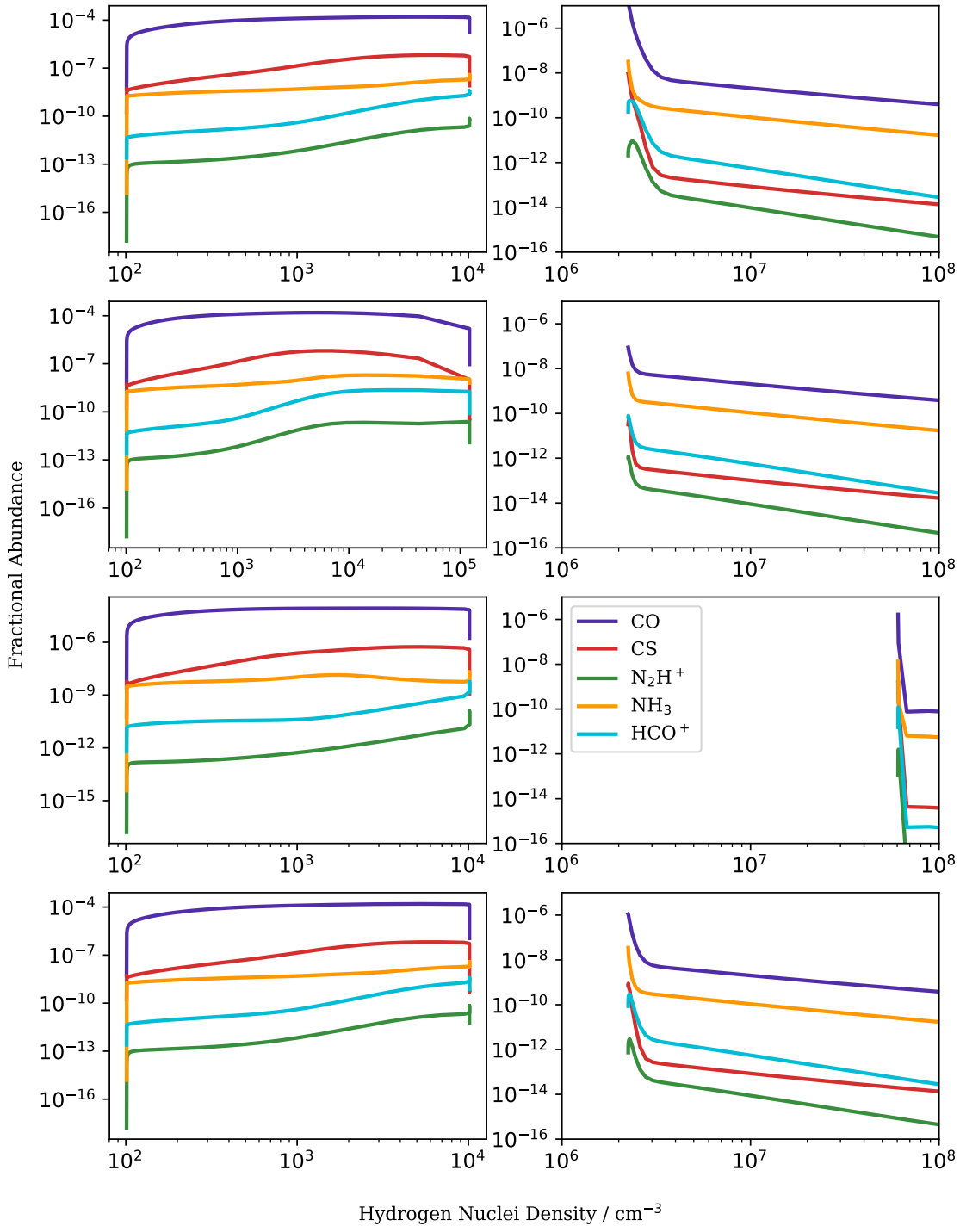

Figure 3.1: Comparison of model outputs for important molecular tracers, all showing the formation of a 0.07M$_\odot$ core but for different phase 1 parameters. The rows show models 1,2,3 and 5 from top to bottom with the left column showing Phase 1 and the right column showing Phase 2. Only model 3, the high temperature model, shows a clear difference to the other models.

3.4 Stratification

Comparisons to the core as a whole could well be enough to match observations to the models and determine whether they could be formed through turbulent fragmentation. However, modern instruments could resolve a core, allowing for characterization of its density and temperature structure. For example, the full capability of ALMA will allow angular resolutions of 0.015", allowing scales as small as 2 AU to be resolved at distances of 140 pc; the distance to the Taurus molecular cloud. It is therefore possible to ask whether the abundance of certain molecules would be expected to be higher in the centre of the core or at the edge.

The models are run as a series of gas parcels along a radial line from the centre to the edge of a core, allowing stratification to be seen by plotting fractional abundance against radial point position for given times. Figure 3.2 shows the abundances of four molecules at varying times for the 1-0.07 model. Of the five molecules examined in this chapter, four have been plotted as CS follows the behaviour of CO.

The dashed lines in Figure 3.2 show the fractional abundance of molecules just after the shock reaches the final point; when the core is considered to be just formed. At this time, there can be large differences between the core's edge and centre. NH_3 in particular is over an order of magnitude more abundant in the centre than at the edge. However, the solid lines show 0.1 Myr later and there are no differences in fractional abundances between points at this time. Given that the shock period is relatively short compared to the lifetime of the core, it is unlikely that a core will be observed mid formation and so no stratification will be observed according to this model.

3.5 Observational Tracers

The models produced here may be best used by comparing them in detail to individual pre-brown dwarf cores. However, a number of general conclusions can be drawn from the models. If the majority of pre-brown dwarf cores are formed through turbulent fragmentation then it is expected that they will be consistent with these predictions.

In order to qualify whether our predictions can lead to observables, the radiative transfer code RADEX (van der Tak et al. 2007) was used to give an indication of what might be observable in pre-brown dwarf cores considering the fractional abundances given by the models. RADEX was run repeatedly using the results of the models at different

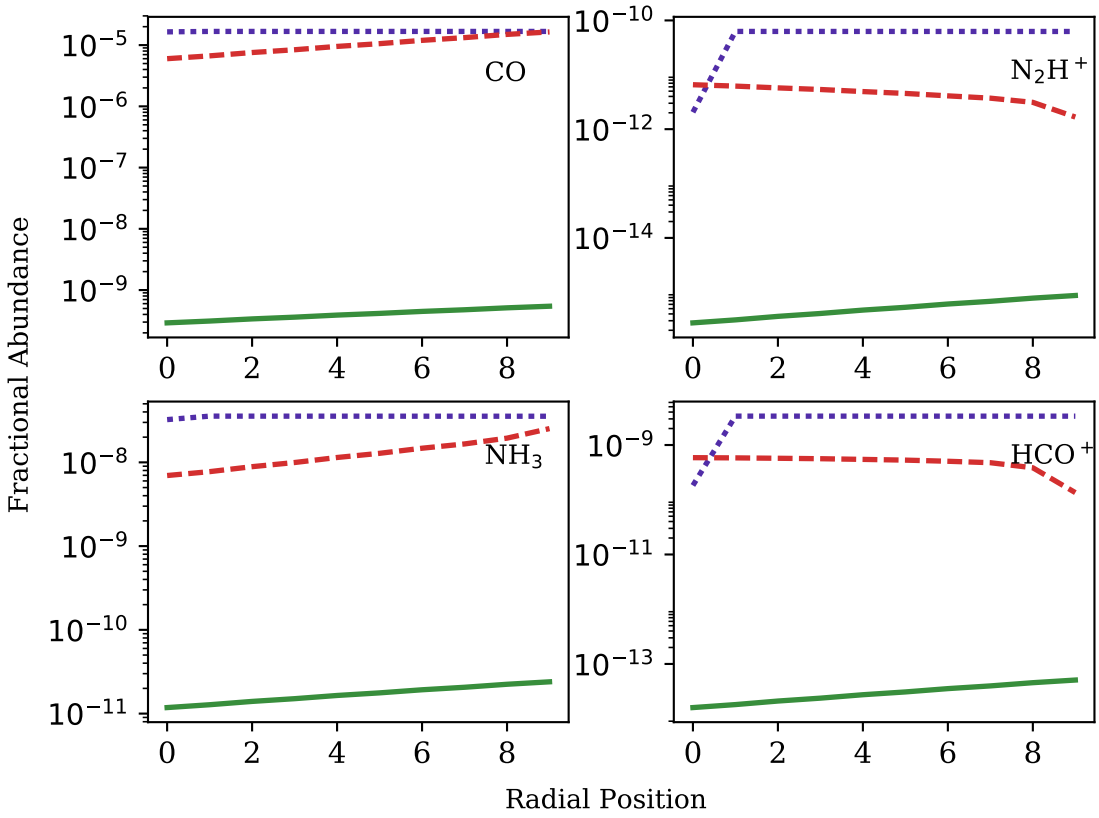

Figure 3.2: Fractional abundances with distance from core centre for four molecules, the model shown is a 0.07 M⊙ core formed from the first set of initial conditions. The x-axis shows the point number, with the centre of the core being point 0 and the edge being 9 for a total of 10 points distributed along the core radius. The dotted lines show the start of Phase 2 where only the first point has had a density increase, the dashed line shows the end of the shock passage when the final point has been reached and the solid line shows 0.1 Myr after the shock.

time steps to produce the line intensities for several molecular transitions as a function of time. For each time step, the hydrogen nuclei density was halved to give the number density of H_2 molecules, as the vast majority of H nuclei are in H_2 for all models. A kinetic temperature of 10 K is used, in line with the model temperature. The line width is assumed to be turbulence dominated and taken to be $1\,\mathrm{km\,s^{-1}}$ (Benedettini et al. 2012b). RADEX also requires a column density which was calculated by multiplying the density of each species by the radius of the core.

By considering the brightest line emitted by each molecule that would be observable using a ground based telescope and applying a lower limit for visibility, several key diagnostics of a core formed through turbulent fragmentation were found. The capabilities of ALMA and the VLA were used as a guide. Of course, the results given assume that

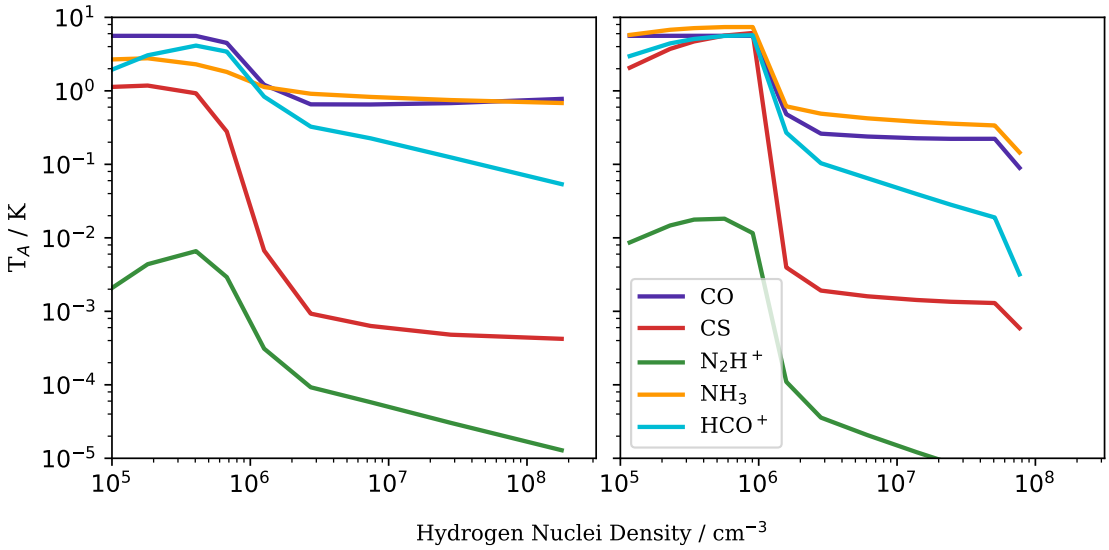

Figure 3.3: Brightness temperature expected for the five transitions discussed in Section 3.5 plotted against the average density of the core. On the left, a freefall model is shown and on the right a turbulent fragmentation model in which a 0.07 M⊙ core is formed from a cloud using the first set of initial conditions. HCO^+ in particularly is an order of magntiude brighter in the freefall model than in the turbulent fragmentation model.

most of the flux is recovered which may not be the case. No adjustment for beamsize has been made as both arrays have synthesized beamwidths smaller than the typical angular size of these cores; ∼10" at 140 pc. T_A = 100 mK has been used as the lower limit for a detectable line (see Section 3.7). The results discussed in this section are based on models using the first set of initial conditions: n_H=1 × 10^4 cm^{-3}, T=10K and an age of 6 Myr.

For bound cores above 0.04 M⊙, detection of the CO 2-1 and NH_3 $1_{(1,0)}$-$1_{(1,0)}$ transitions are expected. They are difficult to differentiate from a core formed through freefall using the 100 mK cut off. However, the behaviour of the HCO^+ 3-2 transition is very different between turbulent fragmentation model and freefall. HCO^+ is an order of magnitude brighter in freefall cores than in the turbulent fragmentation models and remains observable to high densities. A comparison between a 0.07 M⊙ and equivalent freefall model is shown in Figure 3.3.

This is not the case for an extremely low mass core (<0.04 M⊙). Such cores are extremely dense and are formed very quickly, giving bright lines in CS 3-2 and N_2H^+ $1_{(2,3)}$ - $0_{(1,2)}$ which are not apparent in higher mass cores or cores formed through freefall. Cores are unlikely to be detected during the shock as this is a very short lived stage. However, an unusually bright CS 3-2 line would be an indicator of a shock in progress.

Table 3.2 shows which of the molecules considered in this chapter are observable in cores

Table 3.2: Observable molecules for different models at $n_H > 10^7 cm^{-3}$, where an observable molecule is considered to be one that has a transition which would emit with a brightness temperature greater than 100 mK. All models use the first set of initial conditions. A + indicates an observable molecule.

Molecule	0.01 $M_\odot$	0.04 $M_\odot$	0.07 $M_\odot$	0.10 $M_\odot$	Freefall
CO	+	+	+	+	+
HCO^+	+				+
CS	+				
NH_3	+	+	+	+	+
N_2H^+	+				

at densities of $n_H > 10^7 cm^{-3}$. The models shown use Model 1 conditions. 30 K models have much higher n_{shock} values and so molecules remain detectable at higher densities. All five molecules are detectable up to at least $n_H = 10^8 cm^{-3}$ for the 0.04 and 0.01 $M_\odot$ models at 30 K.

3.6 Comparison To Observations

Only one pre-brown dwarf core has been firmly detected so far. André et al. (2012) presented observations of a core of mass less than 0.03 $M_\odot$ with a good detection in the 3.2 mm continuum and the N_2H^+ $1_{0,1}$-$0_{1,2}$ line. The core is estimated to be at $n_H > 7.5 \times 10^7$ cm^{-3}. The density, the signal to noise ratio of the observed line and the apparent early evolutionary stage of the object make it an ideal candidate for comparison to the models in this chapter.

Figure 3.4 shows the RADEX derived intensities for the detected transition using the model abundances as a function of density. Whilst a N_2H^+ detection at this density would not fit with freefall or higher mass models it would fit with low mass models where the density has been greatly increased by the shock. This is by no means conclusive but it does show that there are measured abundances in very low mass cores that do not fit with simple freefall models and can be fitted by assuming a fast density increase due to a shock.

The turbulent fragmentation process is not brown dwarf specific, therefore prestellar cores in the low mass star range could be used to test the model until more pre-brown dwarf cores are discovered. Seo et al. (2015) used a source finding algorithm with NH_3 observations of the L1495-B218 filaments in the Taurus molecular cloud and found many low mass cores which are potentially prestellar cores. In their work Seo et al. present core masses estimated from dust emission and from NH_3 column densities using an assumed

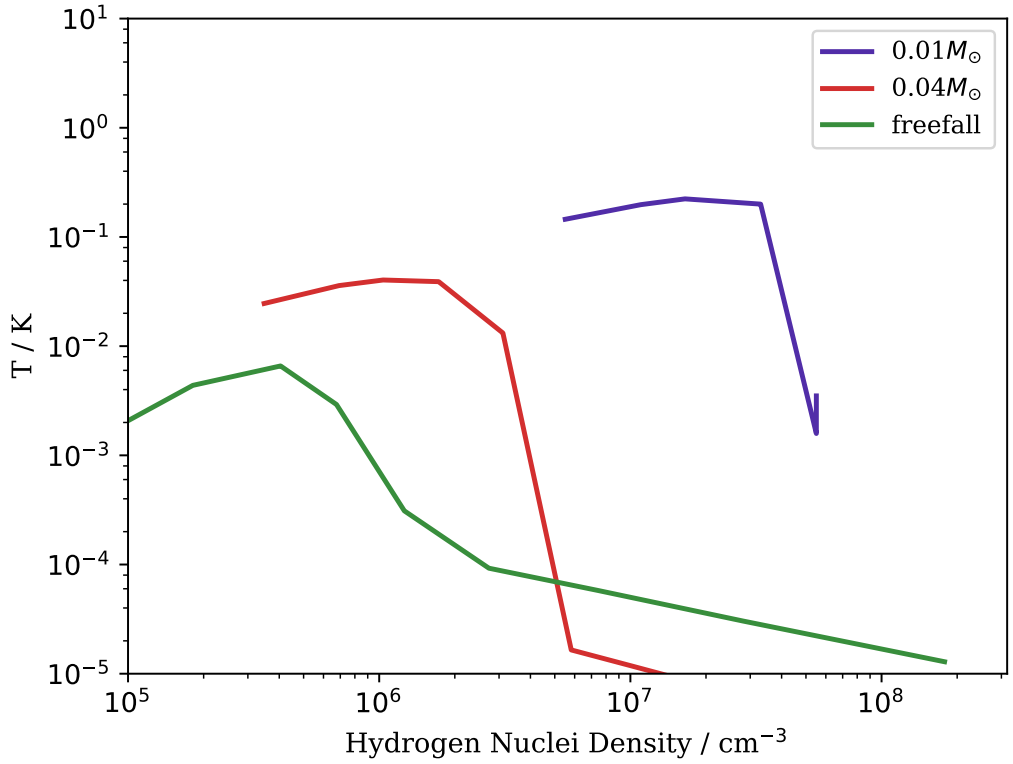

Figure 3.4: Brightness temperature of the N_2H^+ $1_{0,1}$-$0_{1,2}$ transition for three models; 0.01 $M_\odot$ (blue),0.04 $M_\odot$ (red) and freefall (green). Only the lowest mass turbulent fragmentation model can produce a bright line for this transition at n_H=7.5x10^{7}cm^{-3}; the density calculated by André et al. (2012).

fractional abundance of NH_3. Using these to calculate their measured mass of NH_3 and assuming the mass from dust is the total core mass, we have arrived at NH_3 fractional abundances for their cores. Table 3.3 shows a comparison between those NH_3 abundance estimates and the models. The models show poor fits for the brown dwarf mass cores. However, it is worth noting that none of these cores are gravitationally bound according the Virial masses calculated by Seo et al. (2015). The models in this chapter use the mass to set n_{shock} assuming that a bound core will be produced, therefore an unbound core is not expected to be a good match to the models. For this reason models were run with higher mass cores to compare to the higher mass, bound objects in the paper. For the higher mass cores in Table 3.3, the fractional abundance of NH_3 is much closer and is a good match considering that without density measurements, the abundances can change by a factor of a few depending on which density value is chosen. The model abundances chosen are during the post-shock period where many molecules maintain constant fractional abundances for

Table 3.3: List of cores from Seo et al. (2015) with model equivalents. Fractional abundances are given in units of 10^{-9}. Abundances from the model are taken to be the average abundance for the post-shock core.

Mass/ $M_\odot$	Virial Mass/ $M_\odot$	$X(NH_3)_{observed}$	$X(NH_3)_{model}$
0.04	0.31	1.13	0.07
0.07	0.22	1.07	0.32
0.10	0.58	1.8	0.5
0.88	0.77	3.65	1.5
0.95	0.98	1.35	2.5
0.99	1.09	1.00	1.0

close to a million years. This is the most likely stage in which to view the cores as it is by far the longest.

For further comparison, the models were fitted to data on dense cores in the Lupus molecular cloud, presented by Benedettini et al. (2012b), which could be prestellar cores. Whilst the density and mass of these cores is unknown, they do calculate the column densities of up to 5 species for each core. The three cores (Lupus1 C4,C6 and C7) with the most column density data were chosen and the column densities were used to compare the ratios of CH_3OH, HC_3N, N_2H^+ and NH_3 with CS to the same ratios from our models. For each model, the best fit density was found through a χ^2 test in which the squared difference between the four observed column density ratios and model abundance ratios were compared to the squared observational error on the column density ratios. These χ^2 values were used to evaluate which model and density would best fit the cores giving effectively four free parameters: core density, temperature, age and initial cloud density. This test was done for all the initial conditions and brown dwarf masses; none were considered to be a good fit. This seems to imply that, whether they are gravitationally bound or not, the objects presented by Benedettini et al. (2012b) are not high density cores formed through turbulent fragmentation.

3.7 Comparison to MHD models

The work presented in this chapter represents a first step towards modelling cores formed through turbulent fragmentation. To investigate its short-comings and how the model can be moved forward, a more detailed dynamical model was required. The ideal way to do this is to perform MHD modelling of the formation and collapse of a core in turbulent gas whilst simultaneously solving for the chemistry and radiative transfer in the core. However,

this would represent an infeasible amount of work and a great deal of computational complexity. For these purposes, post-processing the results of MHD modelling to calculate the chemistry should be sufficient to discuss the differences between the simple model presented above and a more accurate model of the physics.

The MHD model used is based on the work of Offner and Arce (2014), in which the collapse of a isothermal sphere through to the early stages of the protostar was studied. The model includes turbulence, self-gravity, radiative transfer for cooling, and an initially uniform magnetic field along one axis. The authors of that work produced a $0.2M_{\odot}$ model for this comparison and provided 1D cuts of the gas density along the x- and z-axis, the z-axis being the direction of the initial magnetic field. These outputs were re-binned into 65 radial points, the minimum amount of points that could capture the density structure of the model at each timestep.

UCLCHEM was adapted to read the resulting time series and use it as the physical inputs for the chemistry. An equivalent model was run using the turbulent fragmentation model described above for a $0.2M_{\odot}$ core. Both models used the first set of initial conditions from Table 3.1 and the same chemical network as used for the original turbulent fragmentation work.

Two major conclusions could be found from the comparison. Firstly, averaging over the whole core, the chemical abundances are remarkably similar between the two models. Figure 3.5 shows the fractional abundances of various species as a function of the average density of the core for each model. The fractional abundances are density weighted averages and they clearly follow extremely similar trends.

However, if the fractional abundance of each species is plotted as a function of radius at comparable times in each model, it is clear that the lack of stratification found in the simple model presented in this chapter is the result of an oversimplification of the physics. Primarily, turbulent motions in molecular clouds may lead to the formation of cores, but that turbulence does not dissipate immediately. The gas density is a decreasing function of radius in the MHD outputs and is also subject to fluctuations where low density outer regions suddenly and briefly increase in density before returning to lower values and this leads to much more complicated chemical trends. Most strikingly, the radial density profile is such that freeze out is less efficient and UV driven processes are faster in the MHD model. As a result of the reduced freeze out and increased photo-desorption from the ices, the abundances of many molecules are increased towards the edge of the core.

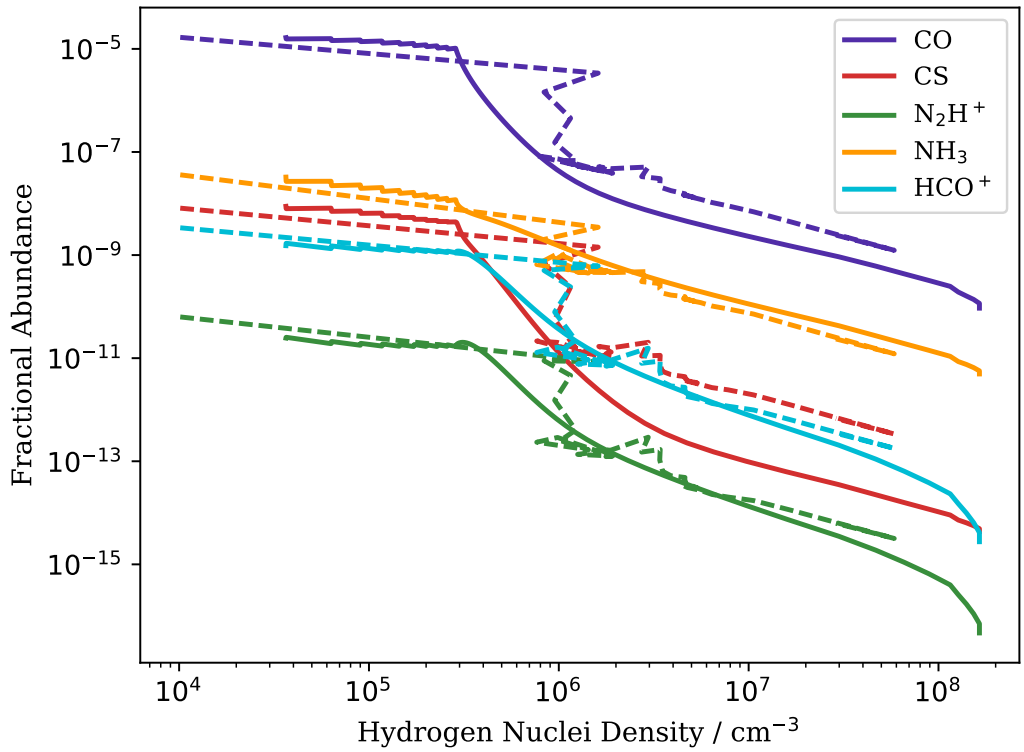

Figure 3.5: Fractional abundance as a function of average core density for the turbulent fragmentation model (solid lines) and MHD post-processing (dashed). The MHD core fluctuates in density complicating the abundance profiles but clearly follow the same trend as the turbulent fragmentation model presented in this chapter.

Figure 3.6 shows radial profiles of the fractional abundances from each model $\sim 1 \times 10^5$ yr after the initial formation of the core. The turbulent fragmentation model from this chapter shows species only slightly increasing with radius whereas there is a clear trend of the fractional abundance of each species increasing with radius in the MHD post-processing models.

3.8 Conclusions

UCLCHEM was adapted to investigate the formation of brown dwarfs through turbulent fragmentation. To do this a simple 1D model of a shock travelling through a cloud was applied to the chemical model. The resulting chemistry is expected to be representative of what would be observed in prestellar cores formed by the collision of turbulent flows. Without more observations to compare to, it is difficult to say how reliable the models are. However, certain aspects are promising as they essentially reproduce the results of

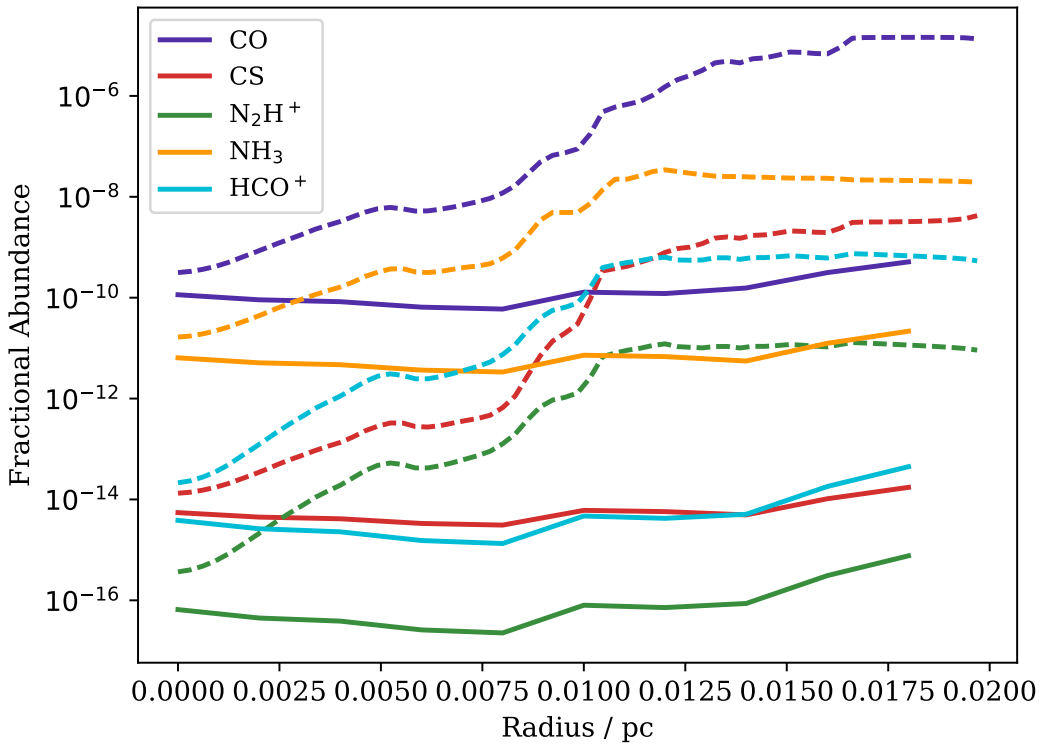

Figure 3.6: Fractional abundance as a function of radius for the turbulent fragmentation model (solid lines) and MHD post-processing (dashed). From these plots, it is clear that the non-uniform, Bonnor-Ebert like density profile from the MHD model has a strong effect on the chemistry and the flat density profile of the turbulent fragmentation model is unable to reproduce it.

freefall models for low mass stars and show behaviour that is incompatible with freefall in brown dwarf cores where the effects of turbulent compression would be strongest. For example, in an extremely low mass brown dwarf, the N_2H^+ abundance is three orders of magnitude higher than in an equivalent freefall model.

The model is not strongly sensitive to the initial conditions investigated, though changes in the gas temperature do affect the results. In principle, temperature measurements may be included when fitting with the models. However, despite this sensitivity, the models produce molecular abundances which are incompatible with freefall models for a wide range of initial conditions. This has allowed the proposal of general observational tests that could mark a core as worth following up with more observations. These include the detection of CO and NH_3 in a low mass core without the detection of HCO^+ which would be expected from freefall. Whilst the existence of pre-brown dwarf cores does in itself reduce the possible formation routes, the possibility of matching the chemistry to a

specific formation model would add to the body of evidence available for determining how very low mass objects form.

Introducing the shock to the model produces many changes to the chemistry when compared to freefall models. The largest effects of the shock are in maintaining high abundances of molecules at high core densities where they would normally have frozen out during a freefall collapse. An example is CS which is undetectable at X_{CS} $<10^{-12}$ in a core of density $n_H=10^7 cm^{-3}$ for freefall models but has a fractional abundance of $X_{CS}=10^{-8}$ for the lowest mass brown dwarf model. Similarly, CS freezes out more quickly than CO during a freefall, leading to a larger ratio at higher densities during a freefall collapse. However, this ratio does not increase during the shock as both species remain at roughly constant fractional abundance. This flattening in the CS trends also means that it is never less abundant than N_2H^+ in the shock models whilst it freezes out more quickly than N_2H^+ in freefall and is generally less abundant.

The model was finally compared to the results of post-processing the chemistry for MHD simulations of cores collapsing under turbulent fragmentation. Taking source averaged fractional abundances, the model and MHD post-processing are in agreement with each other. However, radial density profile in the model is far too simplified to match the results of the MHD simulations. It is possible that if the post-core formation collapse was replaced with a more accurate collapse model (see Priestley et al., submitted) then it would be sufficient but further work is required to ascertain this.

This page was intentionally left blank

Chapter 4

H_2S in the L1157-B1 Bow Shock

The work presented in this chapter is based on the paper by Holdship et al. (2016), in collaboration with S.Viti, I.Jimenez-Serra, B. Lefloch, C. Codella, L. Podio, M. Benedettini, F. Fontani, R.Bachiller, C. Ceccarelli and M. Tafalla.

4.1 Introduction

In Section 1.4.3 of the Introduction, outflows and jets driven by low mass protostars in the earliest stages of their evolution were discussed. The observation and modelling of ones of these objects is the subject of this chapter. The collision between a jet and the associated protostar's parent cloud is supersonic, producing shock fronts of warm, dense gas. This in turn drives processes that greatly increase the chemical complexity, such as endothermic reactions, sputtering from dust grains and ice mantle sublimation. Many molecular species are enhanced in abundance through this process (Draine et al. 1983; van Dishoeck and Blake 1998; Codella et al. 2013) and the observation and modelling of these species is a powerful tool for understanding their gas-phase chemistry and the initial pre-shock composition of the ices on the grains.

L1157-mm is a low mass Class 0 protostar driving a molecular outflow (Gueth et al. 1997) and is at a distance of 250 pc (Looney et al. 2007). The outflow was discovered by Umemoto et al. (1992) who also inferred the presence of strong shocks from the temperature of the gas implied by NH_3 and SiO emission. Since then, several bow shocks

along the outflow have been identified and studied due to their rich chemical content. The brightest of these, L1157-B1, has a complex, clumpy structure (Tafalla and Bachiller 1995; Benedettini et al. 2007) and an age of order 1000 yr constrained by observations (Podio et al. 2016) and models (Flower and Pineau des Forêts 2012). Emission from molecules thought to be formed on icy mantles such as methanol and water have been observed (Bachiller and Pérez Gutiérrez 1997; Busquet et al. 2014). This high degree of study of the L1157 outflow has led to it being considered the prototype of a chemically rich molecular outflow (Bachiller et al. 2001). Therefore, L1157 represents the best laboratory to study the initial composition of the ices.

Through the IRAM large program ASAI (Astrochemical Surveys At IRAM) and the Herschel Key project CHESS (Chemical HErschel Surveys of Star forming regions), a spectral survey of L1157-B1 has been performed in the frequency ranges of 80-350 GHz (IRAM-30m/EMIR) and 500-2000 GHz (Herschel-HIFI). The first results of the CHESS survey (Lefloch et al. 2010, 2012) confirmed the chemical richness of the bow shock. Several studies have started to compare the observed species with chemical models to derive the properties of the shock in L1157-B1 (Viti et al. 2011; Benedettini et al. 2012a, 2013). Podio et al. (2014) reported the emission of molecular ions, including SO^+ and HCS^+, whose chemistry is closely related to the amount of S-bearing molecules released from dust grains, such as H_2S and OCS.

Sulfur is highly reactive and therefore its chemistry is very sensitive to the thermal and kinetic properties of the gas. That chemistry, if it were well understood, could be used to constrain the properties of the bow shock or regions within it. In fact, H_2S has been studied along with SO and SO_2 as a chemical clock for environments where dust grains are disrupted since it was first proposed by Charnley (1997). A key assumption for this is that H_2S is one of the most abundant sulfur bearing species on ice mantles (Wakelam et al. 2004) and is then released into the gas-phase during a shock.

This assumption requires further study to determine its veracity. OCS and SO_2 are the only sulfur-bearing species firmly detected in the solid phase so far (Geballe et al. 1985; Palumbo et al. 1995; Boogert et al. 1997). Whilst a direct detection is preferred, it is possible to constrain the H_2S abundance on grains through observations of the gas-phase where ice mantles are disrupted. In observations of hot cores, Hatchell et al. (1998) were able to model the observed abundances of sulfur-bearing species only if H_2S had an abundance of 10^{-8} to 10^{-7}, much lower than the cosmic sulfur abundance. Evidence for

large amount of OCS on the other hand was presented by Podio et al. (2014). In order to reproduce the abundance of CS and HCS^+ observed in L1157-B1, their model required OCS be one of the main sulfur carriers on dust grains. Despite this, detections of solid OCS give abundances that would account for only ∼0.5% of the cosmic sulfur abundance (Palumbo et al. 1997). Since estimates of grain-surface OCS abundances may be affected by blending with a nearby methanol feature in infra-red spectra, it is possible that much sulfur is eventually locked in solid OCS.

Other forms of sulfur have been considered. Woods et al. (2015) investigated the gas and solid-phase network of sulfur-bearing species using new experimental and theoretical studies (Garozzo et al. 2010; Ward et al. 2012; Loison et al. 2012). They found that although species such as H_2S and H_2S_2 are present on the ices, they are not sufficiently abundant to be the major carriers of sulfur. In fact, a residue of atomic sulfur may be abundant enough to harbour a large amount of the total sulfur budget. This residue may come off during sputtering if a fast enough shock is present. A shock velocity of $25\,\mathrm{km\,s^{-1}}$ is likely to be sufficient to release even highly refractory species from the grains (May et al. 2000). One would expect to commonly observe chemistry involving atomic sulfur in shocked regions as this sulfur residue is sputtered from the mantle at such shock velocities. They also found that H_2S is in fact the predominant sulfur-bearing species at the early phases of the pre-stellar core.

In summary, H_2S is routinely observed in warm, sometimes shocked environments, in the gas-phase; yet it is undetected in the ices to date. Given the uncertainty of the origin of H_2S on grains and the fact that L1157-B1 contains gas that is highly processed by shocks, the physical properties and kinematics of the H_2S gas could help determine its chemical origin.

In this chapter, H_2S observations along the L1157-B1 clump are presented and its origin and relationship to other sulfur-bearing species are investigated by the use of the shock model of UCLCHEM. In Section 4.2, the observations with HIFI and the IRAM 30m telescope are described. In Section 4.3, the detected H_2S lines are presented and analyzed. In Section 4.4, the abundance and behaviour of H_2S is compared to CS and NH_3 as well as to a chemical model in which the form of sulfur in ice mantles is explored. Finally, a summary is presented in Section 4.5.

4.2 Observations

4.2.1 IRAM-30m

The H_2S and $H_2^{34}S$ ($1_{1,0}$-$1_{0,1}$) lines as well as the HDS ($1_{1,0}$-$0_{0,0}$) were detected during the ASAI program's unbiased spectral survey of L1157-B1 with the IRAM 30m telescope. The pointed co-ordinates were $\alpha_{J2000} = 20^h39^m10.2^s$, $\delta_{J2000} = +68^\circ01'10".5$ i.e. $\Delta\alpha = +25".6$, $\Delta\delta = -63".5$ from the driving protostar. NGC7538 was used for pointing, which was monitored regularly. It was found very stable with corrections less than 3". The observed region and the relevant beam-sizes for the observations presented here are shown in Fig. 4.1. The broadband EMIR receivers were used with the Fourier Transform Spectrometer backend which provides a spectral resolution of 200 kHz, equivalent to $0.35\,\mathrm{km\,s^{-1}}$ for the transitions at around 168 GHz. The transition at 244 GHz was smoothed to a velocity resolution of $1.00\,\mathrm{km\,s^{-1}}$ to improve the signal to noise ratio. Forward and beam efficiencies are provided for certain frequencies (Greve et al. 1998) and a linear fit gives a good estimate when interpolating between points. Table 4.2 gives these efficiencies as well as the telescope half power beam-width at the observed frequencies. Line intensities were converted to units of T_{MB} by using the B_{eff} and F_{eff} values given in Table 4.2.

4.2.2 Herschel-HIFI

The H_2S ($2_{0,2}$-$1_{1,1}$), ($2_{1,2}$-$1_{0,1}$) and HDS ($2_{1,2}$-$1_{0,1}$) transitions were detected with Herschel (Pilbratt et al. 2010) using the HIFI instrument (de Graauw et al. 2010), in bands 2A, 2B and 1B respectively as part of the CHESS spectral survey. The observations were done in double beam switching mode, with the pointed co-ordinates being the same as the IRAM-30m observations. The receiver was tuned in double sideband and the Wide Band Spectrometer was used. At the frequencies observed, the pointing of the H and V polarisations can differ by as much as 5". However, the spectra are in good agreement having similar rms values, line profiles and fluxes for detected lines and are therefore averaged. The data were processed using ESA supported package HIPE 6 (Herschel Interactive Processing environment, Ott et al. 2010) and FITS files from level 2 were exported for further reduction in GILDAS[1]. The resulting spectra have a velocity resolution of $0.25\,\mathrm{km\,s^{-1}}$ and an rms of 3.6 mK. Values for beam efficiency were taken from Roelfsema et al. (2012) and

[1] http://www.iram.fr/IRAMFR/GILDAS/

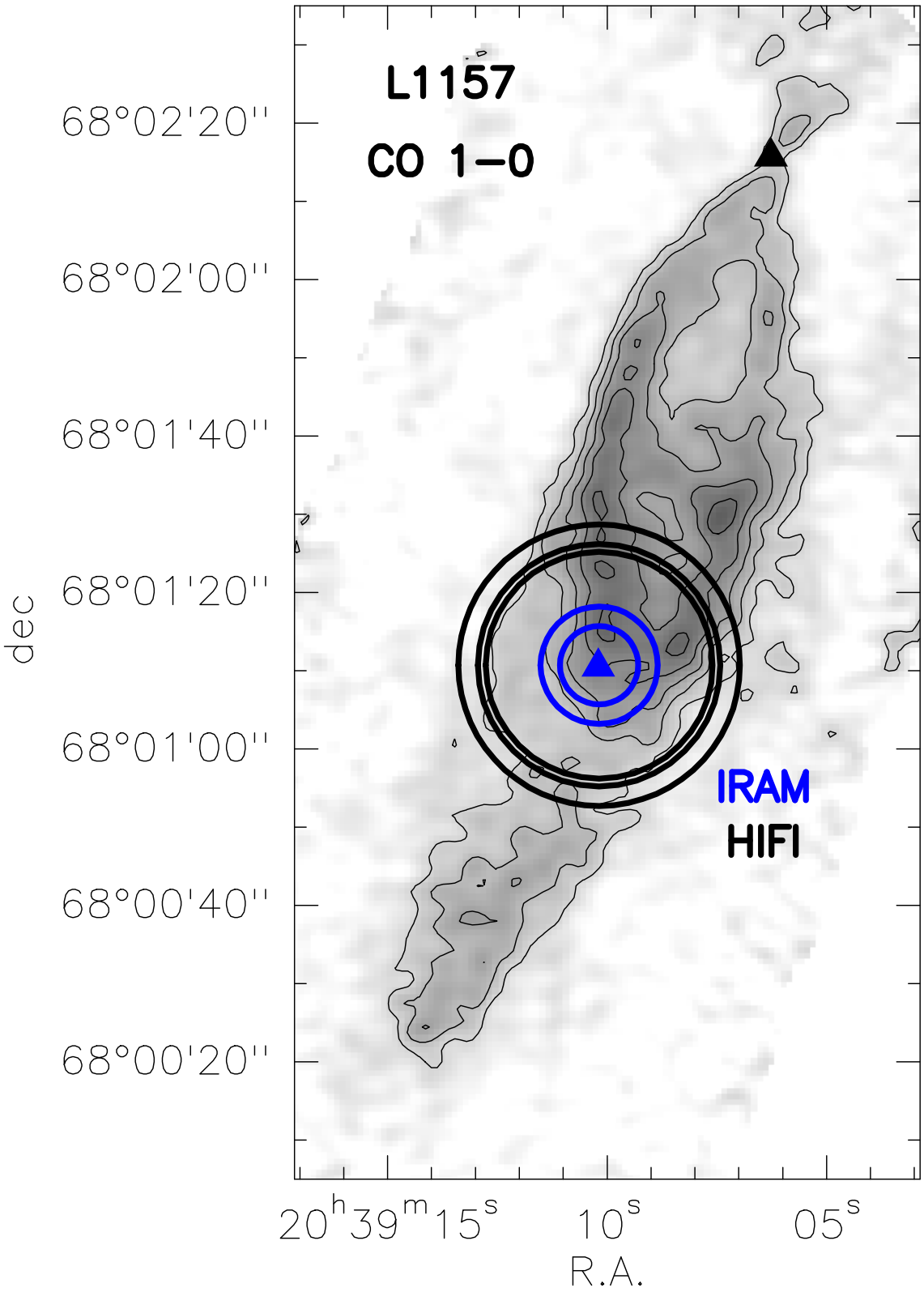

Figure 4.1: CO (1-0) map of the L1157 region (Gueth et al. 1996), including the protostar L1157-mm and the southern outflow. The dashed and solid rings show the beam-sizes of IRAM-30m/EMIR and Herschel/HIFI respectively for the transitions detected. The blue triangle within the rings marks the position of the B1 shock and the other black triangle marks the position of the protostar L1157-mm. Three regions are discussed in the text: g_1 is considered to be the region with the bright CO contours of the bow shock, g_2 the lower intensity emission behind the bow-shock and g_3 the southern disconnected region.

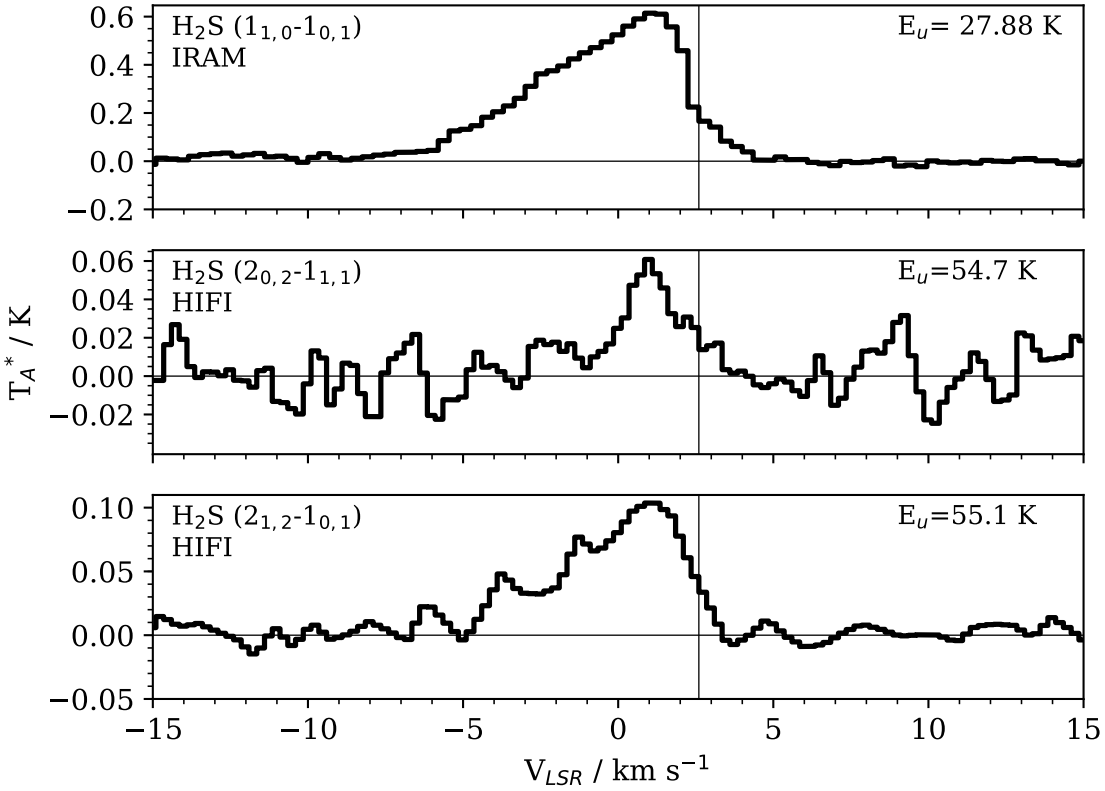

Figure 4.2: Herschel/HIFI and IRAM-30m/EMIR detections of the H_2S main isotopologue. The vertical line indicates the cloud velocity V_{sys} =2.6 km s^{-1}.

Table 4.1: Details of Herschel/HIFI observations.

Frequency (GHz)	Band	Obs_Id	Date
687.3	2a	1342207607	2010-10-28
736.0	2b	1342207611	2010-10-28
582.4	1b	1342181160	2009-08-01

adjusted for wavelength by a Ruze formula given in the same article.

4.3 Results

4.3.1 Detected Lines and Opacities

In total, six lines were detected including $H_2^{34}S$ and HDS as well as the main isotopologue, H_2S. Table 4.2 gives the telescope and spectroscopic parameters relevant to each detected line. Frequencies (ν), quantum numbers, Einstein coefficients (A_{ul}), and the upper state energies (E_u) and degeneracies (g_u) are taken from the JPL spectral line catalog (Pickett 1985). The measured line properties including the velocities V_{min} and V_{max} taken to be

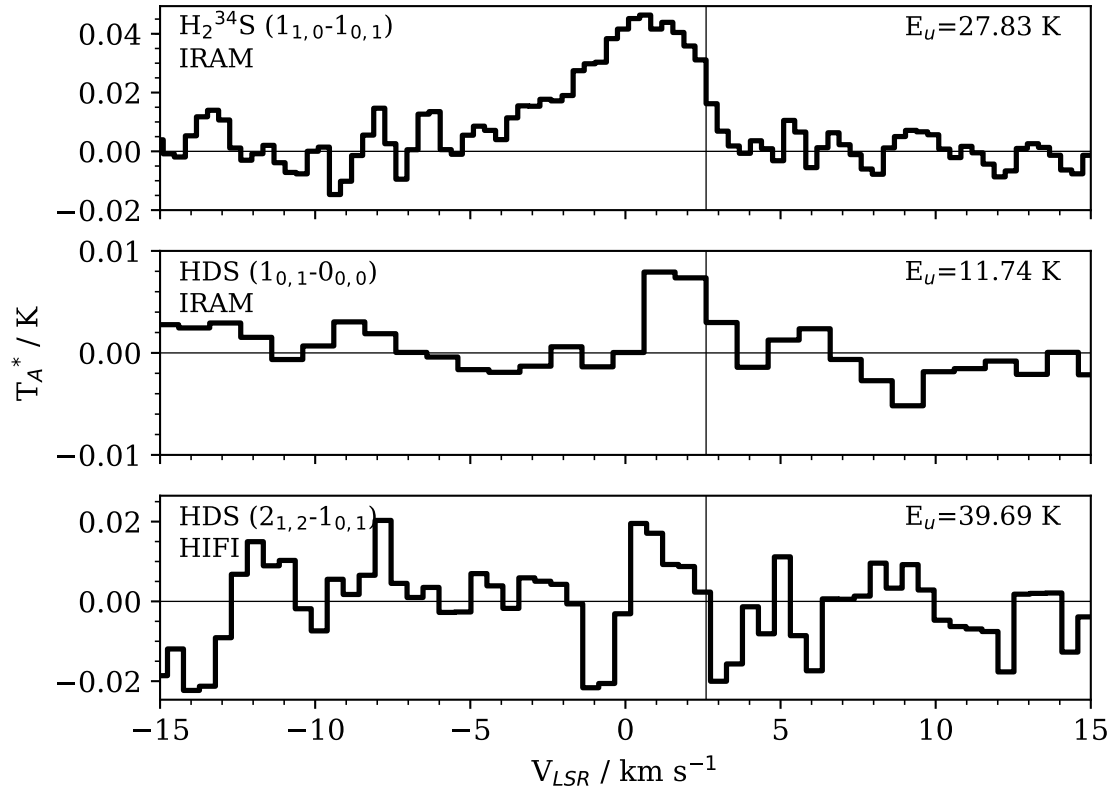

Figure 4.3: Herschel/HIFI and IRAM-30m/EMIR detections of H_2S isotopologues. The HDS lines are at lower spectral resolution than the other detections. The HDS (1-0) spectrum has a resolution of $1\,\mathrm{km\,s^{-1}}$ and HDS (2-1) spectrum has a resolution of $0.5\,\mathrm{km\,s^{-1}}$.

Table 4.2: List of detected lines and the relevant spectroscopic and instrument properties. Ortho and para species are denoted by o- and p- respectively. All spectroscopic data were taken from Pickett (1985).

Molecule	Transition	Freq (GHz)	E_u (K)	g_u	$log(A_{ul})$	Instrument	T_{sys} (K)	θ_{beam} (")	ΔV ($\mathrm{km\,s^{-1}}$)	B_{eff}	F_{eff}
o-H_2S	$1_{1,0}$-$1_{0,1}$	168.7628	27.9	9	-4.57	EMIR	132	15	0.35	0.74	0.93
p-H_2S	$2_{0,2}$-$1_{1,1}$	687.3035	54.7	5	-3.03	HIFI	137	31	0.25	0.76	0.96
o-H_2S	$2_{1,2}$-$1_{0,1}$	736.0341	55.1	15	-2.88	HIFI	317	29	0.25	0.77	0.96
o-$H_2^{34}S$	$1_{1,0}$-$1_{0,1}$	167.9105	27.8	9	-4.58	EMIR	159	15	0.36	0.74	0.93
o-HDS	$1_{0,1}$-$0_{0,0}$	244.5556	11.7	3	-4.90	EMIR	190	10	1.00	0.59	0.92
o-HDS	$2_{1,2}$-$1_{0,1}$	582.3664	39.7	5	-3.18	HIFI	84	36	0.50	0.77	0.96

Table 4.3: Derived parameters of the detected lines. T_{peak} is given in units of T_{mb} and Vmin/Vmax are where lines drop below 3σ levels except for HDS lines where 1σ is used (See Section 4.3.1). Parenthesized values are uncertainties.

Molecule	Transition	T_{peak} (mK)	V_{peak} ($km\,s^{-1}$)	V_{min}/V_{max} ($km\,s^{-1}$)	$\int T_{mb}$ dv ($K\,km\,s^{-1}$)
o-H_2S	$1_{1,0}$-$1_{0,1}$	614 (8)	1.05	-7.90/4.70	4.41 (0.90)
p-H_2S	$2_{0,2}$-$1_{1,1}$	60 (9)	1.00	0.10/2.10	0.20 (0.03)
o-H_2S	$2_{1,2}$-$1_{0,1}$	103 (9)	1.25	-4.15/3.10	0.58 (0.07)
o-$H_2^{34}S$	$1_{1,0}$-$1_{0,1}$	46 (6)	0.65	-1.69/2.96	0.28 (0.06)
o-HDS	$1_{0,1}$-$0_{0,0}$	8 (2)	1.00	0.60/3.60	0.030 (0.008)
o-HDS	$2_{1,2}$-$1_{0,1}$	19 (6)	0.00	0.00/2.50	0.034 (0.009)

the velocities at which the emission falls below the 3σ level, and the integrated emission ($\int T_{MB}dv$) within those limits are shown in Table 4.3. The error quoted for the integrated intensities includes the propagated error from the rms of T_{MB} and the velocity resolution of the spectra as well as nominal calibration errors of 10 and 20% for Herschel-HIFI and IRAM-30m respectively. Note that the HDS spectra are at lower spectral resolution and have less significant detections than the other H_2S transitions, each peaking between the 3 and 4 σ level. For this reason, the velocity limits of the HDS (2-1) transition are taken to be where the peak is above 1σ.

Figures 4.2 and 4.3 show the six lines labelled by their species and quantum numbers. The spectra are given in units of antenna temperature T_a^*. Figure 4.2 shows the three H_2S lines whilst Fig. 4.3 shows the isotopologues. In Fig. 4.2, the H_2S ($2_{1,2}$-$1_{0,1}$) line shows three peaks. The primary peak is at $1.25\,km\,s^{-1}$, which is common to all the spectra. The secondary peak at $-3.75\,km\,s^{-1}$ is consistent with lines detected in L1157-B1 by Lefloch et al. (2010) who found that HCN, NH_3, H_2CO and CH_3OH showed primary peaks at approximately $1\,km\,s^{-1}$ and secondary peaks between -3 and $-4\,km\,s^{-1}$. However, the peak at $-1.25\,km\,s^{-1}$ in the H_2S ($2_{1,2}$-$1_{0,1}$) spectrum is not consistent with any other spectral features and may be due to a contaminant species or simply noise.

From the integrated intensity, the upper state column density, N_u can be calculated as,

$$N_u = \frac{8\pi k\nu^2}{hc^3 A_{ul} ff} \int T_{MB} dv \left(\frac{\tau}{1-e^{-\tau}}\right) \tag{4.1}$$

where ff is a correction factor for the fact the emission does not fill the beam and τ is the optical depth. This clearly requires estimates of the optical depth of each line and the source size from which the filling factor can be calculated.

It is assumed that all the H_2S emission comes from B1. Whilst previous work on L1157-B1 has suggested most emission comes from the walls of the B1 cavity (Benedettini et al. 2013), this has not been assumed and the entire size of B1 is used. Thus, size was taken to be 18" in agreement with the size of B1 in CS estimated by Gómez-Ruiz et al. (2015) from PdBI maps by Benedettini et al. (2013). The validity of this assumption is explored in Section 4.3.2. However, it should be noted that varying the size from 15" to 25" changes $\ln(\frac{N_u}{g_u})$ by less than 1% and encompasses all estimates of the source size from other authors (Lefloch et al. 2012; Podio et al. 2014; Gómez-Ruiz et al. 2015).

The $1_{1,0}$-$1_{0,1}$ transition has been detected in both H_2S and $H_2^{34}S$, allowing the optical depth of L1157-B1 for H_2S to be calculated. For the equivalent transition in a pair of isotopologues, it is expected that N_u would only differ by the isotope abundance ratio if the emission region is the same. A $^{32}S/^{34}S$ ratio, R, of 22.13 was assumed (Rosman and Taylor 1998) and tested by comparing the integrated emission in the wings of the $1_{1,0}$-$1_{0,1}$ transitions; that is all of the emission below $-1\,\mathrm{km\,s^{-1}}$. This emission is likely to be optically thin, allowing us to test the abundance ratio. A ratio of 22±3 was found, consistent with the value taken from the literature. By taking the ratio of the measured integrated line intensities,

$$\frac{1-e^{-\tau}}{1-e^{-\tau/R}} = \frac{\int T_{MB}(^{32}S)dv}{\int T_{MB}(^{34}S)dv} \tag{4.2}$$

and solving for τ, an optical depth for H_2S ($1_{1,0}$-$1_{0,1}$) of τ =0.87 was calculated.

4.3.2 Origin of the Emission

Lefloch et al. (2012) found that the CO emission from L1157-B1 could be fitted by a linear combination of three velocity profiles, associated with three physical components. The profiles were given by $I(v) \propto exp(-|v/v_0|)$ where v_0 is the characteristic velocity of the physical component. The velocities were $12.5\,\mathrm{km\,s^{-1}}$, $4.4\,\mathrm{km\,s^{-1}}$ and $2.5\,\mathrm{km\,s^{-1}}$ which are respectively associated with a J shock where the protostellar jet impacts the B1 cavity, the walls of the B1 cavity and an older cavity (B2). These components were labelled as g_1, g_2 and g_3 and the same notation is used here for consistency. In Figure 4.1, g_1 is considered to be the region with the bright CO contours of the bow shock, g_2 the lower intensity emission behind the bow-shock and g_3 the southern disconnected region. However, it should be noted that this is not based on interferometry and so the assignment is a best

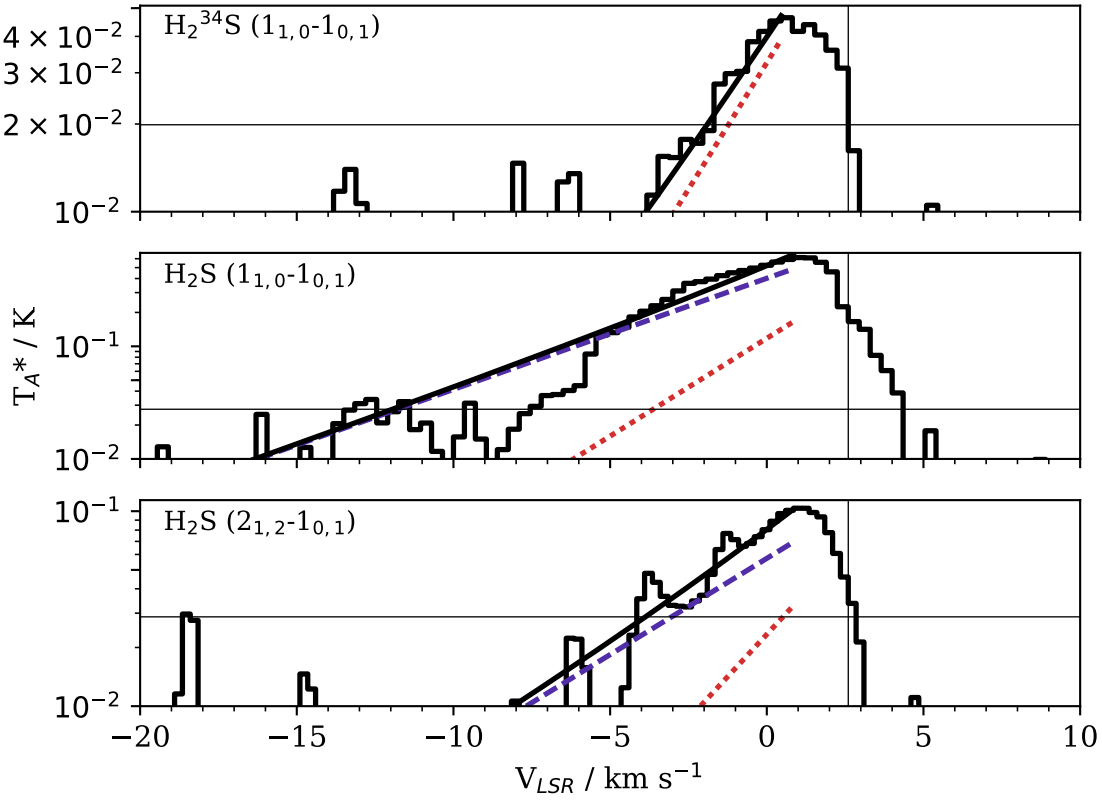

Figure 4.4: Log-linear plots of the well detected transitions. The dashed and dotted fits are $I(v) \propto exp(-|v/v_0|)$ profiles with $v_0 = 4.4\,\mathrm{km\,s^{-1}}$ (g_2) and $2.5\,\mathrm{km\,s^{-1}}$ (g_3) respectively. The solid line is the best fit line, a linear combination of the other two. The third component, g_1 (v_0=12.5 $\mathrm{km\,s^{-1}}$) is not shown as it is not required for the best fit and there is no emission from velocities more blue shifted than $-8\,\mathrm{km\,s^{-1}}$. The vertical line is the cloud velocity, V_{sys} =2.6 $\mathrm{km\,s^{-1}}$ (Bachiller and Pérez Gutiérrez 1997), and the horizontal line marks each the 3σ rms level on each plot.

guess based on the gas properties of the velocity components and the gas properties derived from interferometric studies.

This has also been applied to other molecules. For CS (Gómez-Ruiz et al. 2015), it was found that the g_2 and g_3 components fit the CS lines well with a negligible contribution from the g_1 component except for the high J lines detected with HIFI. The same was found to be true for SO^+ and HCS^+ (Podio et al. 2014). This implies that the majority of emission from the low energy transitions of sulfur bearing molecules comes from the B1 and B2 cavities and is not associated with the J-shock.

The three components have been used to fit the H_2S line profiles and the results are shown in Fig. 4.4. The fit for H_2S ($2_{0,2}$-$1_{1,1}$) is not shown as the detection is not significant enough to be well fitted. Unlike other molecules in the region, the fits for H_2S appear to

be fairly poor, with reduced χ^2 values much greater than 1 for H_2S ($1_{1,0}$-$1_{0,1}$) and the H_2S ($2_{1,2}$-$1_{0,1}$) suffering from the secondary peaks. However, the $H_2{}^{34}S$ isotopologue is well fitted. In each case, only the g_2 and g_3 components are required for the best fit. This implies that, as for CS, the majority of the H_2S emission arises from B1 and B2 cavities affected by the interaction of low-velocity C-shock. Since the g_1 component is negligible in the H_2S lines, the nearby J-shock does not contribute to their emission. This justifies the use of a C-shock model in Section 4.4.2 to reproduce the observed line profiles and measured abundances of H_2S in L1157-B1.

4.3.3 Column Densities and Abundances

The three detected transitions of H_2S allow the excitation temperature and column density of the shocked gas in L1157-B1 to be calculated through use of a rotation diagram (Goldsmith and Langer 1999). Of the three transitions, one is para-H_2S and the other two are ortho. In order to proceed, an ortho-to-para ratio needs to be assumed. Given the lack of further data, the statistical average of 3 is assumed for the ortho-to-para ratio. Reducing this ratio to 1 produced results within error of those presented here for column density and temperature. It is therefore not possible to draw any conclusions about the ortho-to-para ratio from the data available.

The H_2S column density and temperature were calculated through the use of a rotation diagram. For the rotation diagram, the upper state column density, N_u was calculated from Eq. 4.1 assuming all three transitions had the same optical depth, calculated above. The filling factor in Eq. 4.1, ff is uncertain due to the fact that Section 4.3.2 shows that H_2S emission comes partially from the walls of the B1 cavity and partially from the older B2 cavity. For the calculations here, we adopt a source size of 18" but as noted in Section 4.3.1, a size of 25" gave the same result. The rotation diagram is shown in Fig. 4.5 and gave an excitation temperature of (12 ± 1) K. Of the three components discussed in Section 4.3.2, this is most consistent with the low temperature of the g_3 component calculated as $\sim$23 K by Lefloch et al. (2012). They report errors of order 10 K and the excitation temperature from a rotation diagram is typically lower then the gas temperature when the emission is not in LTE (Goldsmith and Langer 1999). Using the JPL partition function values for H_2S (Pickett 1985), a total column density was found to be $N(H_2S)$=$(4.7 \pm 0.4) \times 10^{13}\,\mathrm{cm}^{-2}$.

Bachiller and Pérez Gutiérrez (1997) calculated a fractional abundance of H_2S by

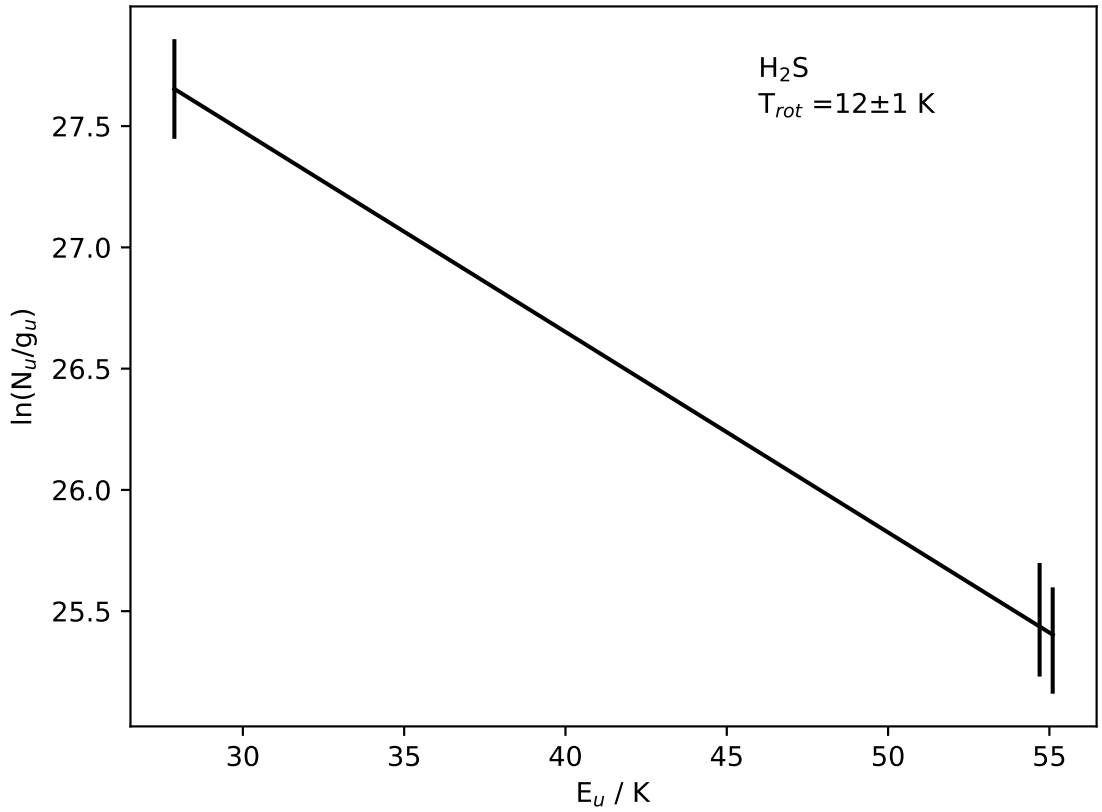

Figure 4.5: Rotation diagram for H_2S. The gradient gives an excitation temperature of 12 K and the intercept gives a column density of $(4.7 \pm 0.4) \times 10^{13}\,\mathrm{cm}^{-2}$.

comparing measured column densities of H_2S to CO and assuming a CO:H_2 ratio of 10^{-4}. They obtained a value of $2.8{\times}10^{-7}$. Given that their H_2S column density was calculated from a single line by assuming a temperature of 80 K and optically thin emission, an updated value has been calculated. For the CO column density, a more recent measurement of N(CO)=$1.0{\times}10^{17}$ cm^{-2} is used (Lefloch et al. 2012). For a H_2S column density of $4.7{\times}10^{13}$ cm^{-2}, a fractional abundance X= 4.7×10^{-8} is found. This is a factor of $\sim$6 smaller than the Bachiller and Pérez Gutiérrez measurement, most likely due to the improved column density derived by using a rotation diagram with three transitions rather than a single line with an assumed temperature.

It should be noted that the critical densities for the two higher frequency transitions are $n_c \sim 10^7\,\mathrm{cm}^{-3}$. Estimates of the average number density in B1 and B2 are of order $n_H \sim 10^5\,\mathrm{cm}^{-3}$. Therefore LTE is unlikely to apply here. This casts doubt on the rotation diagram method and so the radiative transfer code RADEX (van der Tak et al. 2007) was run using the slab model with a range of column densities, gas densities and temperatures to see if similar results would be obtained. H_2 number densities in the range $n = 10^4 - 10^6$

cm^{-3} and temperatures in the range 10-70 K were used based on the values found for g_2 and g_3 with LVG modelling by Lefloch et al. (2012). With these parameters, the best fit found by comparing predicted brightness temperatures to the H_2S lines reported here is $3.0 \times 10^{14}\,cm^{-2}$ at a temperature of 10 K and density $10^5\,cm^{-3}$. Fits with T > 30 K or $n_H \gg 10^5\,cm^{-3}$ were always poor.

4.3.4 The Deuteration Fraction of H_2S

The excitation temperature is further used to make the first estimate of the deuteration fraction of H_2S in an outflow from a low mass protostar. The integrated intensities of the HDS emission lines are used to calculate $\ln(N_u)$ for each transition, again assuming a source of 18". T_{ex}=12±1 K, the value of the partition function, Z, and upper state degeneracy g_u taken from the JPL catalog are then used to find a column density for HDS as,

$$ln(N) = ln(\frac{N_u}{g_u}) + ln(Z) + \frac{E_u}{kT_{ex}} \tag{4.3}$$

By averaging the column density obtained from each of the two transitions, a column density of 2.4±1.2×10^{12} cm^{-2} is found. This corresponds to a deuteration fraction for H_2S of 5.1±1.3×10^{-2}. As these abundances are an average over the beam, this is likely to be a lower limit of the true deuteration on the grains. However, it is comparable to level of deuteration measured for other species in L1157-B1. For example, the methanol deuteration fraction was found to be 2×10^{-2} by Codella et al. (2012). Further, Fontani et al. (2014) detected HDCO, CH_2DOH with the Plateau de Bure interferometer and compared to previous measurements of CH_3OH and H_2CO. They obtain higher deuteration fractions for H_2CO and CH_3OH, reporting 7×10^{-2} for H_2CO and 3×10^{-2} for CH_3OH.

4.4 Sulfur Chemistry in the B1 Shock

4.4.1 Comparison of Line Profiles

In the previous section it is postulated that H_2S arises from the B1 and B2 cavity like CS. In order to test this hypothesis, the emission of these species is compared to see if they show similar behaviour. Figure 4.6 shows the ratios of the line temperatures for the H_2S ($1_{1,0}$-$1_{0,1}$) transition with the CS (3-2) and NH_3 (1-0) transitions. This allows us to better

compare the line profiles and the evolution of the molecular abundances of the different species considered in this section and in Section 4.4.2. The spectra have been re-sampled to common velocity bins. The H_2S ($1_{1,0}$-$1_{0,1}$) transition was chosen as it is both less noisy than the other H_2S transitions and closer in excitation properties to the available CS and NH_3 transitions.

The CS transition in Fig. 4.6a is the CS (3-2) transition at 146.97 GHz; it has an upper level energy of $E_u = 14.1$ K. Figure 4.6a shows that the CS (3-2) and H_2S ($1_{1,0}$-$1_{0,1}$) profiles differ by a factor of $\sim$10 at higher velocities. Assuming that the line ratio follows the behaviour of the abundance ratio between these two species, this may imply that H_2S is not as abundant as CS at higher velocities and therefore raises the possibility that the H_2S and CS emission do not entirely arise from the same region. This pattern is attributed to chemical differences between the molecules and explored in Section 4.4.2.

The NH_3 spectrum in Fig. 4.6b is the NH_3 (1-0) line at 572.49 GHz. It has an upper level energy of $E_u = 27.47$ K which is comparable to the upper level energy of the H_2S ($1_{1,0}$-$1_{0,1}$) transition. These two transitions are compared due to their similar excitation properties and strong detections; the other H_2S spectra are much noisier. From Fig. 4.6b, we find that the H_2S and NH_3 intensities (and thus, their abundances) differ by less than a factor of 3 throughout the post-shock gas, which suggests that H_2S and NH_3 come from the same region and behave similarly. It should be noted that the NH_3 line has been measured within a larger beam than H_2S and thus, the NH_3 line may include emission from a larger area in the L1157-B1 bowshock.

4.4.2 Comparison with Chemical Models

Though the velocity fits are poor, the H_2S spectra do not require a g_1 component to be well fitted and have low terminal velocities and so are not likely to be associated with the J shock from L1157-mm's outflow (see Section 4.3.2). Extensive efforts have been made to model the dynamics of L1157-B1 with C-shocks (e.g. Gusdorf et al. 2008; Flower and Pineau des Forêts 2012) and have proven successful. The line profiles of H_2S appear to be consistent with the shapes predicted for other molecules from a parameterized C-shock model in Jiménez-Serra et al. (2008) and the behaviour of other species such as H_2O and NH_3 have been successfully modelled by coupling the same shock model with a chemical code (Viti et al. 2011). Hereafter it is thus assumed that the sulfur chemistry observed toward L1157-B1 can be modelled by a C-type shock. Through this modelling,

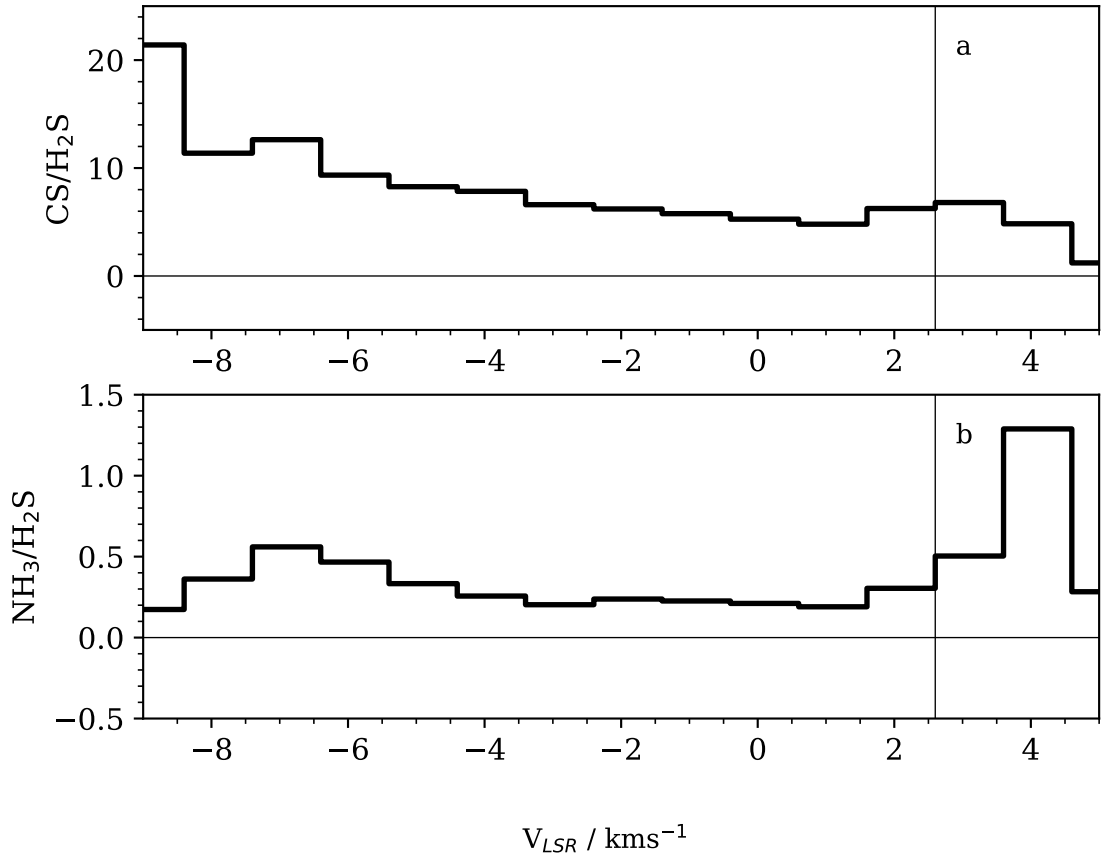

Figure 4.6: Emission ratios CS (3-2)/H_2S (a) and NH_3 (1-0)/H_2S (b). The H_2S ($1_{1,0}$-$1_{0,1}$) line is used in both. All the spectra have been resampled into bins with a common resolution of $1\,km\,s^{-1}$ centred at $2.6\,km\,s^{-1}$. The 3σ velocity limits of the H_2S line are used to set the x-axis as they give the smallest velocity range in each case.

the question of whether H_2S is formed mainly on the grains or in the gas-phase during the passage of a C-type shock is investigated. The model used is the C-shock parameterization of UCLCHEM using parameters found by Viti et al. (2011) as the best fit to H_2O and NH_3. This is considered more reasonable than fitting for the physical parameters to the single abundance derived for H_2S.

The model is run in two phases. Phase 1 is typical for UCLCHEM and follows the formation of a molecular cloud through gravitational collapse where freeze out onto dust grains and surface chemistry set the abundances of the gas-phase and grain adsorbed species. This gives ice mantle and gas-phase abundances that are consistent with the network for Phase 2 rather than assumed.

In Phase 2, the propagation of a C-type shock from the protostellar outflow is modelled according to the Jiménez-Serra et al. (2008) parameterization as discussed in Chapter 2.

The physical structure of the shock is parameterized as a function of the shock velocity (V_s), and the H_2 gas density of the pre-shock gas. The magnetic field used in the model is 450 μG, transverse to the shock velocity, and it has been calculated following the scaling relation $B_0(\mu G) = b_0\sqrt{n_0(cm^{-3})}$ with $b_0 = 1$ following Draine et al. (1983) and Le Bourlot et al. (2002). Note that in this one case, the density n_0 is given as the density of hydrogen nuclei. The maximum temperature of the neutral fluid attained within the shock ($T_{n,max}$) is taken from Figures 8b and 9b in Draine et al. (1983). The sputtering of the grain mantles is simulated in the code by introducing a discontinuity in the gas-phase abundance of every molecular species once the dynamical time across the C-shock has reached the "saturation time-scales". The "saturation times" were defined by Jiménez-Serra et al. (2008) as the time-scales at which the relative difference in the sputtered molecular abundances between two consecutive time steps in the model are less than 10%, and represent a measure of the time-scales for which almost all molecular material within the mantles is released into the gas-phase. For the saturation times for H_2S and the other sulfur-bearing species, we adopt those already derived for SiO coming from the mantles (see Table 5 in Jiménez-Serra et al. (2008)). The mathematical expression for the sputtering of the grain mantles for any molecular species is the same except for the initial solid abundance in the ices (see Eqs. B4 and B5 in the same paper). Consequently, species differ in the absolute scale in the final abundance sputtered from grains but not the time-scales at which they are injected into the gas-phase.

The best fit model from Viti et al. (2011) is used to set the shock parameters. In this model, the C-shock has a speed of v_s=40 km s^{-1} and the neutral gas reaches a maximum temperature of $T_{n,max}$=4000 K in the post-shock region. This reproduced the observed behaviour of NH_3 and H_2O in the work by Viti et al. (2011) and since the work on which this chapter is based was published, it has also been used to explain the abundances of NO (Codella et al. submitted.), DCN and HCN (Busquet et al. 2017), and PO and PN (Lefloch et al. 2016) . It was shown by Le Bourlot et al. (2002) and Flower and Pineau des Forêts (2003) that C-shocks can indeed develop in a medium with a pre-shock density of 10^5 cm^{-3} and magnetic induction B_0=450 μG (or b_0=1; see their Figures 1 and 5).

Although the terminal velocity of the H_2S shocked gas observed in L1157-B1 is only about -10 km s^{-1}, the higher shock velocity of v_s= 40 km s^{-1} used in the model is justified by the fact that other species observed in the region such as H_2O and CO show broader emission, even reaching terminal velocities of -30 km s^{-1} and -40 km s^{-1} (Lefloch et al.

2010, 2012). These are expected to be more reflective of the shock velocity as these species are not destroyed at the high temperatures produced by the shock and so remain abundant out to high velocities (Viti et al. 2011; Gómez-Ruiz et al. 2016).

Recent shock modelling assuming perpendicular geometry of the shock predicts thinner post-shock regions, and consequently higher T_{max} in the shock, than those considered here under the same initial conditions of pre-shock gas densities and shock velocities (see e.g. Guillet et al. 2011; Anderl et al. 2009). However, MHD simulations of oblique shocks (Van Loo et al. 2009) seem to agree with the lower estimates of $T_{n,max}$ used here and therefore, the treatment proposed by Jiménez-Serra et al. (2008) is adopted. The validation of this parameterization is discussed at length in Jiménez-Serra et al. (2008). The interested reader is referred to that paper for details of the C-shock modelling and to Chapter 2 for details on its implementation in UCLCHEM.

In the model, the sulfur network has been expanded following Woods et al. (2015) to investigate the composition of the ice mantles. The first three versions of the network were taken directly from Woods et al. (2015). The behaviour of sulfur bearing species are as follows (see Table 4.5):

- Model A Species froze as themselves.
- Model B Species immediately hydrogenated.
- Model C Species would freeze 50% as themselves and 50% hydrogenated.
- Model D Any species for which a reaction existed to produce OCS on the grains was set to freeze out entirely as OCS.
- Model E Species would freeze 50% as themselves and 50% as OCS if possible.

The injection of the ice mantles into the gas-phase by sputtering occurs once the dynamical time in the C-shock exceeds the saturation time, i.e. when t_{dyn} >4.6 years. This greatly decreases the computational complexity without changing the chemistry. No grain-grain interactions are taken into account due to the computational costs.

The parameter values for the C-shock in the model are given in Table 4.4. Note network D is not reflective of real chemistry but rather takes the extreme case of highly efficient grain surface reactions allowing frozen sulfur, carbon and oxygen atoms to form OCS.

Figure 4.7 shows the results from four of the networks used to investigate the conditions of the shock in L1157-B1 plotted as function of the distance into the shock, log(Z). In each

Table 4.4: Model parameters.

$n(H_2)$	$1 \times 10^5\,cm^{-3}$
V_s	$40\,km\,s^{-1}$
t_{sat}	4.6 yr
$T_{n,max}$	4000 K
B_0	450 μG

Note: $n(H_2)$ is the pre-shock hydrogen density, V_s is the shock speed, t_{sat} is the saturation time, $T_{n,max}$ is the maximum temperature reached by the neutral gas.

Table 4.5: Branching ratios for the freeze out routes of example sulfur bearing species in each model. # indicates a frozen species.

Model	**S**	**HS**	**CS**
Model A	100% #S	100% #HS	100% #CS
Model B	100% #H_2S	100% #H_2S	100% #HCS
Model C	50% #S 50% #H_2S	50% #HS 50% #H_2S	50% #CS 50%#HCS
Model D	100% #OCS	50% #HS 50% #H_2S	100% #OCS
Model E	50% #OCS 50% #H_2S	50% #HS 50% #H_2S	50% #OCS 50% HCS

case only Phase 2 is shown, the initial abundances at log(Z)=14 are the final abundances of Phase 1 from each network. As explained above, sputtering occurs once t_{sat} is reached, releasing mantle species into the gas-phase. This sputtering is responsible for the initial large increase in abundance for each species at around log(Z)=14.8. A further increase can be seen in the H_2S abundance as the peak temperature is reached at log(Z)=15.8, after which H_2S is destroyed through gas-phase reactions as the gas cools. Most of this destruction is due to the reaction,

$$H + H_2S \rightarrow HS + H_2.$$

It is worth noting that the H_2S abundance remains low over thousands of years in cold gas if the model is allowed to continue to run after the shock passage.

Comparing the predicted fractional abundance of H_2S in each model, Models A and D are the best fit predicting $X(H_2S) = 7.8\times10^{-8}$ and $X(H_2S) = 7.3\times10^{-8}$ respectively. The average fractional abundance of each model is calculated as an average over the dissipation

length: the whole width of the shock. The fractional abundance is given here with respect to the H_2 number density. Model B predicts an average H_2S abundance of $X(H_2S) = 1\times10^{-6}$ and model E gives $X(H_2S) = 6\times10^{-7}$. These are an order of magnitude higher than the observed fractional abundances of H_2, which disfavours these models. Overall, the predicted abundances imply that if too large a proportion of sulfur is hydrogenated on the grain, the gas-phase H_2S abundance is over-estimated once the grain material is released into the gas-phase. These results are dependent on the assumed CO abundance, which was taken to be $X_{CO}=10^{-4}$, a standard assumption which agrees with the model abundance of CO (see Fig. 4.7).

Furthermore, it is expected that excitation and beam effects are constant between two transitions for all emission velocities. Therefore, it can be assumed that any change in intensity ratio between the transitions of two species reflects a change in the abundances of those species. Model D gives a varying ratio of H_2S to NH_3 which is at odds with the approximately flat intensity ratio shown in Fig. 4.6. Model A, on the other hand, shows H_2S and NH_3 varying in similar ways, which would give a constant ratio.

In contrast, CS remains at a relatively constant fractional abundance in the model throughout the shock and so one would expect a large difference between the intensities of CS and H_2S at high velocities, where the gas is warmer. This is consistent with the velocity limits of the detections and the ratio plots shown in Fig. 4.6. None of the H_2S spectra remain above the rms at more than $V = -8\,\mathrm{km\,s^{-1}}$ but Gómez-Ruiz et al. (2015) report their CS (3-2) line extends to $V = -19\,\mathrm{km\,s^{-1}}$. We note that the differences in terminal velocities between CS and H_2S are not due to excitation effects but to real differences in their abundances as the CS (7-6) line, reported in the same work, reaches $V=-16\,\mathrm{km\,s^{-1}}$ and has E_u, g_u and A_{ul} that are similar to the H_2S ($2_{1,2}$-$1_{0,1}$) transition.

Whilst the comparison between the fractional abundances given by the models and the data is promising, it must be remembered that the networks used are limiting cases and the model is a 1D parameterization. From the results of models A and D it is clear that the observed H_2S emission requires that no more than half of the sulfur on the grains be in H_2S. However, observations of other sulfur bearing species are required to really differentiate between the models. This is explored further in Chapter 5.

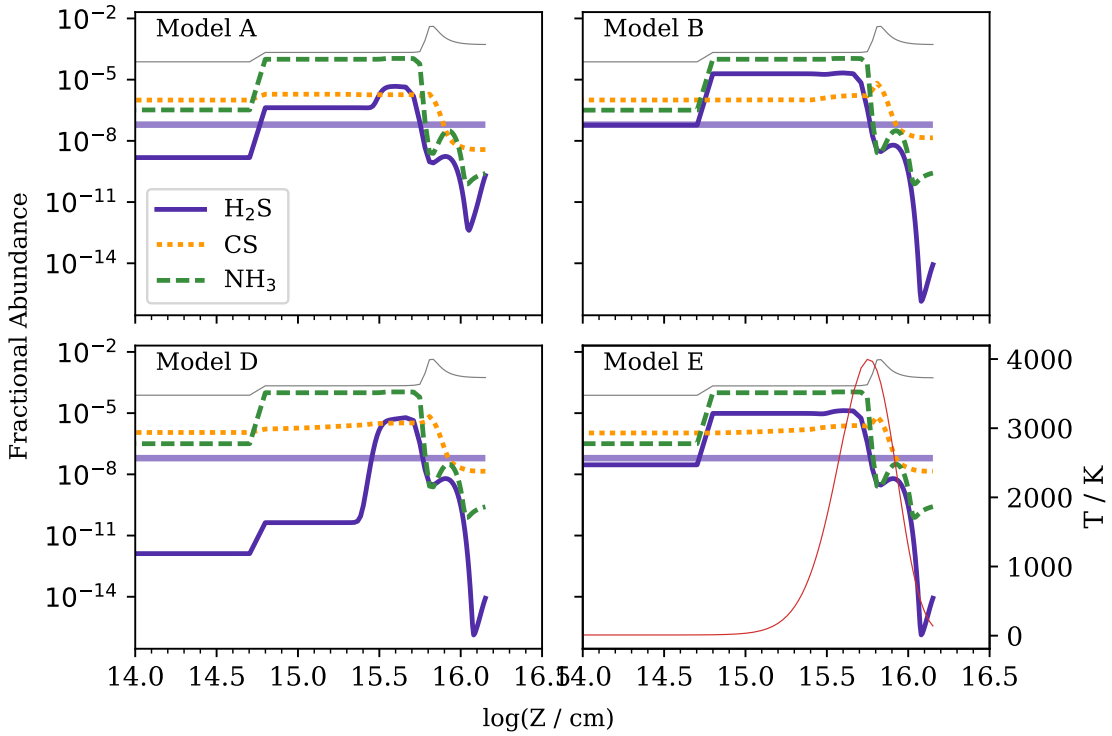

Figure 4.7: Fractional abundances of H_2S, NH_3 and CS as a function of distance into the shock for the different networks, the wide faded band is the H_2S derived from the rotation diagram. Plots are shown only up to the dissipation length, described in Section 4.4.2. The panels show: A) Freeze out to same species; B) freeze out to hydrogenated species; D) efficient OCS freeze out; E) 50% into routes B and D. The grey line in each panel shows the CO fractional abundance, demonstrating the validity of assuming X_{CO}=10^{-4}. In the final panel, the red line shows the neutral gas temperature through the shock.

4.5 Conclusions

In this work, H_2S in the L1157-B1 bowshock has been studied using data from the Herschel-CHESS and IRAM-30m ASAI surveys. Six detections have been reported: H_2S ($1_{1,0}$-$1_{0,1}$), ($2_{0,2}$-$1_{1,1}$) and ($2_{1,2}$-$1_{0,1}$); $H_2^{34}S$ ($1_{1,0}$-$1_{0,1}$); and HDS ($1_{0,1}$-$0_{0,0}$) and ($2_{1,2}$-$1_{0,1}$). The main conclusions are as follows.

i) The H_2S gas in L1157-B1 has a column density of $N(H_2S)$=$(4.7 \pm 0.4) \times 10^{13}$ cm^{-2} and excitation temperature, T=12±1 K. This is equivalent to a fractional abundance of X(H_2S)~4.7×10^{-8}. These values are based on opacity measurements using the $H_2{}^{34}S$ intensity and an assumed size of 18".

ii) The isotopologue detections allow the deuteration fraction of H_2S in L1157-B1 to be calculated. A HDS:H_2S ratio of 5.1×10^{-2} is found.

iii) The state of sulfur on dust grains is explored by the use of a gas-grain chemical

code with a C-shock where the freeze out routes of sulfur bearing species are varied in order to produce different ice compositions. These frozen species are then released into the gas by the shock and the resulting chemistry is compared to the measured abundances and intensities of molecules in L1157-B1. It is found that the best fit to the data is when no more than half of each sulfur bearing species hydrogenates as it freezes. Further work with a more comprehensive dataset of emission from sulfur bearing species in L1157-B1 is required to truly understand the grain composition.

This page was intentionally left blank

Chapter 5

Sulfur in the L1157-B1 Bow Shock

The work presented in this chapter is based on the paper by Holdship et al. (submitted), in collaboration with S.Viti, C. Codella, I.Jimenez-Serra, B. Lefloch, L. Podio, M. Benedettini, F. Fontani, M. Tafalla, R.Bachiller and C. Ceccarelli.

5.1 Introduction

In the previous chapter, observations of L1157-B1 in H_2S were presented and used to study the contents of the grains. However, the study of a single species limits what it is possible to learn. For example, it was concluded that H_2S could not be a major carrier of sulfur on the grains but it could not be stated whether this was consistent with the finding of Podio et al. (2014), in which it is suggested most of the sulfur on the grains should be in OCS. Clearly, a more complete inventory of the sulfur in L1157-B1 would resolve this problem.

A further problem in the previous chapter is the spatial resolution of the observations. Despite its identification as a bow-shock, there is clear clumpy substructure in the region (Benedettini et al. 2007) with different chemical species tracing only the clumps or the region as a whole. An effort has been made to resolve these diverse emitting components despite the fact they are contained in a single telescope beam. Lefloch et al. (2012) found that CO emission from the region could be separated into components based on an intensity-velocity relationship, $I(v) \propto \exp\left(-|v/v_0|\right)$. This is a largely empirical relationship based on the work of Downes and Cabrit (2003), who showed that simulations

of jet driven molecular outflows could be fitted in this way. Lefloch et al. (2012) found the highest excitation CO lines could be fit by this relationship with v_0=12.5 km s^{-1} and called this component g_1. Fitting this line to the high velocity emission of lower excitation lines, it was then found the remaining emission could mostly be fit by a second component (g_2), v_0=4.4 km s^{-1}. The very lowest excitation lines were then left with residual emission well fit by v_0=2.5 km s^{-1} (g_3).

It was therefore arguable that three physical gas components were contained in the telescope beam. With the g_1 component hot enough to excite high-J lines the other components could not, the g_2 able to reach mid-J transitions and only the lowest J transitions excited by g_3. LVG fitting to the emission in of these components corroborated this view, predicting high temperatures for g_1 and very low temperatures for g_3. Components g_2 and g_3 were found to be good fits to CS emission in the region (Gómez-Ruiz et al. 2015) as well as HCO^+, SO^+ and HCS^+ (Podio et al. 2014), with similar gas properties derived from LVG analysis. Finally, it was found that H_2O emission required four different gas components to make good LVG fits to the observed emission in L1157-B1 (Busquet et al. 2014). The first three were responsible for most of the emission and matched the properties derived from the velocity components.

The clumps in the L1157 outflow are rich in sulfur-bearing species. B1 was shown to be well defined in OCS, ^{34}SO and CS emission. SO^+ and SiS were discovered for the first time in a shock in L1157-B1 (Podio et al. 2014, 2017), SO^+ being part of a search for molecular ions in which HCS^+ was also detected. Overall, L1157-B1 provides a rich source of data on sulfur-bearing species with which to advance our understanding of sulfur chemistry, particularly of the form of sulfur that has been depleted from the gas-phase.

In this chapter, observations of six sulfur-bearing species are presented. Multiple transitions of CCS, H_2CS, OCS, SO and SO_2 have been observed along with isotopologues of SO and SO_2. An attempt is made to fit the velocity components discussed above to the best detected species in an effort to treat the emitting components separately. The column density and rotational temperature of these species are extracted from radiative transfer modelling and rotation diagrams of their transitions and those are converted to fractional abundances in order to compare them with abundances derived from chemical modelling. In Section 5.2, details of the observation and data reduction are given. In Section 5.3, the properties of the emitting gas are discussed from the radiative transfer fitting. In Section 5.4, the observations are compared to chemical models and finally the

conclusion is given in Section 5.5.

5.2 Observations & Processing

5.2.1 IRAM-30m Observations

The data presented here were collected as part of the IRAM large programme ASAI[1](Lefloch et al., in prep), which included a systematic search for lines of sulfur-bearing species between 80 and 350 GHz. The data includes over 140 detected transitions of six species: CCS, H_2CS, OCS, SO, SO_2 along with the ^{34}S isotopologues of SO and SO_2. These were obtained observing the L1157-B1 bowshock, with pointed co-ordinates $\alpha_{J2000} = 20^h39^m10.2^s$, $\delta_{J2000} = +68°1'10.5''$, which is $\Delta\alpha = +25".6$, $\Delta\delta = -63".5$ from L1157-mm. Pointing was monitored using NGC7538 and found to be stable. The pointing was checked regularly and corrections were typically less than 3".

The data were obtained using the IRAM-30m telescope's EMIR receivers with the Fourier Transform Spectrometer (FTS) and WILMA backends. These gave spectral resolutions of 200 kHz and 2 MHz respectively. Where intensities are given in T_{MB}, the efficiencies required for this conversion (B_{eff} and F_{eff}) were interpolated from the values given in Table 2 of Greve et al. (1998).

5.2.2 Line Properties

In Appendix A, the intenstity-velocity spectrum of every detected line is plotted. A comprehensive list of all detected transitions for every molecule and their measured line properties is then tabulated in Appendix B. For each spectrum, the rms of the whole spectrum was calculated and emission peaks were identified by looking for channels above twice that value. Windows around these were removed from the spectrum and the remaining spectrum was averaged to find the rms noise.

Lines were identified by comparing the frequencies of emission peaks to the JPL catalog (Pickett 1985). The minimum and maximum velocity (V_{min},V_{max}) of those peaks were found by moving away from the peak until the signal dropped below three times the rms noise value. The V_{min} and V_{max} of the highest signal to noise line of each species was used to set the bounds for integration. The integrated emission reported for each spectrum is the emission between these limits. It appears that all of the sulfur-bearing

[1]http://www.oan.es/asai

species have very similar line profiles. For all species, both the strongest spectrum and a stacked spectrum of all transitions were above the rms between V_{min} = -8 $km\,s^{-1}$ and V_{max} = 5 $km\,s^{-1}$. The exception is SO which displays secondary emission that is analysed separately in section 5.3.3. The error on the integrated emission combines the temperature rms, the velocity resolution and a nominal 20% calibration error. This is then propagated through for all reported values. All of these values are reported in Appendix B.

5.2.3 Radiative Transfer and LTE Treatment

Where possible, the radiative transfer code RADEX (van der Tak et al. 2007) was used to estimate the column density of each molecule and the properties of the emitting gas. The species H_2CS, OCS, SO and SO_2 have collisional data available in the LAMDA database[2](Schöier et al. 2005) and so these were modelled with RADEX.

For H_2CS, the transitions were separated into ortho and para H_2CS. Six transitions were then eliminated from the data set as they are the combined flux of multiple transitions with overlapping frequencies and the same spectroscopic properties. This left nine o-H_2CS and eight p-H_2CS transitions, which was a sufficient number of data points to strongly constrain the gas temperature and column density.

For the parameter estimation, the python package PyMultiNest (Buchner et al. 2014) was used. This is a package for nested sampling which was used to infer the gas temperature, gas density and molecular column density. Nested sampling is an algorithm for Bayesian parameter estimation in which the parameter space is sampled according to the prior distribution rather than in a random walk. This is less efficient than algorithms like Metropolis-Hastings but less prone to finding only local maxima in the probability distribution. The line width was not found to affect the results and so was left out of the fitting procedure. The likelihood of any given set of parameter values was calculated as $\mathcal{L} = \exp(-\chi^2/2)$. The value of χ^2 is calculated as the sum of the squared difference between the RADEX predicted flux and the measured total flux of each transition, each divided by the squared uncertainty in the measured flux. The final outputs of the nested sampling routine are the marginalized and joint probability distributions for each fitted parameter, these are shown in Appendix C. In Section 5.3 the reported values are the most likely values from the marginalized probability distributions and the given errors represent the interval containing 67% of the probability density.

[2]http://home.strw.leidenuniv.nl/~moldata/

RADEX assumes that the source fills the beam which is unlikely to be the case for the species reported here. Therefore, the flux of each transition was adjusted by a filling factor of the form,

$$ff = \frac{\theta_S^2}{\theta_{MB}^2 + \theta_S^2} \tag{5.1}$$

where θ_{MB} and θ_S are the beam and source sizes respectively (Roberts et al. 2010). The beam size is derived from the frequency using the formula θ_{MB} =2460"/frequency(GHz) (Greve et al. 1998). For the source, CS maps from Benedettini et al. (2007) were used to estimate a size of 20". This size is likely to be different for each species and the same work showed OCS emission from a considerably smaller region. However, without interferometric maps of each species in each transition, some assumptions must be made and, ultimately, the values from the RADEX fits change by only a factor of a few when no filling factor is used and are often within the reported error bars.

The rotational temperatures and column densities of each species were also calculated through use of rotation diagrams and this is the only estimate of the CCS column density, as collisional data is not available for this species. For the rotational diagrams, the upper state number density for each transition was calculated from the integrated emission using,

$$N_u = \frac{8\pi k\nu^2}{hc^3 A_{ul} ff} \int T_{MB} dv, \tag{5.2}$$

with spectroscopic parameters taken from the JPL catalog (Pickett 1985). For all transitions, we assume that the emission is optically thin. A more detailed discussion of rotation diagrams is given in Section 1.6.1 and interested readers are referred to Goldsmith and Langer (1999). From plots of $\ln(N_u)$ against E_u, the column density and rotational temperature of each species can be found.

The RADEX column densities for each molecule, and the column density from the CCS rotation diagram, are reported in Table 5.1. The rotation diagrams for each molecule are in Section 5.3 with rotation diagrams produced from the best fit RADEX models overplotted to give the reader a sense of the accuracy of the derived gas properties and column densities. The column densities can be converted to a fractional abundance with respect to H_2 by assuming a CO abundance of 10^{-4} and comparing the species column density to $N(CO)=1.0 \times 10^{17} cm^{-2}$ (Lefloch et al. 2012) and these are also given in Table 5.1.

5.2.4 Velocity Components

As discussed above, previous work on observations of L1157-B1 have shown that certain molecules such as CO (Lefloch et al. 2012) and CS (Gómez-Ruiz et al. 2015) have velocity profiles that are well described as the sum of three components. These components follow velocity profiles of the form $I(v) = I(0)\exp(-|v/v_0|)$ where v_0 is some characteristic velocity. These components have been shown to have different gas properties in through LVG modelling and if the sulfur-bearing species can be analysed in this way then a clearer view of their chemistry may emerge.

An attempt has therefore been made to fit similar velocity components to the emission of SO and SO_2, which have the highest signal to noise ratio and most detected lines of the molecules presented here. If the components are responsible for the emission of either species, every line will be a sum of contributions of the three components. However, there are a number of complications. For SO, the secondary emission discussed in Section 5.3.3 emerges more strongly in higher excitation conditions. The approach taken by Lefloch et al. (2012) was to fit the highest J transitions first, as they are only excited by the hottest component. Not only does the secondary emission prevent this, but it also considerably limits the velocity range over which the fits can be made.

It is not clear whether SO_2 shows secondary emission, possible secondary peaks have been identified but at very low signal to noise. Therefore, it can be assumed that any secondary emission will not effect velocity fits to the SO_2 lines. Two methods were attempted to fit SO_2. Firstly, best fit velocity profiles of $I(v) = I(0)\exp(-|v/v_0|)$ were found through χ^2 minimization with a single varying v_0. It was expected that high J SO_2 lines would have a v_0 similar to either the highest J CO lines (g_1, $12.5\,\mathrm{km\,s^{-1}}$) or the g_2 component which was the best fit to the highest J CS emission. These could then be fit to the higher velocity emission of each spectrum and removed so that the residual emission could be fit by g_3. However, neither of these hypotheses held true so a different method was required to fit the emission.

Secondly, a blind fit was made in which PyMultiNest was used to find the three most likely velocity components. To evaluate the likelihood of any set of velocity components, each spectrum was fit by summing the velocity components and varying the contribution from each to minimize the χ^2 value. Once these contributions were determined for every spectrum, the combined χ^2 value for all spectra was calculated and the likelihood of the

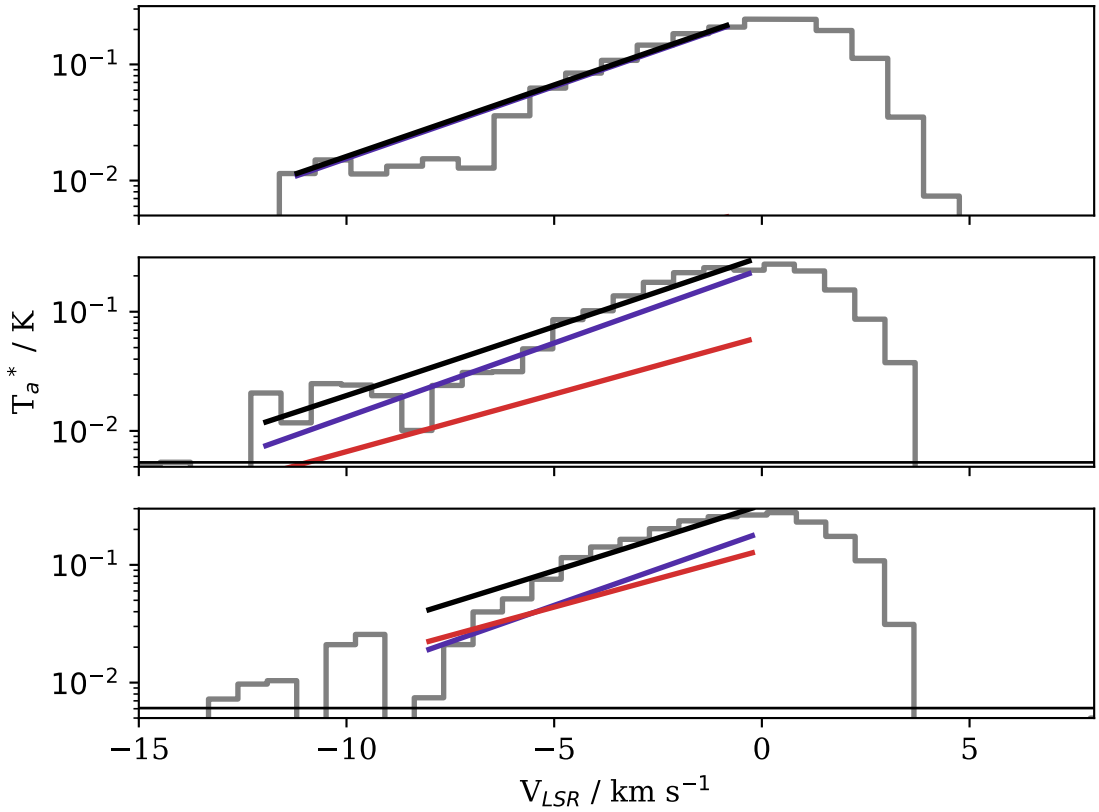

Figure 5.1: Component fits to the three brightest SO_2 lines. The red line is the $4.5\,\mathrm{km\,s^{-1}}$ component and the purple is $3.5\,\mathrm{km\,s^{-1}}$ component. The black is the sum the of the two.

velocity components was taken to be $\mathcal{L} = \exp(-\chi^2/2)$.

If the velocity components found for other molecules were good approximations to the SO_2 emission, the procedure would find the most likely values of the characteristic velocities to be $12.5\,\mathrm{km\,s^{-1}}$, $4.4\,\mathrm{km\,s^{-1}}$ and $2.5\,\mathrm{km\,s^{-1}}$. It would also be possible for SO_2 to trace completely different gas to CO and then a different velocity component would provide a good fit.

No satisfactory fit was found. The most likely velocities were $4.5\,\mathrm{km\,s^{-1}}$ and $3.0\,\mathrm{km\,s^{-1}}$ which were reasonably close to g_2 and g_3. The probability distribution of the third velocity component was not peaked, implying it was not needed for the best fits. Figure 5.1 shows these fits for the three strongest SO_2 lines. However, it is important to note that these characteristic velocities are the best fit under the assumption that the spectra can be described as the combination of three exponential velocity profiles. That is not to say the best fits are good fits. χ^2 values were calculated for the best fit velocities and were all greater than 10. It therefore seems that SO_2 is not well described by these simple velocity components.

The exact reason for this is not clear. However, it is worth noting that the species which are well fitted in this way (CO, CS, H_2O) are also species that, in the shock models presented in Chapter 2, are not greatly changed through the shock, whereas in those models SO_2 varies through the shock.

5.3 Results

5.3.1 Bulk Gas Properties

Whilst the excitation temperatures of each detected molecular transition can be found from a rotation diagram and the column density can be estimated, it is useful to estimate how far from LTE these molecules deviate and to investigate the properties of the emitting gas as a whole. Further, since the beam encompasses a large emitting region, analysing each species separately can shed light on whether a single gas component is responsible for the bulk of sulfur emission or whether each species traces different gas.

Fitting each species separately, there is no agreement on the most likely values of the gas temperature and density. o-H_2CS, p-H_2CS, OCS and SO do not strongly favour any particular gas density but tend towards higher densities. On the other hand, SO_2 strongly constrains the density to be $n_{H2}=(3.6 \pm 0.8) \times 10^5\,cm^{-3}$ so SO_2 is clearly tracing different gas. The SO_2 densities are in the range found for CS emission from the B1 cavity (Gómez-Ruiz et al. 2015).

The difference in emitting gas becomes clear when examining the most likely gas temperature for each species. All species favour a particular temperature but there is large variation between species. SO and o-H_2CS both give low temperatures close to 16 K. OCS and SO_2 give higher temperatures of $T_{kin}=(37 \pm 2)$ and $T_{kin}=(48 \pm 5)$ K respectively. For p-H_2CS, a temperature of $T_{kin}=(60.0 \pm 10.0)$ K was found which is consistent with the temperature derived for the B1 region from CO(Lefloch et al. 2012) and CS (Gómez-Ruiz et al. 2015).

Fitting all the species with one density and temperature gave generally poorer fits for all transitions of all species. This procedure gave a temperature and density of $T_{kin} = (46 \pm 3)$ K and $n_{H2} = (3.9 \pm 0.5) \times 10^5\,cm^{-3}$. This is well in agreement with the values from SO_2 but the fits for every other species suffers. In particular, the SO fit becomes extremely poor, suggesting the SO and SO_2 emission come from very different gas.

Ultimately, it is likely that the IRAM-30M beam encompasses a large number of different gas conditions and the best fit conditions found through the RADEX modelling represent the average properties of the regions contributing the most to each species' emission. This will vary from species to species subject to the excitation properties of the detected transitions and the chemical properties of the species.

5.3.2 Column Densities and Fractional Abundances

The most robust results from the RADEX modelling were the column densities, the fitting procedure strongly constraining the column density even when one of the gas properties could not be well constrained. The most likely column densities and 1σ uncertainties are given in Table 5.1. The probability distributions from the sampling procedure are shown in Appendix C.

It is possible that both o-H_2CS and p-H_2CS trace the same gas and so RADEX fits were performed with shared a density and temperature for both species. If this assumption is made, an ortho to para ratio can be calculated and a value of 5.8±1.1 was found for H_2CS in L1157-B1. This is unrealistically high given that the statistical limit is 3. This ratio and the fact the individual fits to o-H_2CS and p-H_2CS give very different physical conditions indicates that the two species are not tracing the same gas and so can not be compared. Fitted separately, the column densities of H_2CS from the RADEX fitting are $(1.8 \pm 0.2) \times 10^{13}\,\mathrm{cm}^{-2}$ and $(3.4 \pm 0.4) \times 10^{12}\,\mathrm{cm}^{-2}$ for the ortho and para species respectively.

All detected transitions of OCS, SO and SO_2 were used for their respective RADEX fits. It was possible to strongly constrain the column density for all three data sets. Figures 5.3 and 5.4 show the RADEX outputs for the most likely values from the OCS and SO fitting, plotted as rotation diagrams with the original data. They show good agreement between the modelling and the data, though the OCS fitting favours high densities and low temperatures and so has a slightly too steep gradient.

Figure 5.5 shows the best SO_2 RADEX model, it gives good agreement with the lower E_u transitions but fails at high E_u. It is likely that the SO_2 emission arises from multiple gas components and the high E_u emission is from another, hotter gas component. This would be in agreement with SO_2 interferometry of the region (Feng et al. in prep.).

For CCS, no collisional data is available so the rotation diagram derived column density is reported. The rotation diagram shown in Figure 5.6 shows that the CCS emission is

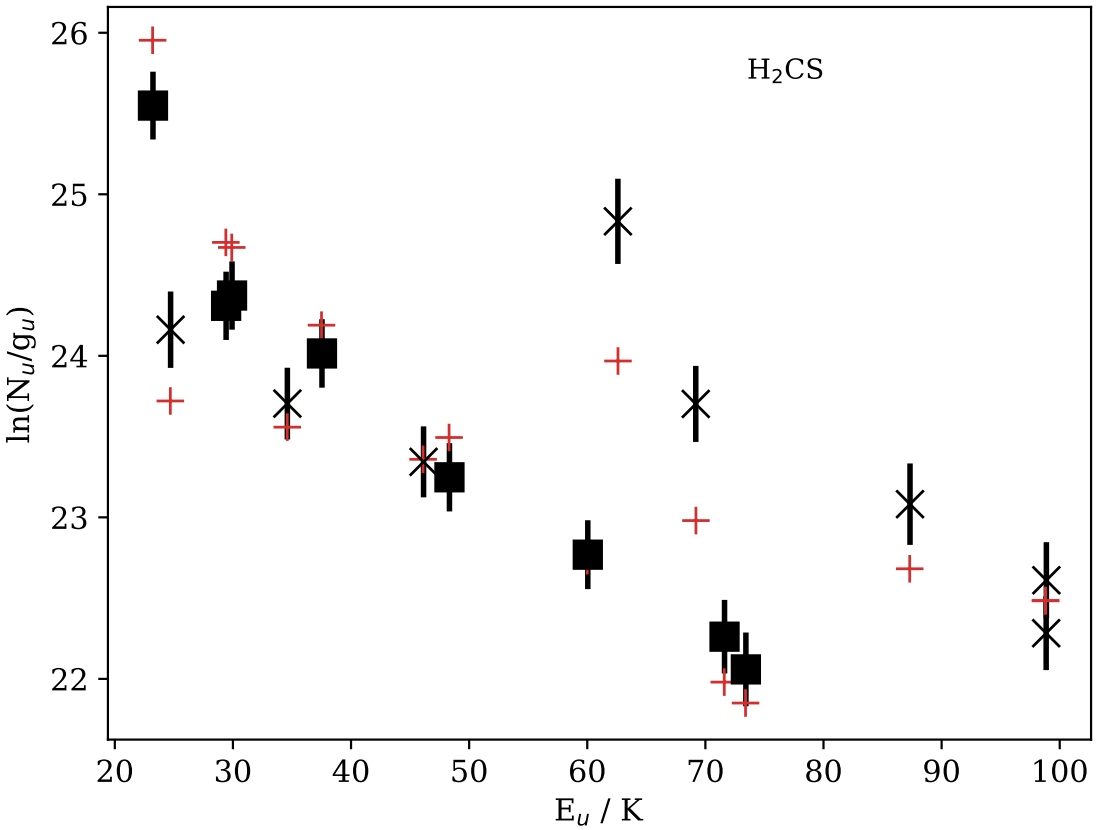

Figure 5.2: Rotation Diagram for detected H_2CS transitions with ortho transitions marked as squares and para transitions as crosses. Red points indicate the values given by the best fit RADEX model.

well fit by two components, an 8 K and a 34 K component, splitting the data at E_u=40 K. The column densities derived from these two components differ by a factor of 30.

Table 5.1 also gives the column density of ^{34}SO derived from a rotation diagram. The column density is $(8.2 \pm 3.6) \times 10^{12}\,cm^{-2}$ and this is consistent with the SO column density derived from RADEX if a $^{32}S/^{34}S$ ratio of 22 is assumed (Rosman and Taylor 1998).

5.3.3 Secondary SO Emission

The SO emission is a particularly large dataset with many high signal to noise lines, the majority of which show a secondary peak at $-12\,km\,s^{-1}$. The presence of this peak in multiple transitions implies it is SO emission, rather than contamination from another species and that it comes from a weakly emitting, more blue shifted part of the bow shock. Furthermore, secondary peaks were observed in HCO^+ by Podio et al. (2014) so this is not

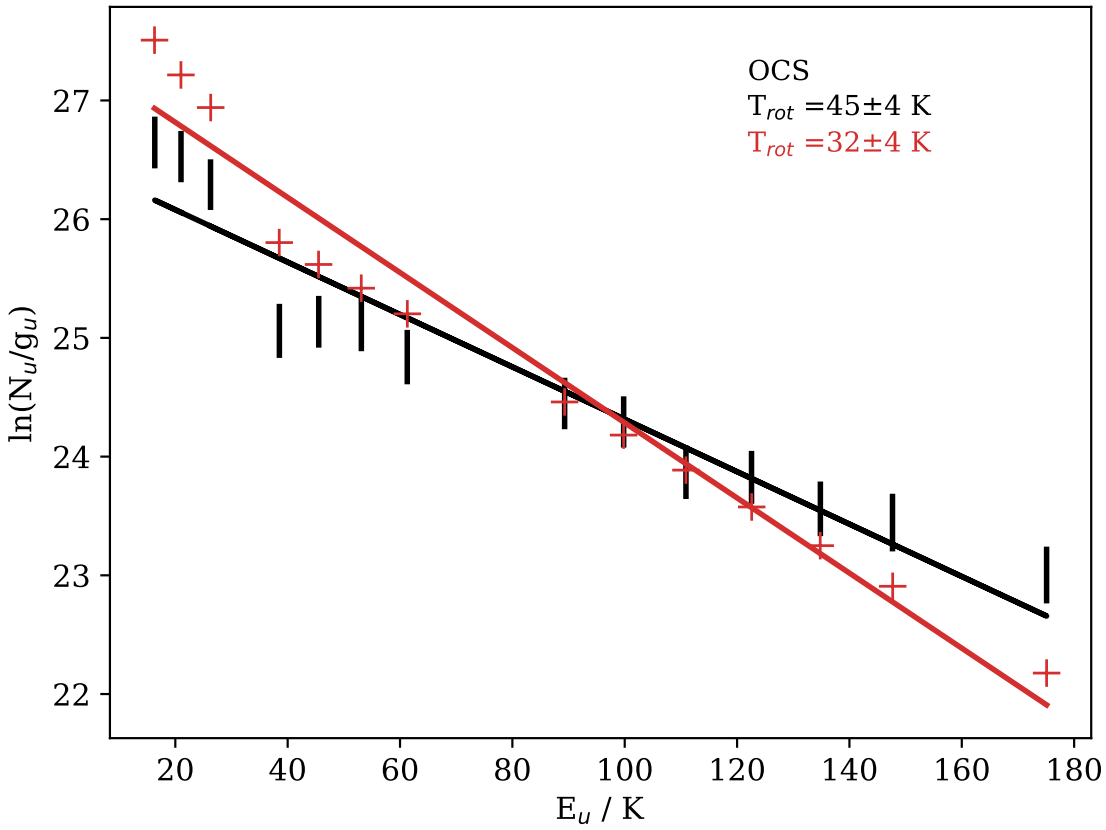

Figure 5.3: Rotation Diagram for detected OCS transitions. Red points indicate values given by the best fit RADEX emission. Linear fits have been made to each data set to infer a rotational temperature and column density.

unique to SO. In fact, Benedettini et al. (2013) showed B1 to be made up of substructures and one such "clump" B1a showed secondary high velocity emission at $-12\,\mathrm{km\,s^{-1}}$. This coincides with the peak of the secondary SO emission. In this section, the emission of the primary peak and secondary "bump" are compared to identify their sources and relative conditions.

An example of the SO line profiles can be seen in Figure 5.7. Overplotted are four transitions of SO with frequencies for which the telescope beam size would vary from 9" to 25". With the peaks normalized, it is clear the bump emission is a larger fraction of the peak emission for smaller beams. This trend is clearly visibile across all transitions of SO. This would imply that the secondary bump is closely centred on the pointed position of the telescope, as the relative emission of the bump decreases as the emission is averaged over a larger area.

Due to the frequency spacing of the SO transitions, it is hard to deconvolve the effect of the beam size from any excitation effects. However, small groups of transitions with

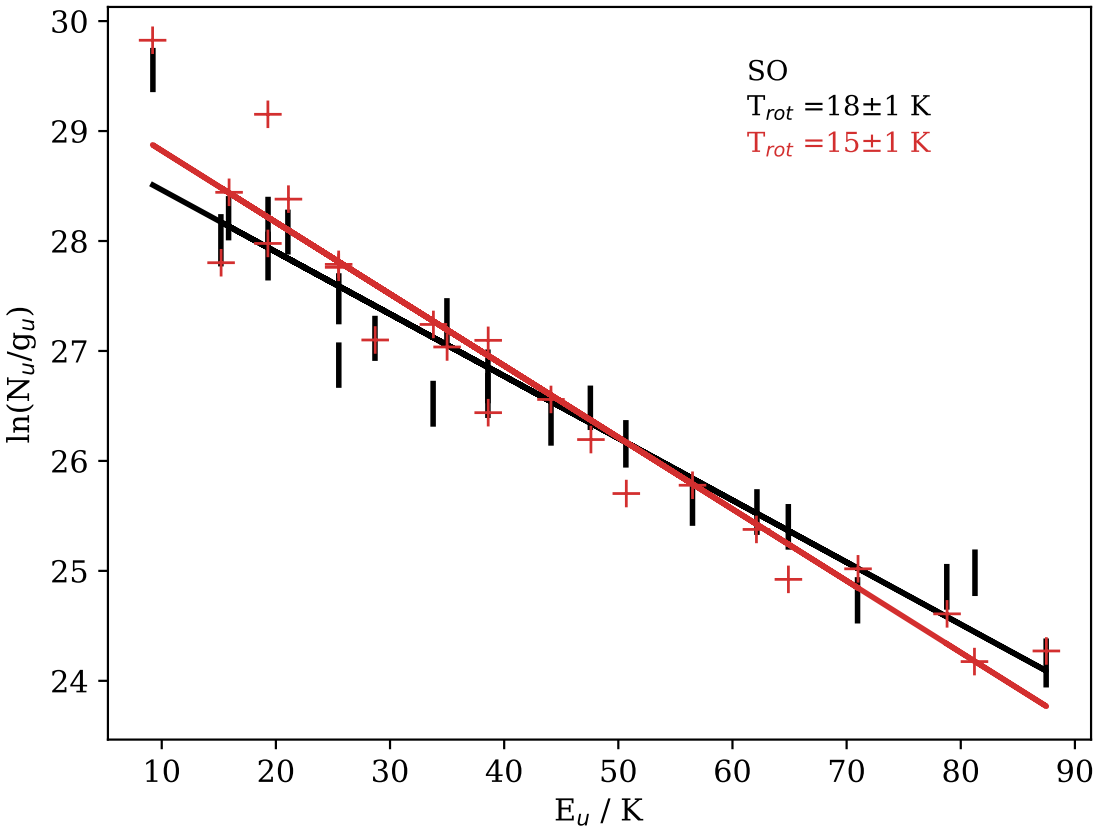

Figure 5.4: Rotation Diagram for detected SO transitions. Red points indicate values given by the best fit RADEX emission. Linear fits have been made to each data set to infer a rotational temperature and column density.

varying excitation properties and similar (within 1") beam sizes can be compared and there is some evidence that the bump to peak ratio increases for higher excitation transitions. The second panel of Figure 5.7 demonstrates this for three transitions, each with a beam size of 11" or 10". Whilst not definitively shown by the spectra, this conclusion is supported by the RADEX analysis below.

The pointed co-ordinates for the SO observations are extremely close to the B1a peak seen in CS and the bump is strongest with small beam sizes, consistent with the result that the B1a high velocity bullet is no more than 8". These points and the fact the secondary emission peaks at the same velocity as the high velocity emission associated with B1a makes it likely that the secondary SO emission originates from the high velocity bullet associated with B1a.

Velocity-intensity fits to the wing of each SO line up to $-8\,\mathrm{km\,s^{-1}}$ were made and extrapolated over the full velocity range to remove the main SO emission from spectra.

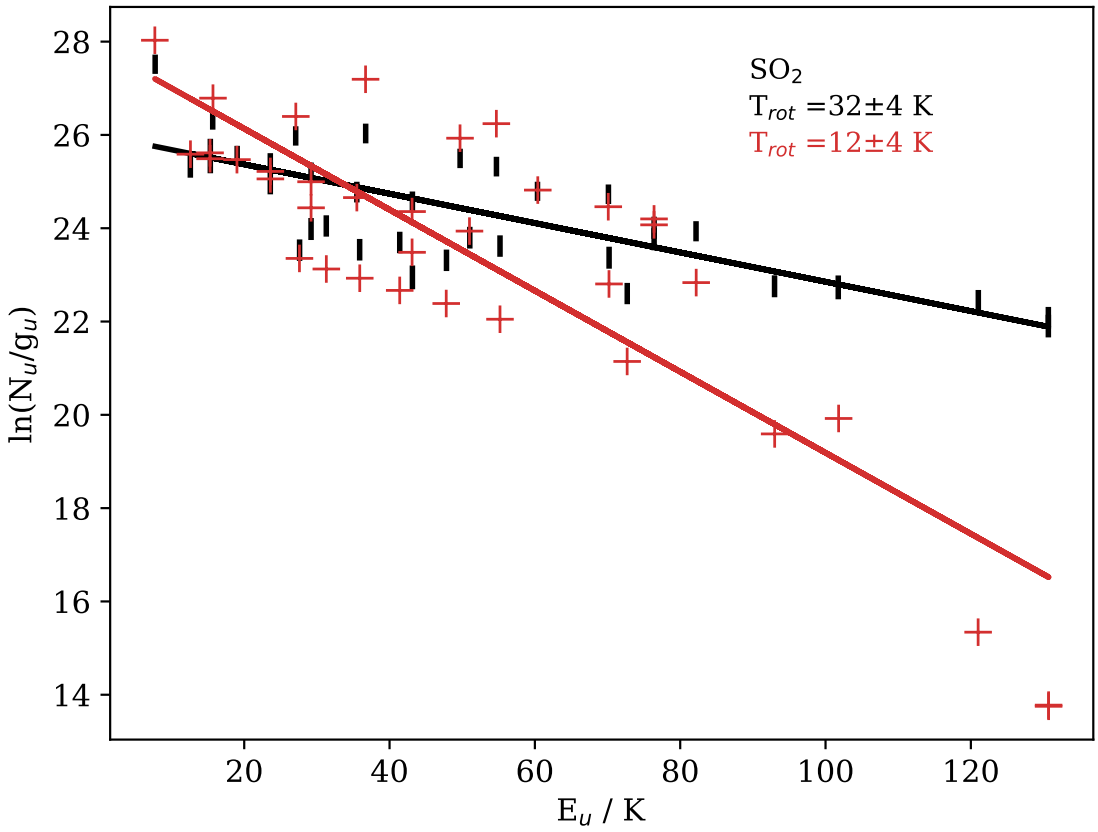

Figure 5.5: Rotation Diagram for detected SO_2 transitions. Red points indicate values given by the best fit RADEX emission. Linear fits have been made to each data set to infer a rotational temperature and column density.

The remaining spectra were then integrated between $-8\,\mathrm{km\,s^{-1}}$ and $-17\,\mathrm{km\,s^{-1}}$. This gave an estimate for the total flux in the secondary peak for each transition, which was then analysed with RADEX in the same way as the main emission. Considering the likely identification of the secondary emission as belonging to the B1a clump, a source size of 10" was assumed.

RADEX fits to this bump emission favours lower densities than found for the peak emission, though it should be noted that the density of the peak is not well constrained. For the bump, the most likely value is n_{H2}=$2.0 \times 10^6\,\mathrm{cm^{-3}}$ with a 1σ interval of $5 \times 10^5\,\mathrm{cm^{-3}}$ to $8 \times 10^6\,\mathrm{cm^{-3}}$ whereas for the peak the majority of the probability density lies above $1.0 \times 10^7\,\mathrm{cm^{-3}}$. The secondary bump also has a higher temperature than the main peak. The best fit temperature is $(45 \pm 19)\,\mathrm{K}$. The secondary SO emission has a column density of $(4.3 \pm 0.3) \times 10^{12}\,\mathrm{cm^{-2}}$, a factor of ~ 40 less than the bulk of the SO emission.

The derived properties of the secondary bump are consistent with the LVG modelling

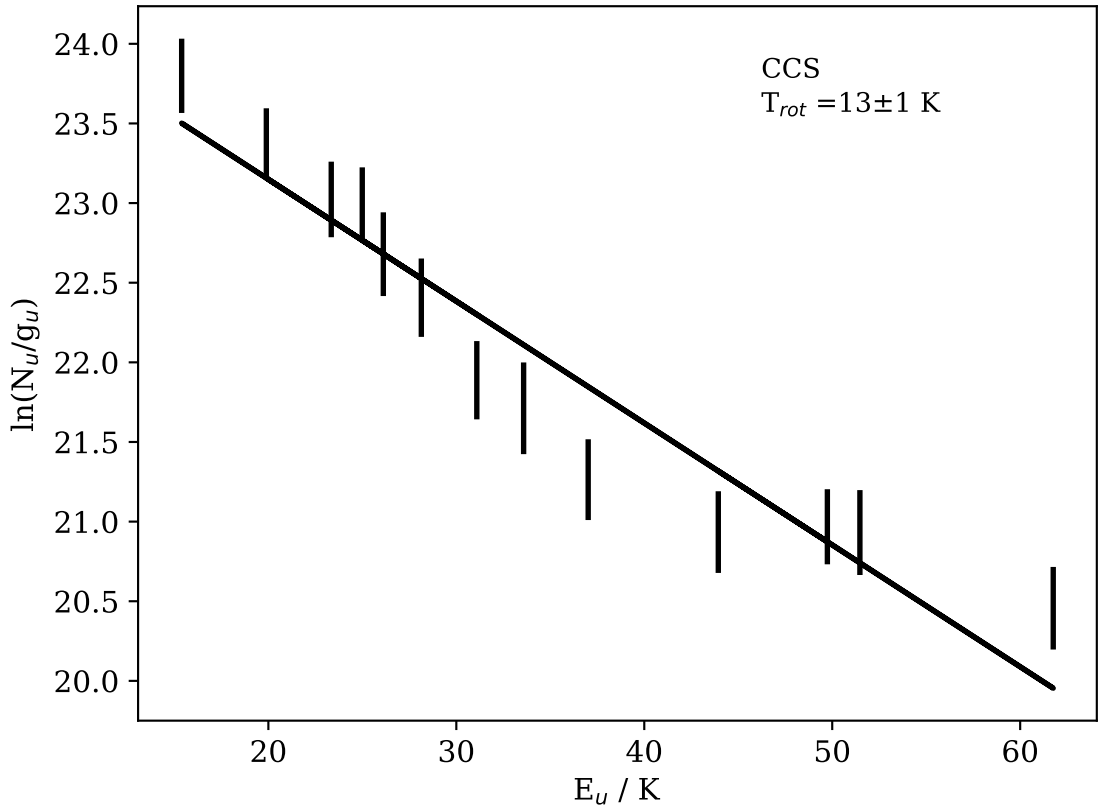

Figure 5.6: Rotation Diagram for detected CCS transitions. Two components have been fit due to clear break in gradient at E_u=40 K. The fit to the lower excitation points give a much higher CCS abundance and lower rotational temperature than the higher excitation points.

of high velocity CS emission from the B1a clump from Benedettini et al. (2013). That work similarly found a temperature varying from a few tens to a few hundred Kelvin and a density of up to $5 \times 10^5\,\mathrm{cm}^{-3}$, the χ^2 results presented in Figure 7 of that paper are similar to the probability distribution for the secondary SO emission shown in Appendix C. However, the properties derived from CS are done by fitting to two lines whereas many more lines are used for the secondary SO emission. It is therefore to be expected that the temperature is better constrained by the SO data.

5.4 The Origin of Sulfur-Bearing Species

5.4.1 Chemical Modelling

In order to understand the origin of the observed sulfur-bearing species, the work of Chapter 4 is built upon in this section. However, in the last chapter, only the form of

Table 5.1: Column density and fractional abundances for all species, tabulated with gas temperature and density fits from RADEX.

Species	N cm^{-2}	Fractional Abundance	T_{kin} K	$log(n_{H2})$ cm^{-3}
$CCS^{(1)}$	$(9.1 \pm 1.6) \times 10^{12}$	$(9.1 \pm 1.6) \times 10^{-9}$	-	-
$CCS^{(2)}$	$(2.9 \pm 1.5) \times 10^{11}$	$(2.9 \pm 1.5) \times 10^{-10}$	-	-
o-H_2CS	$(1.8 \pm 0.2) \times 10^{13}$	$(2.6 \pm 0.3) \times 10^{-8}$	15 ± 1	7.3 ± 0.6
p-H_2CS	$(3.4 \pm 0.4) \times 10^{12}$	$(3.4 \pm 0.4) \times 10^{-9}$	60 ± 10	6.75 ± 0.90
OCS	$(6.0 \pm 0.3) \times 10^{13}$	$(6.0 \pm 0.3) \times 10^{-8}$	37 ± 2	7.1 ± 0.7
SO	$(1.7 \pm 0.1) \times 10^{14}$	$(1.7 \pm 0.1) \times 10^{-7}$	16 ± 1	7.7 ± 0.3
SO Secondary	$(4.3 \pm 0.3) \times 10^{12}$	$(4.3 \pm 0.3) \times 10^{-9}$	45 ± 19	6.3 ± 0.6
^{34}SO*	$(8.2 \pm 3.6) \times 10^{12}$	$(8.2 \pm 3.6) \times 10^{-9}$	-	-
SO_2	$(9.0 \pm 0.5) \times 10^{13}$	$(9.0 \pm 0.5) \times 10^{-8}$	47 ± 5	5.6 ± 0.1
$H_2S^{(3)}$	6×10^{13}	6×10^{-8}	-	-
$CS^{(4)}$	8×10^{13}	8×10^{-8}	50 - 100	10^5-10^6
$SO^{+(5)}$	7×10^{11}	8×10^{-10}	-	-
$HCS^{+(5)}$	6×10^{11}	7×10^{-10}	80	8×10^5
$SiS^{(6)}$	2×10^{13}	2×10^{-8}	-	-

1) Derived from rotation diagram where E_u <40 K. 2) Derived from rotation diagram where E_u >40 K. 3) Holdship et al. (2016). 4) Gómez-Ruiz et al. (2016). 5) Podio et al. (2014). 6) Podio et al. (2017).

sulfur on the grains was investigated and the best fit model of Viti et al. (2011) was assumed for the physical model. In this chapter, a much larger amount of data is studied and so the properties of the shock can also be explored. The aim is to evaluate what parameters of the physical model and what grain surface abundances of sulfur-bearing species are most appropriate when the emission of many sulfur-bearing species is considered together.

The models follow the fractional abundances of chemical species through two phases. In the first, the pre-shock molecular cloud is modelled as a dimensionless parcel of gas, the chemistry is advanced through 6 Myr as the gas parcel undergoes freefall to the pre-shock density of the modelled cloud. During this freefall, gas-phase chemistry and freeze out onto the dust grains occurs along with non-thermal desorption as UV radiation and cosmic rays remove species from the dust grains. In the second phase, the density and temperature of the gas change according the C-shock parameterization of Jiménez-Serra et al. (2008) and the ice mantles are released through sputtering.

Twenty five pairs of pre-shock gas densities and shock velocities were ran in ranges $10\,km\,s^{-1}$ to $45\,km\,s^{-1}$ and $10^4\,cm^{-3}$ to $10^6\,cm^{-3}$. Note the gas density used in the models

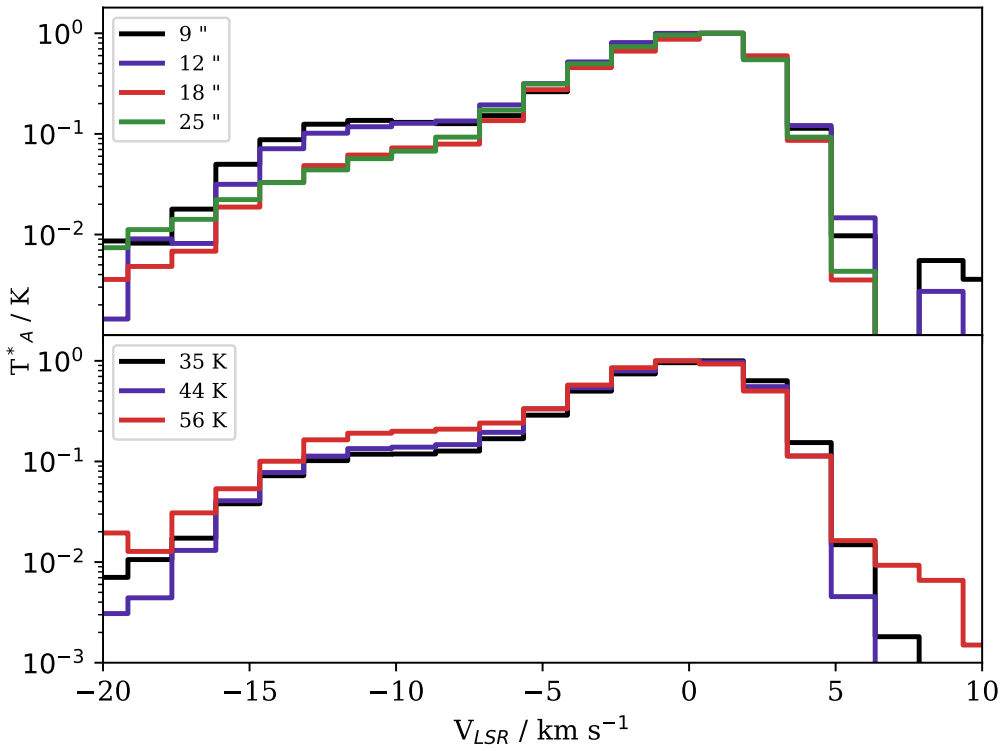

Figure 5.7: Normalized and resampled line profiles of SO where the secondary emission peak at -12.5 km s^{-1} can be seen. The upper panel shows transitions with similar excitation properties but different frequencies, to illustrate the effect of beam size. The lower panel shows the smaller effect of excitation, with three transitions of similar frequency but differing E_u plotted.

is the total number of hydrogen nuclei per cubic centimetre. Every model used solar elemental abundances from Asplund et al. (2009) and the cosmic ray ionization rate was the standard 1.3×10^{-17} s^{-1}. See Jiménez-Serra et al. (2008) for more information on the C-shock parameterization and Chapter 2 for more details on the models used here.

In order to investigate the form of sulfur on the grains, the starting abundances of certain species on the grain are varied for the second phase, following work by Woods et al. (2015). In Phase 1, each species freezes onto the grain and undergoes no further reactions, giving the total amount of each species and element on the grains. In Phase 2, the grain surface abundances of S, OCS, H_2S, H_2CS, CS and CO are altered (whilst conserving the total) to produce four different sets of grain abundances. The actual values used for each set of abundances for models with n_H=10^5 cm^{-3} are given in Table 5.3 as an example. In the first, no changes are made to the frozen abundances. In the second, all frozen S is added to H_2S and all CS to H_2CS to mimic efficient hydrogenation. For the

Table 5.2: Physical Properties of Models

Pre-shock Density (cm^{-3})	V_{shock} (km s^{-1})	t_{sat} (yr)	T_{max} (K)	Z_{diss} cm
10^4	10.0	97.6	323	3.70×10^{16}
10^4	15.0	74.7	584	5.55×10^{16}
10^4	20.0	58.6	869	7.41×10^{16}
10^4	25.0	48.3	1178	9.26×10^{16}
10^4	30.0	42.6	1510	1.11×10^{17}
10^4	35.0	40.3	1866	1.30×10^{17}
10^4	40.0	40.3	2245	1.48×10^{17}
10^4	45.0	41.3	2648	1.67×10^{17}
10^4	60.0	39.7	3999	2.22×10^{17}
10^4	65.0	33.7	4497	2.41×10^{17}
10^5	10.0	9.8	301	3.70×10^{15}
10^5	15.0	7.5	555	5.55×10^{15}
10^5	20.0	5.9	893	7.41×10^{15}
10^5	25.0	4.8	1316	9.26×10^{15}
10^5	30.0	4.3	1824	1.11×10^{16}
10^5	35.0	4.0	2416	1.30×10^{16}
10^5	40.0	4.0	3093	1.48×10^{16}
10^5	45.0	4.1	3855	1.67×10^{16}
10^6	10.0	1.0	279	3.70×10^{14}
10^6	15.0	0.8	525	5.55×10^{14}
10^6	20.0	0.6	916	7.41×10^{14}
10^6	25.0	0.5	1454	9.26×10^{14}
10^6	30.0	0.4	2137	1.11×10^{15}
10^6	35.0	0.4	2966	1.30×10^{15}
10^6	40.0	0.4	3941	1.48×10^{15}

third set of abundances, only half of the S and CS on the grains is hydrogenated and in the fourth set, half the S and CS is hydrogenated and the remaining CS and S is added to OCS, reducing the CO appropriately.

Four initial grain abundances and 25 physical models gives a grid of 100 models. The abundance of each species was compared to the fractional abundances measured from L1157-B1, using the fractional abundance of CO from the model to convert from the column density rather than assuming $X_{CO} = 10^{-4}$. Particular attention was paid to the abundance at 1000 years in the model, which corresponds to the dynamical age of L1157-B1 (Podio et al. 2016). In this way, the shock properties of L1157-B1 are explored along with the possible forms of sulfur on the dust grains.

Table 5.3: Initial Grain Abundances for Phase 2. Example values used for models with n_H=10^5 cm^{-3}.

Set	#S	#OCS	#H_2S	#H_2CS	#CS
1	1.31×10^{-5}	1.36×10^{-9}	1.44×10^{-9}	1.01×10^{-9}	8.90×10^{-9}
2	-	1.36×10^{-9}	1.31×10^{-5}	9.91×10^{-9}	-
3	6.54×10^{-6}	1.36×10^{-9}	6.54×10^{-6}	5.46×10^{-9}	4.45×10^{-9}
4	-	6.54×10^{-6}	6.54×10^{-6}	5.46×10^{-9}	4.45×10^{-9}

5.4.2 Model Results

The "Standard" Model

Previous modelling work on L1157-B1 has shown many species can be fit with the same model, these include: H_2O and NH_3 (Viti et al. 2011); PN and PO (Lefloch et al. 2016); HCN and DCN (Busquet et al. 2017); and NO (Codella et al., submitted). The behaviour of each of these molecules is well reproduced by the model described above with a shock speed of 40 km s^{-1} moving through a gas with pre-shock density n_H=10^5 cm^{-3}. Therefore, it is interesting to examine how successful the same model is in describing the species presented in this work.

Figure 5.8 shows the chemical abundances of CCS, SO and SO_2 for that model along with the measured of abundance of each species. These three species are well described by the model, though only the lower abundance, higher excitation CCS component is matched. SO and SO_2 are initially low in abundance but increase with time until reaching constant abundances remarkably similar to the observed abundance once the shock reaches the dissipation length. CCS reaches the observed abundance immediately in the shock and then remains at a model abundance consistent with the observations for longer than the age of L1157-B1. It is therefore possible that these species are enhanced in the shock and they are now being observed in the cool, post-shock gas. In this particular model, none of these species is affected by the grain abundances used and so cannot be used to constrain the form of sulfur on the grains.

Figure 5.9 shows the effect of changing the shock variables from the "standard" model. The abundaces of SO and SO_2 can only be reproduced by the standard model or an extremely high density model. However, the very high pre-shock density model predicts large H_2CS abundances and the density is higher even than the post-shock densities derived from the RADEX fits.

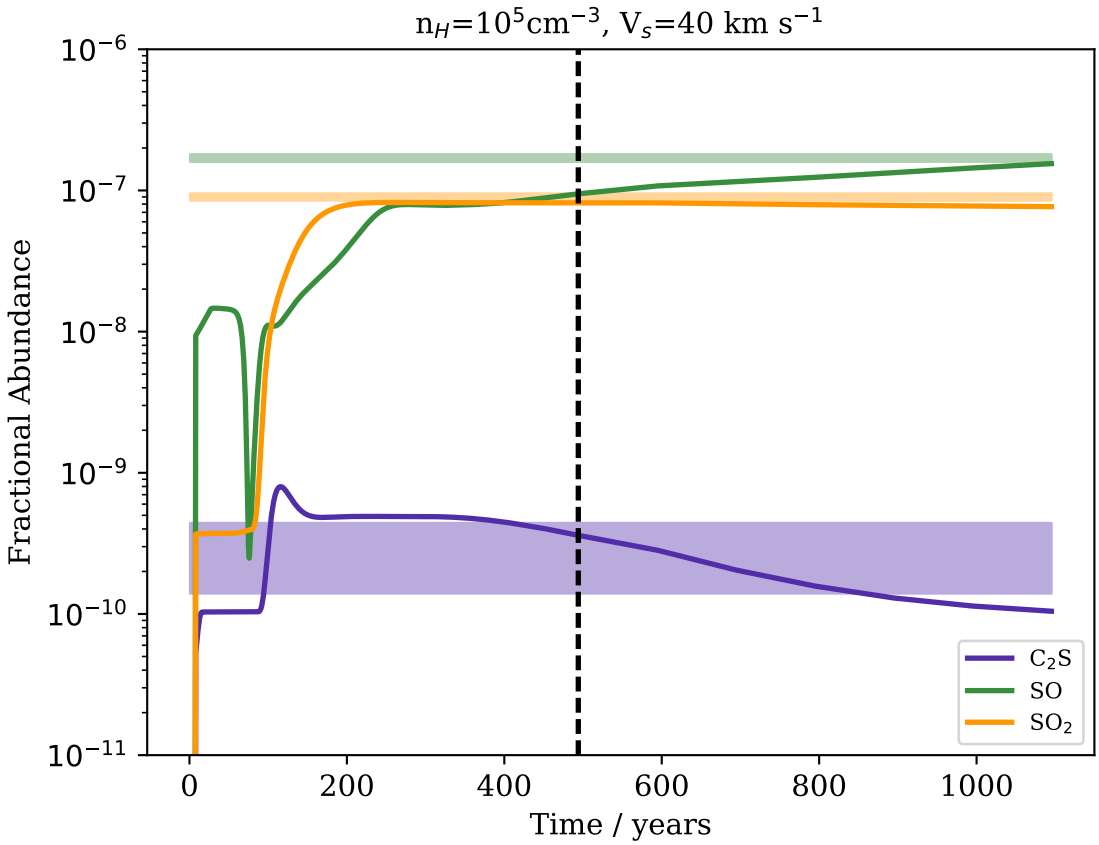

Figure 5.8: Results of a shock model with model predicted abundances as a function of time with 1σ intervals of observed abundances as faded horizontal bands. Displayed species are well fit by the model, particularly at later times. The dashed vertical line indicates the time at which the dissipation length is reached and the gas is decelerating.Results of a shock model with model predicted abundances as a function of time with 1σ intervals of observed abundances as faded horizontal bands. Displayed species are well fit by the model, particularly at later times.

Other Species

Low E_u CCS: Both the high velocity shock model and the lower velocity model shown in Figure 5.10 predict CCS abundances that agree with the value derived from the higher excitation transitions. In both models, CCS is released from the dust grains and then is kept at approximately constant abundance by its gas-phase formation and destruction routes. The primary formation route is a reaction between C_2 and OCS which is less efficient in the fast shock due to the low OCS abundance. As a result, the CCS abundance starts to fall towards the end of the fast shock model.

No model could well reproduce the lower excitation CCS abundance whilst producing feasible abundances for any other molecule. The only models that matched the higher CCS

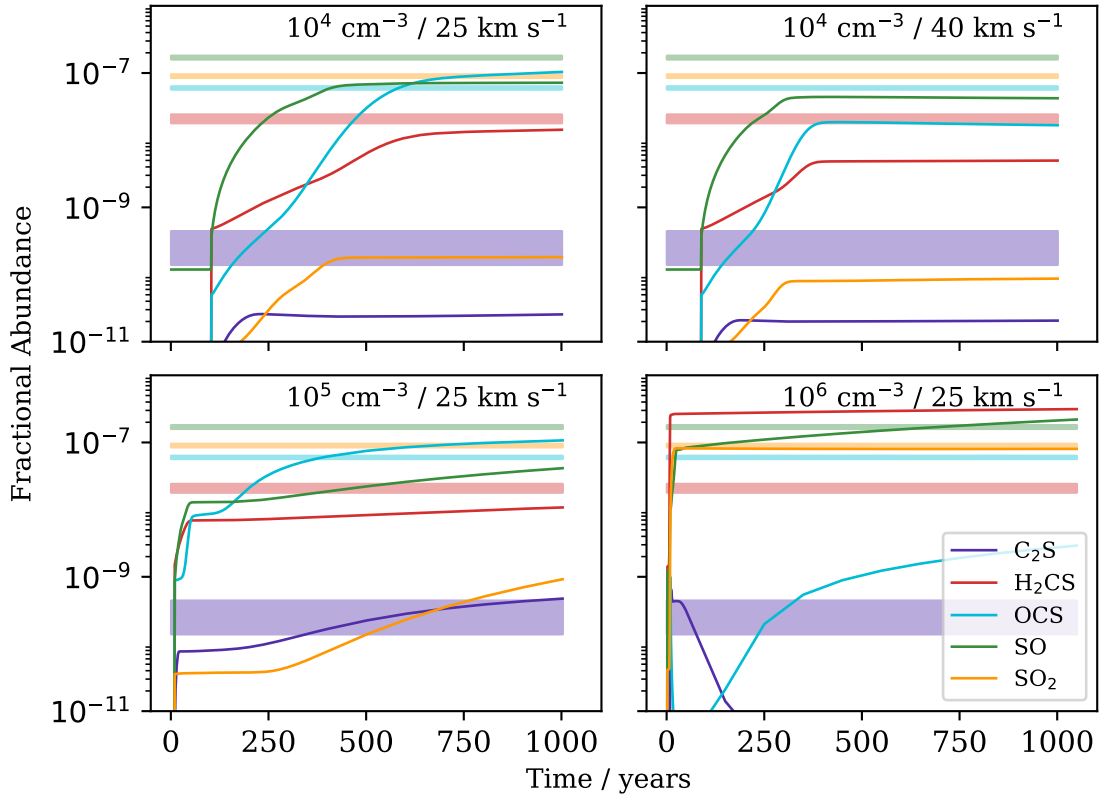

Figure 5.9: Results of various shock models showing the effects of changing different shock variables. The top left panel is a low velocity and low density model and the top right is a low density but high velocity model. In the lower row, the left is a higher density model but at a lower velocity than the "standard" model and the right panel is a very high density model with a low velocity.

abundance of the low excitation transitions were low velocity models at n_H=10^5 cm^{-3} if the initial grain abundances were taken from set 4, where half the sulfur on the grain is in OCS. However, these models overpredict the OCS abundance by two orders of magnitude and so are disfavoured.

The inability of the models to reproduce the higher CCS abundance could be a result of an incomplete network or could imply the CCS in L1157-B1 is not produced in a simple C-shock. In order to check the network, the models were rerun with an expanded gas-phase network. Adding larger sulfur-bearing species to the network made new reactions involving CCS available from the UMIST database. Due to their low abundances, this did not significantly alter the results and lead to the conclusion that the gas-phase network for CCS is sufficient. This gives two possibilities, either CCS is formed efficiently on the grains which would not be accounted for in UCLCHEM or CCS is not formed in C-type shocks and another process must be producing the CCS in L1157-B1.

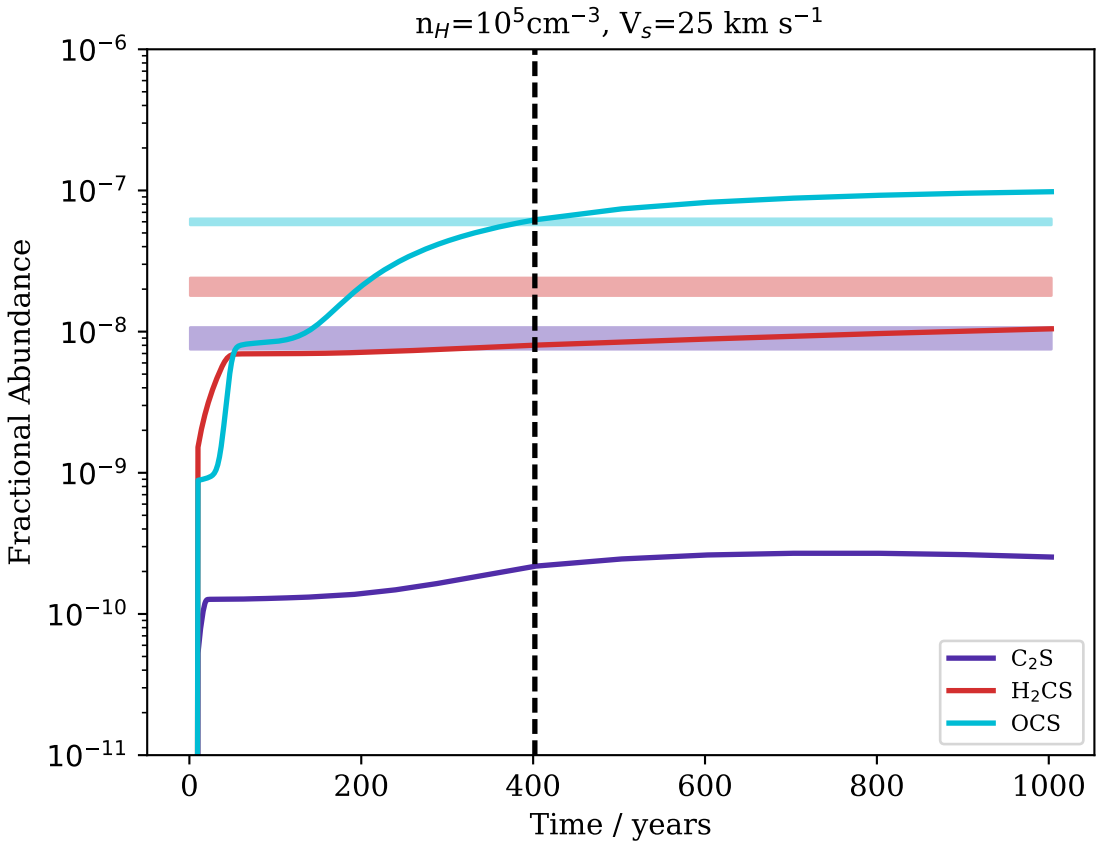

Figure 5.10: Results of a shock model with model predicted abundances as a function of time with 1σ intervals of observed abundances as faded horizontal bands. Displayed species are well fit by the model, particularly at later times. The dashed vertical line indicates the time at which the dissipation length is reached and the gas is decelerating.

H_2CS: The observed H_2CS emission is difficult to explain with the models. The best fit model from Viti et al. (2011) predicts H_2CS abundances that are an order of magnitude too high. Further, whilst other species are destroyed in the hottest, fastest part of the shock, H_2CS is not destroyed in the model and so should show a terminal velocity more similar to that which has been observed for other shock-tracing molecules in the region. The fact that this is not seen may point to a missing destruction route for H_2CS in fast shocks or simply that the model is too simple to describe H_2CS. If H_2CS is in fact destroyed in high velocity shocks, it is worth noting lower velocity models at n_H=10^5 cm^{-3} can also reproduce the H_2CS abundance and are a likely source of the observed H_2CS.

OCS: Abundance set 4, in which half the frozen sulfur is assumed to be in OCS over-predicts the OCS abundance by two orders of magnitude. OCS is also significantly under-predicted by models in which all sulfur is hydrogenated and so favours models where at least half of the sulfur on the grains is in atomic form. The fundamental result of the

comparison between the models and the observed OCS abundance is therefore that OCS is unlikely to be a major carrier of sulfur on the grains.

Unlike H_2CS, fast shocks in gas at n_H=$10^5\,cm^{-3}$ raise the gas temperature to a level that destroys the majority of the OCS and at no point in the high velocity models does OCS reach an abundance close to the observed value. Therefore, unlike H_2CS, there is no contradiction between the apparent presence of high velocity shocks in the region and the low terminal velocity of OCS. Slower shocks at around $10\,km\,s^{-1}$ have OCS abundances close to the observed value. It is possible that OCS is not observed in the main, fast shocks of B1 as it is destroyed but reaches the observed abundances in slower shocks..

Sulfur on the Grains

Generally, the inability of any single model to well predict the behaviour of all species demonstrates the ranges of gas conditions they trace. However, there are promising conclusions. All species but particularly OCS and H_2CS, favour abundance sets 1 and 3 when numerically comparing the modelled average abundance through the shock to the abundances derived from observations. That is, from these observations and the models, it is likely that at least half of the sulfur freezing onto the grains is in atomic form or is converted to atomic sulfur as it is released. The idea of a refractory sulfur residue on the grains has been proposed previously (Woods et al. 2015) and this is most consistent with the results presented here. Certainly, the release of OCS and H_2CS from the grains leads to large overpredictions of their abundance and so they are unlikely to be major sulfur carriers on grain surfaces.

Figure 5.11 demonstrates this for the low velocity model. It can be seen in the lower right plot, that the OCS abundance in the model using Set 4 is orders of magntiude higher than observed. A similar effect is also seen for H_2S in Set 2 models (see Chapter 4) where most sulfur is hydrogenated. However, for the molecules described by the low velocity model, the main effect of Set 2 is locking CS into H_2CS and lowering the OCS abundance in the shock. Typically it is hard to distinguish Set 1 and Set 3, Set 1 predicts abundances closer to the observed values over a wider range of models but the difference is small and it is not possible to use these models to favour one. A key prediction of these models is that the majority of sulfur is in the form of gas-phase atomic sulfur after 1000 years, this is consistent with observations of sulfur in shocks associated with young stellar objects by Anderson et al. (2013). In that work, the average atomic sulfur abundance accounted

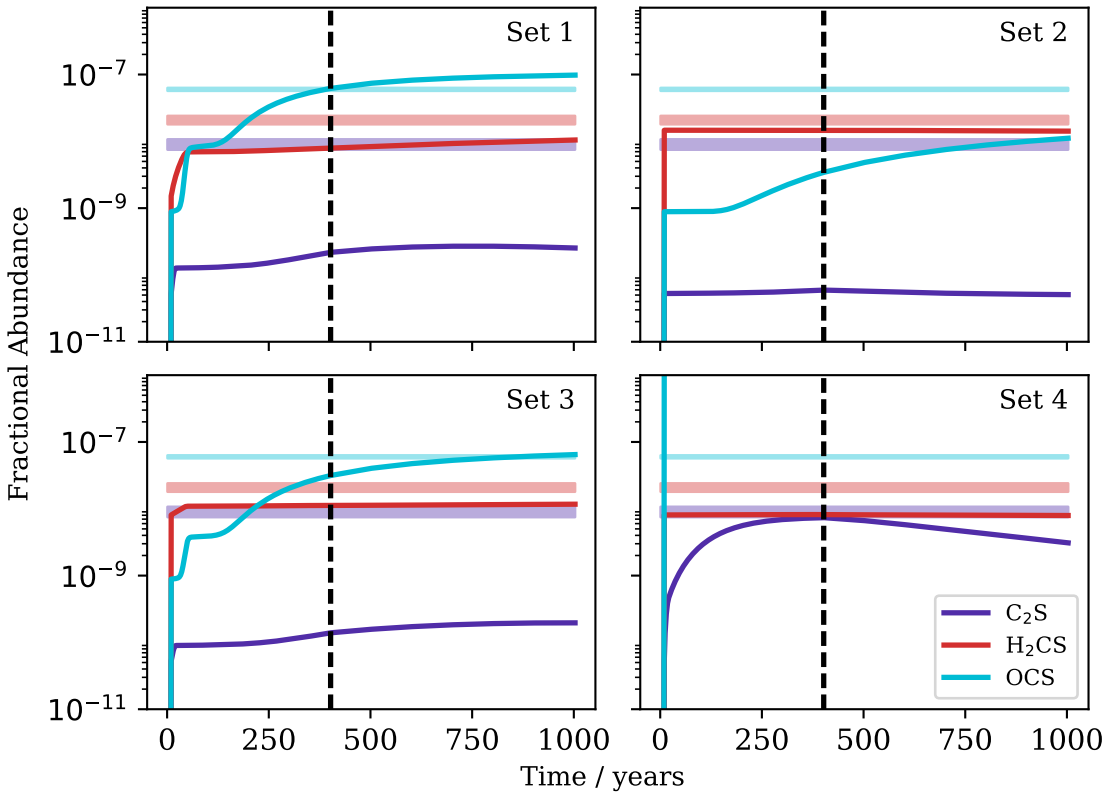

Figure 5.11: An example of how the change in grain surface abundances affects the models. The best low velocity model is plotted for all four sets of grain surface abundances. In the lower right, an example of the general effect of assuming equal amounts of OCS and H_2S can be seen. The OCS abundance reaches values orders of magnitude higher than observed.

for 10% of cosmic sulfur but this was subject to large uncertainties. In some sources, the atomic sulfur abundance could dominate the sulfur budget particularly at temperatures between 50 and 100 K.

Further, the over abundance of OCS cannot be solved by depleting the sulfur abundance in the model from the cosmic value. For H_2CS, a reduction in the cosmic value by a factor of 10 reduces the H_2CS abundance in the "standard" model to a level that fits observations. However, as a result of the reduced sulfur abundance, the modelled abundance of SO, SO_2 and CCS fall well below the observational values. Therefore, though no sulfur-bearing species that is close to the cosmic sulfur abundance is observed, the species that are reported are best fit in the shock model using the solar sulfur abundance (X_S=1.318×10^{-5}) as the initial elemental sulfur abundance.

5.5 Conclusion

Observations of CCS, H_2CS, OCS, SO and SO_2 towards L1157-B1 have been presented. Column densities have been calculated for each species using RADEX, although not every species strongly constrains the gas temperature and density of the emitting region. For those species that do constrain the density and temperature, the variation in these gas properties hint at a wide variety of conditions within the same IRAM-30m beam.

This is further evident when analysing the SO spectra, which show secondary emission at higher velocities than the main peak. The peak velocity of this secondary emission ($-12\,\mathrm{km\,s^{-1}}$), the RADEX derived properties and increasing brightness with smaller beams indicate that this emission comes from the "high speed bullet" associated with the B1a clump (Benedettini et al. 2013).

Chemical shock modelling has been used to further analyse the data, based on fractional abundances derived from RADEX. Since no single model fits all five species, it is likely that many different shock conditions are observed together. SO and SO_2 are well fit by the best fit model for H_2S taken from H16 whereas low velocity shocks can explain OCS as well as H_2CS. The abundance derived from high excitation CCS transitions can be fit by either shock model. For every species, models in which the majority of sulfur is assumed to be in atomic form are favoured. This is consistent with the result for H_2S found by Holdship et al. (2016).

Constraining the abundances of sulfur-bearing species on the grains is important because both the chemistry and the abundances of many species on the grain surface are poorly understood (See Section 1.3). Constraining the abundances of species on the grains by observing regions where the ices have been disrupted will allow chemical models to be improved as surface reaction networks can be modified to reproduce known abundances. From the work presented in this chapter, it is fair to suggest that chemical models should be able to produce results where a large fraction of the total sulfur budget is in the form of atomic sulfur.

The higher CCS abundance derived from the low E_u transitions is not well described by the models. Given that the gas-phase network is quite complete and the difference between observations and the models is often orders of magnitude, it may be that there are missing surfaces reactions leading to CCS. Alternatively, this emission may be dominated by gas not associated with the shock. Ideally, interferometric observations of CCS in

L1157-B1 could be made to give a clearer picture of the emitting gas and allow for more detailed modelling of the chemistry. Ultimately, a stronger understanding of the amount of each sulfur-bearing species present in the ice mantles is vital to correctly interpreting observations such as those presented here.

This page was intentionally left blank

Chapter 6

Concluding Remarks and Further Work

In this thesis, a chemical model has been developed and utilized in understanding two distinct processes related to star formation. Simple physical modelling has been to used to make predictions relevant for observers and contrariwise observations have been used to constrain the models.

In Chapter 2, the chemical model UCLCHEM was developed for the work that followed and for public release. The core ideas and processes considered in chemical models were discussed and a possible use for the code was presented. Molecular tracers of shocks, particularly those whose chemical behaviour may be as rich a source of information as directly interpreting radiation from species like CO and H_2 were investigated. The main result is Figure 2.5, a Carroll diagram giving the expected behaviour of different molecules over varying shock speeds and gas densities.

The release of a public code is a contribution to the community that requires either a clearly define set of capabilities and limits of the model and a simple user interface or an active group of core users and maintainers. Whilst the latter is fortunately the case for UCLCHEM, future work should focus on comprehensive and concise documentation alongside set releases.

The use of predicted chemical abundances to suggest tracers for shocks ignores the complicated radiative transfer process that may have a large effect on what is observable

and what is particularly bright. Extending the model with a radiative transfer program would give a more realistic view of what would be observed for each shock model. It may also bring to light differences in line profiles between species or excitation levels which would be another source of information.

In Chapter 3, UCLCHEM was again employed to predict molecular tracers. However, the considered astrophysical objects were bound prestellar cores. The focus of the chapter was on brown dwarf cores, as their formation is the least understood and offered the chance to truly test the star formation model that was considered. The cores were assumed to form in low velocity shocks that increase the gas density without sputtering the grains. Plots of commonly observed molecular species were presented, with predicted emission from RADEX and these species were tabulated according to their observability in cores of different masses. In addition to these general conclusions, it was suggested that the model would be best utilized in direct comparison to observations.

As of the writing of this thesis, very few observations of proto-brown dwarfs have been reported and possible pre-brown dwarfs are even fewer in number. The ideal next step for the work in Chapter 3 is the detailed modelling of an observed pre-brown dwarf core. In the final sections of Chapter 3, the results of the model are compared to the chemistry obtained by post-processing an MHD model. It seems that the initial density increase is reasonable in the model but the collapse that follows is not. Therefore, before comparing to observations, a model where the post-shock collapse is improved would be useful. The current public release of UCLCHEM includes parameterizations for the collapse of a Bonnor-Ebert sphere and this is likely to be an improvement for the brown dwarf model. In Chapter 4, observations of the L1157-B1 bowshock along a protostellar outflow in H_2S were presented and analysed. Though unobserved in the ices, chemical models predict H_2S to be abundant on the ice mantles and so it is reasonable to expect H_2S to be enhanced in a shocked region. The abundance of H_2S in the gas was estimated from rotation diagrams and RADEX, assuming homogeneous emitting gas in the telescope beam. A deuteration fraction was also calculated from isotopologue detections. Finally, a previously successful chemical model of the region was studied and it was found that the model well described the H_2S emission if most sulfur on the ice mantles is in atomic form rather than in H_2S.

In Chapter 5, the work of the previous chapter was greatly expanded on. Observations of CCS, H_2CS, OCS, SO and SO_2 were presented and analysed comprehensively. It was

found that these sulfur bearing molecules do not follow velocity distributions that fit more typical gas tracers such as CO. It was also shown that RADEX fits to the emission of each molecule were most consistent with widely varying emitting gas properties. The modelling work of the previous chapter was also expanded upon, varying the parameters of the shock model as well as the contents of the ice mantles of the pre-shock gas. It was again concluded that atomic sulfur was the most likely form of sulfur in the ices.

There are many uncertainties in the chapters relating to L1157-B1, not the least of which is the low spatial resolution. It is clear from the variation in best fit gas properties for each species and from observations of molecules such as H_2O (Busquet et al. 2014) and CO (Lefloch et al. 2012) that there are multiple different gas components in the telescope beam. Interferometry of the region is required to improve the chemical picture and this is being undertaken as part of the SOLIS survey programme (Ceccarelli et al., in prep.). Beyond this, it is important to find out whether the chemistry observed in L1157-B1 is typical of protostellar outflows. In order to investigate this, an observing proposal was submitted to the IRAM-30m telescope and accepted. Observations were taken of eight shocked regions in protostellar outflows, with lines detected in H_2CS, OCS, SO and SO_2 and likely other species. If chemical pictures can be built up for these regions, it will be possible to discover whether ices across similar regions have consistent abundances.

Appendix A

Detected Lines

The spectra used for the work in Chapter 5 are shown in Figures A.1 to A.17 labelled with their frequency, upper state energy and the IRAM-30m beam size at that frequency. Spectra are organized by species and intensity.

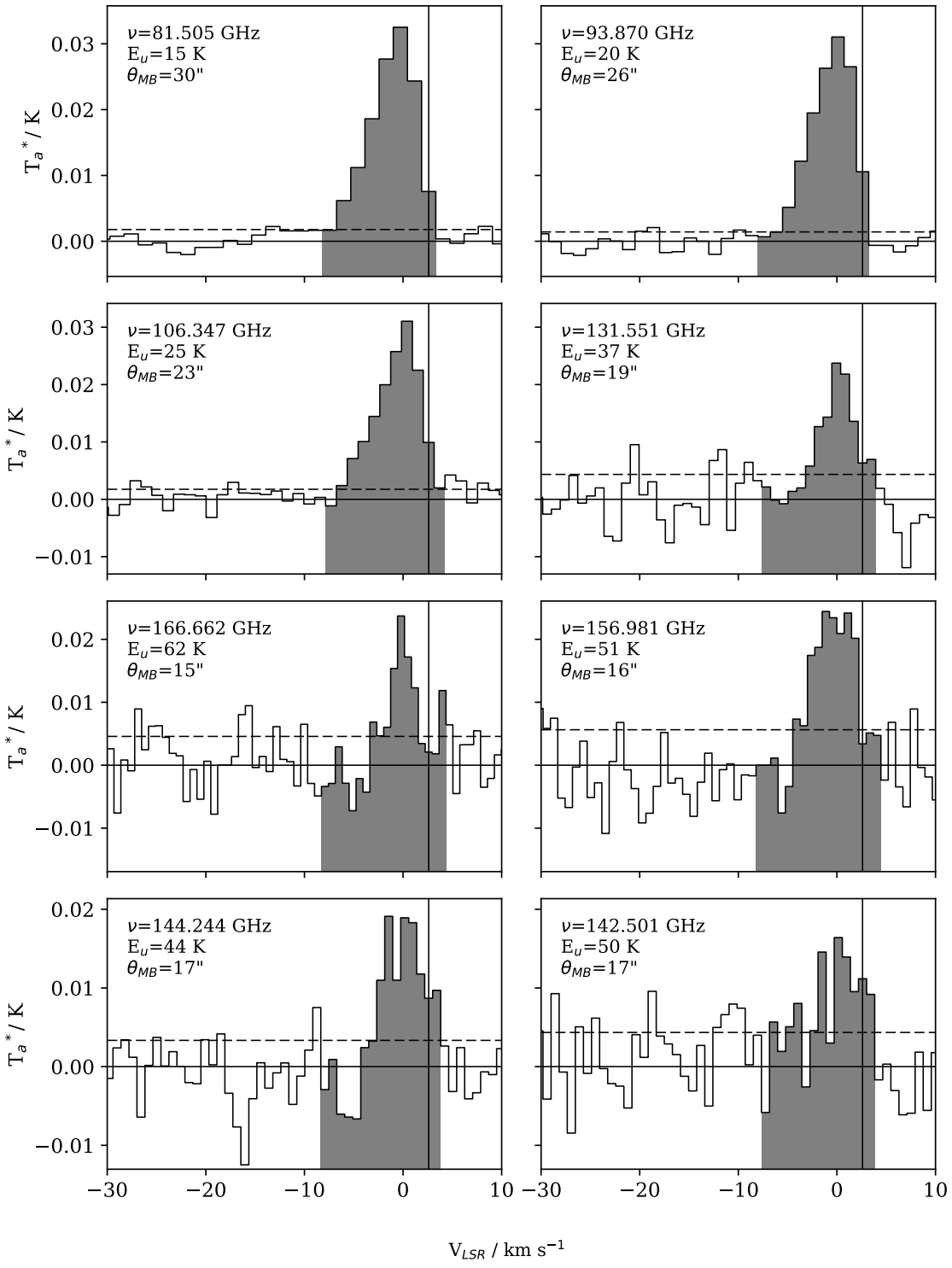

Figure A.1: Detected CCS lines. Rows share Y-axis values which are given in antenna temperature. The vertical black line indicates the location of the local standard of rest velocity $-2.6\,\mathrm{km\,s^{-1}}$. The horizontal dashed line shows the 1σ level for that spectrum, and the part of the spectrum plotted in black is the section integrated for use in this work.

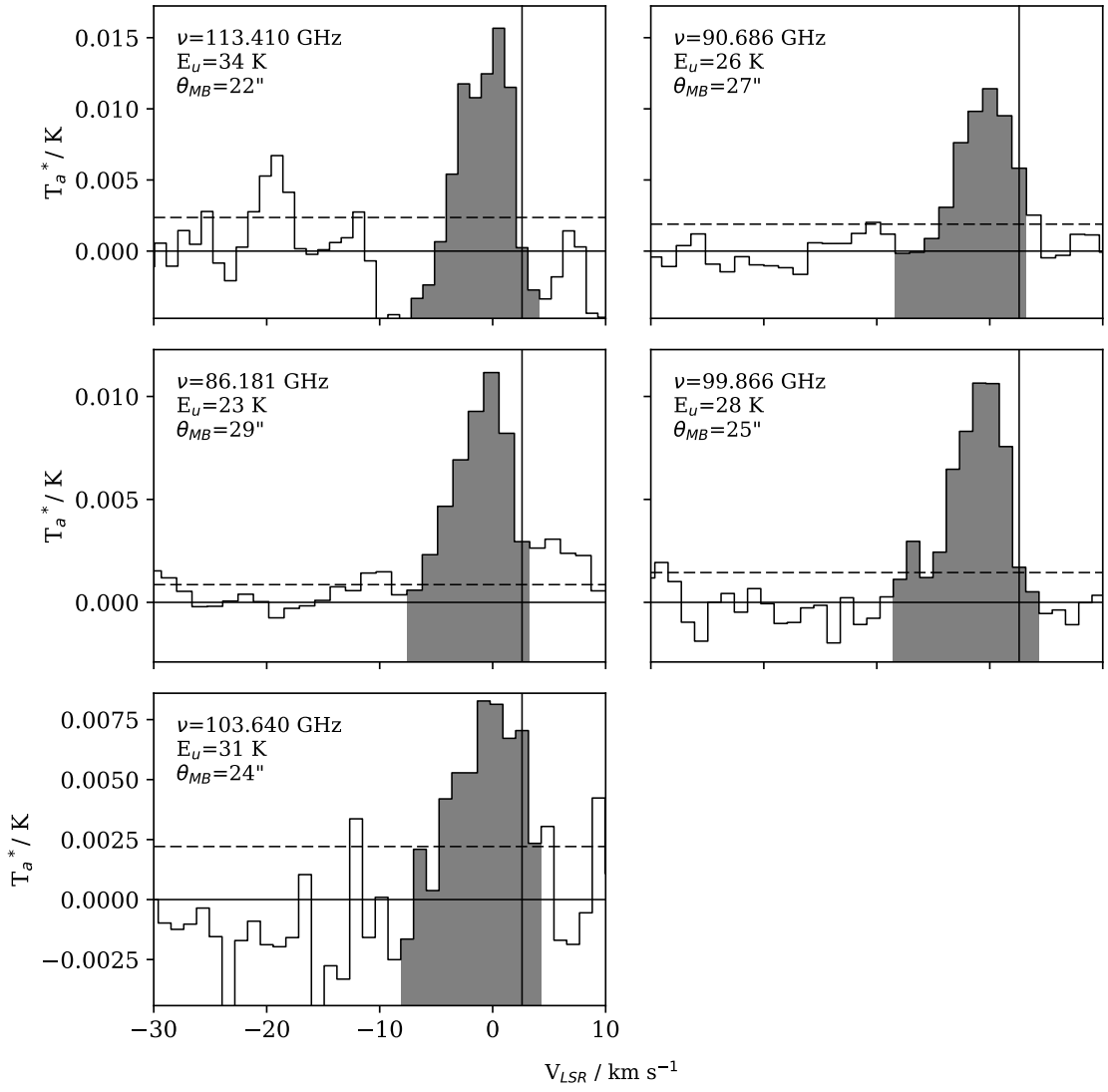

Figure A.2: Detected CCS lines cont.

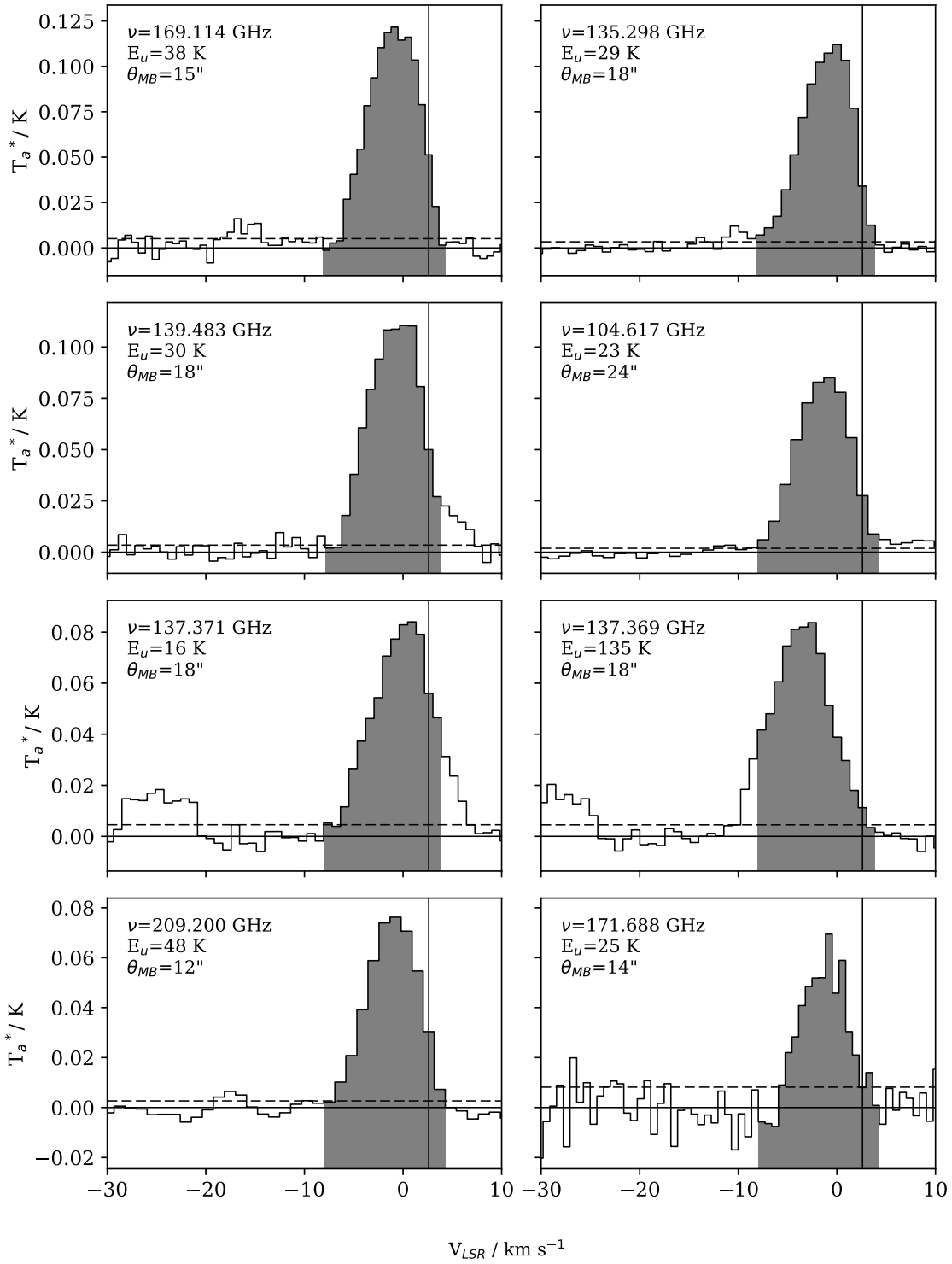

Figure A.3: Detected H_2CS lines. Rows share Y-axis values which are given in antenna temperature. The vertical black line indicates the location of the local standard of rest velocity $-2.6\,\mathrm{km\,s^{-1}}$. The horizontal dashed line shows the 1σ level for that spectrum, and the part of the spectrum plotted in black is the section integrated for use in this work. Some H_2CS lines are blended combinations of slightly offset transitions (eg. 137.369 GHz line), resulting in strange line profiles. These are not included in the main analysis due to the the difficulty and assumptions inherent in separating the flux.

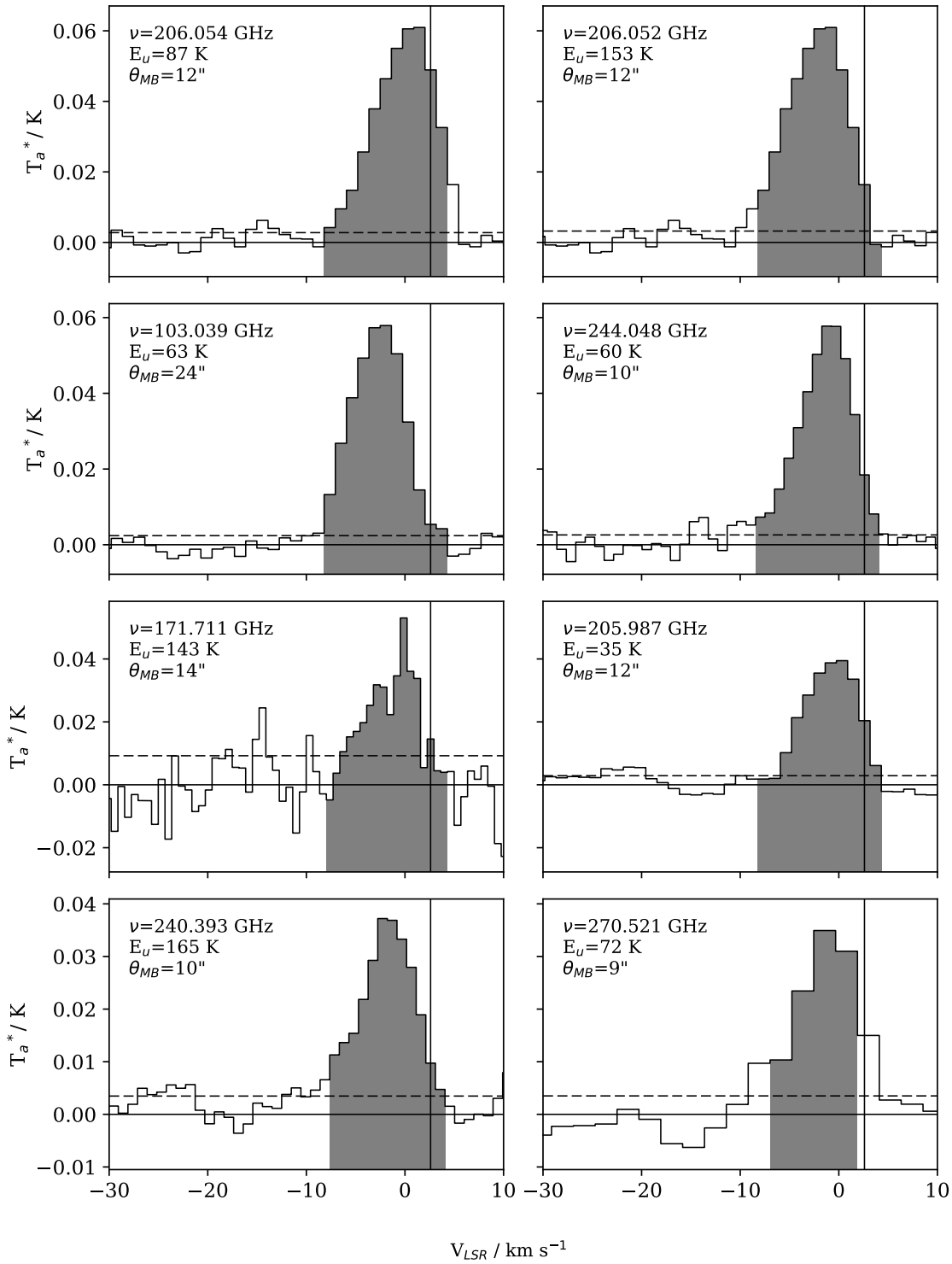

Figure A.4: Detected H_2CS lines cont.

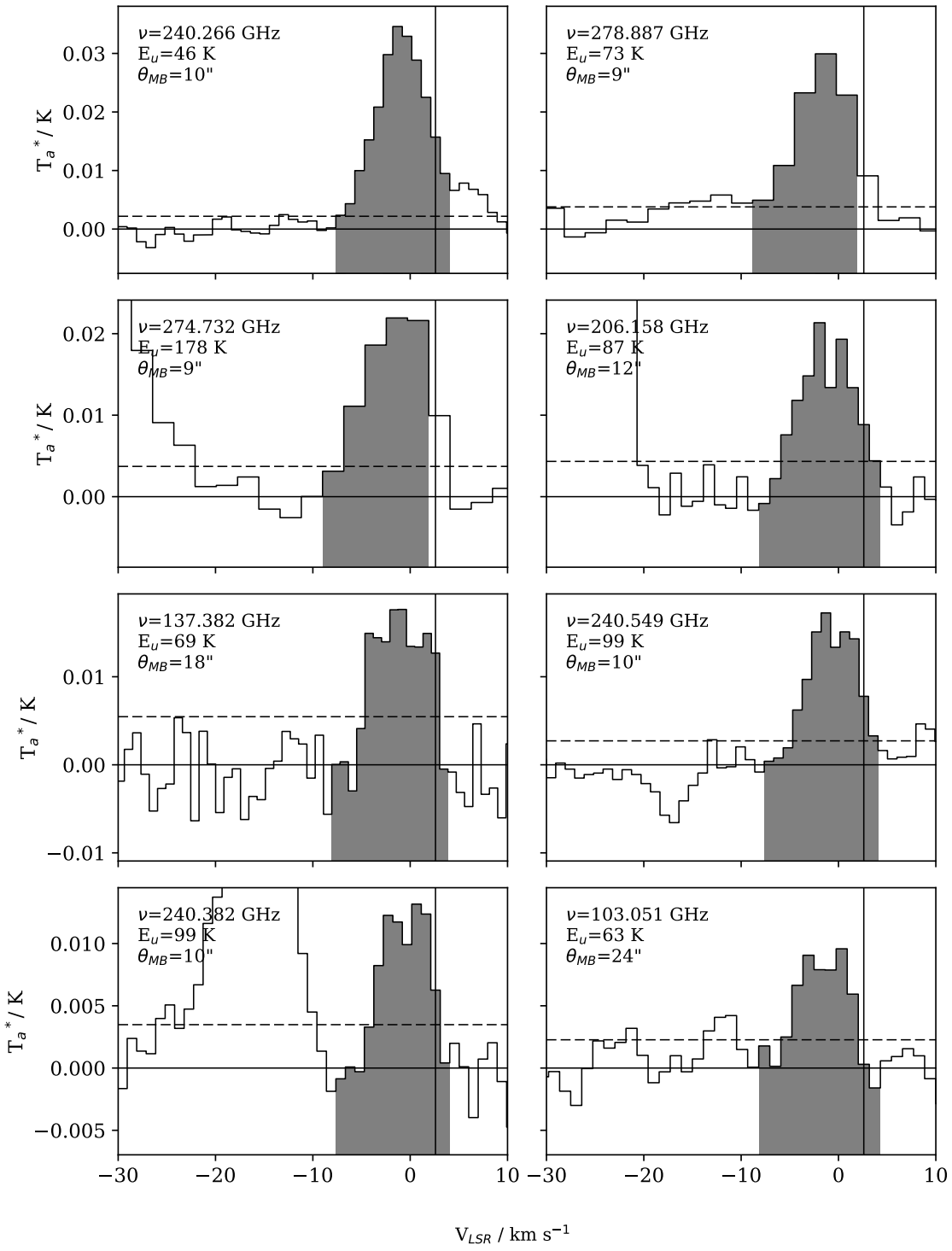

Figure A.5: Detected H_2CS lines cont.

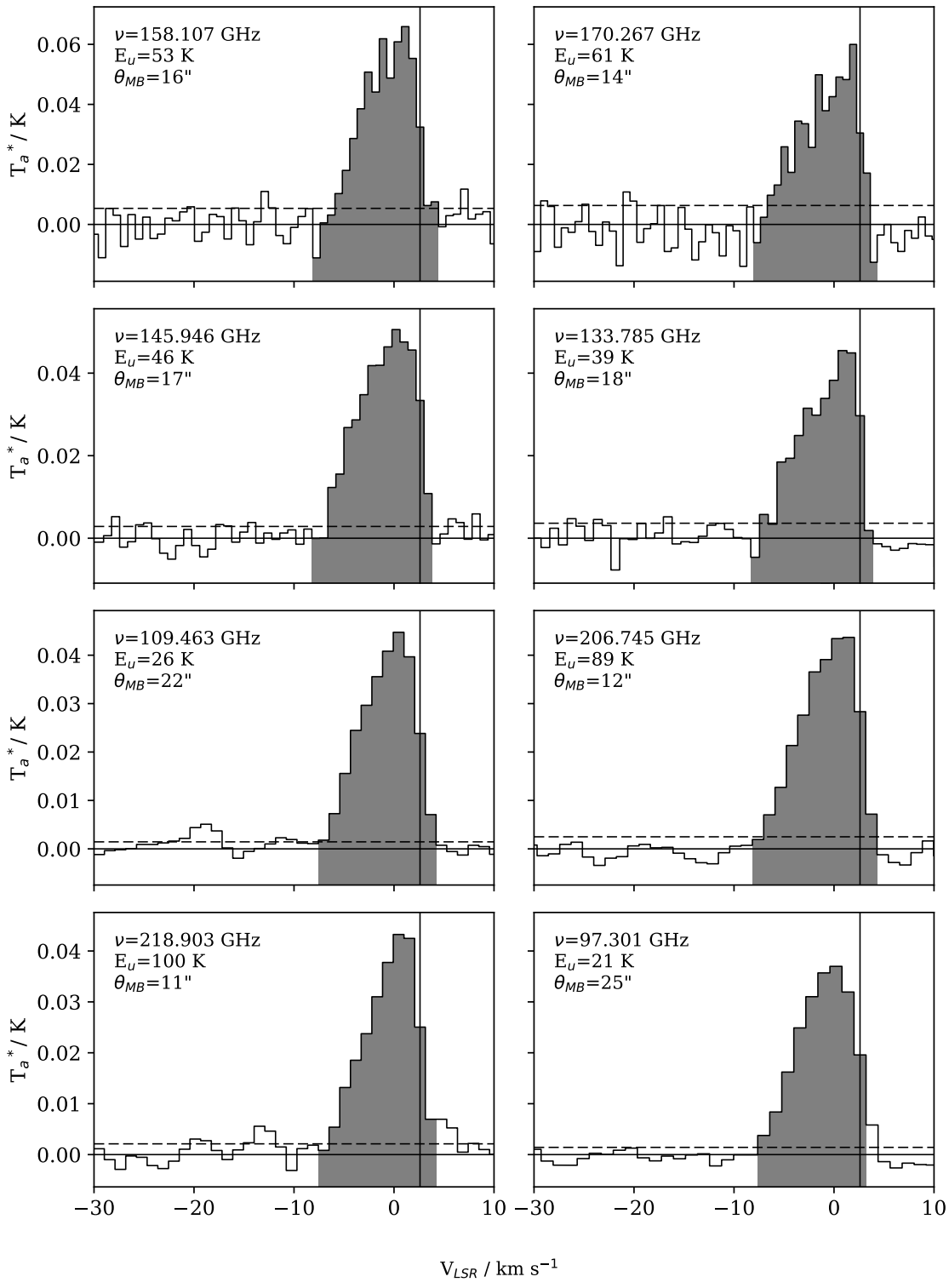

Figure A.6: Detected OCS lines. Rows share Y-axis values which are given in antenna temperature. The vertical black line indicates the location of the local standard of rest velocity $-2.6\,\mathrm{km\,s^{-1}}$. The horizontal dashed line shows the 1σ level for that spectrum, and the part of the spectrum plotted in black is the section integrated for use in this work.

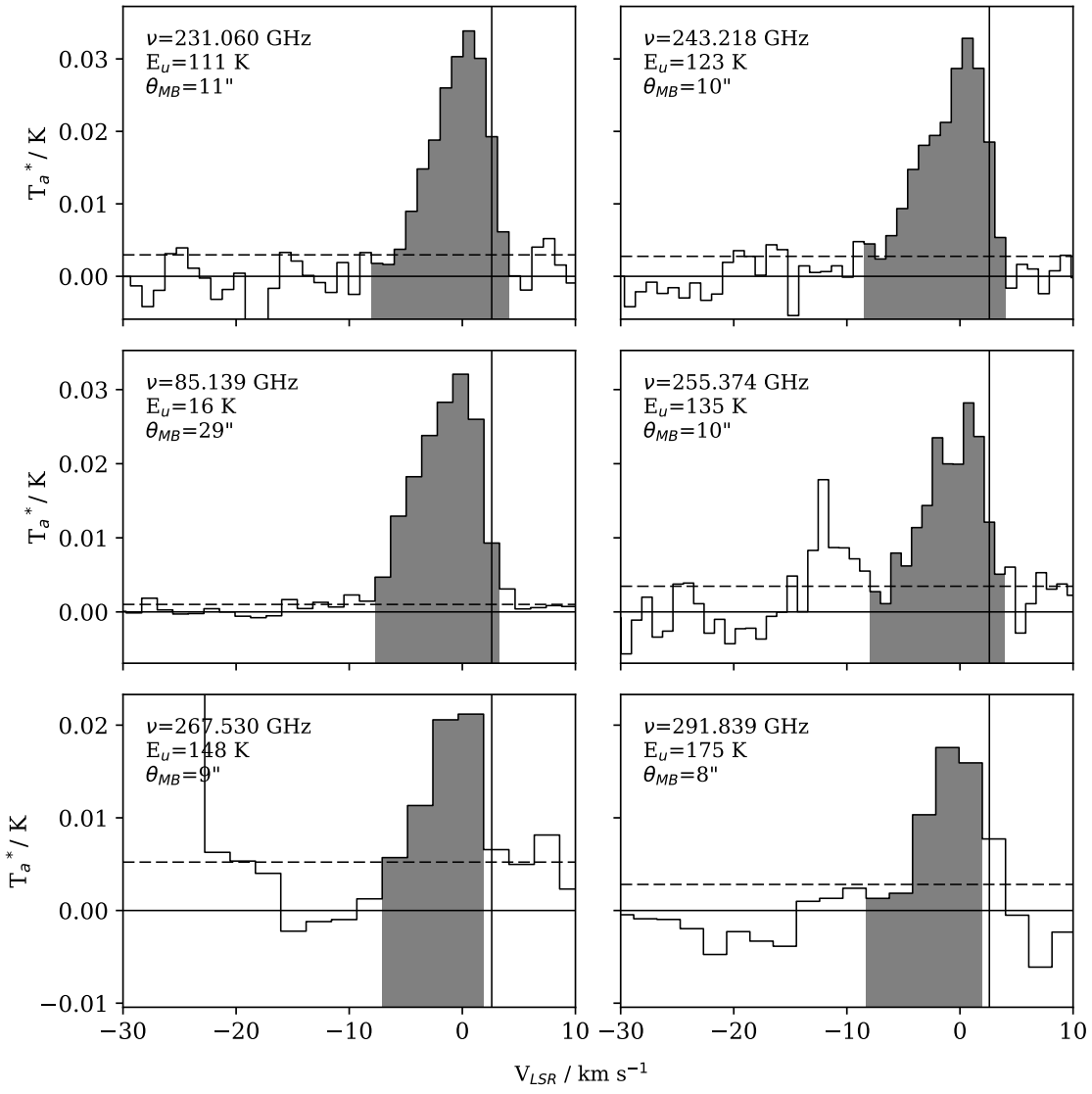

Figure A.7: Detected OCS lines cont.

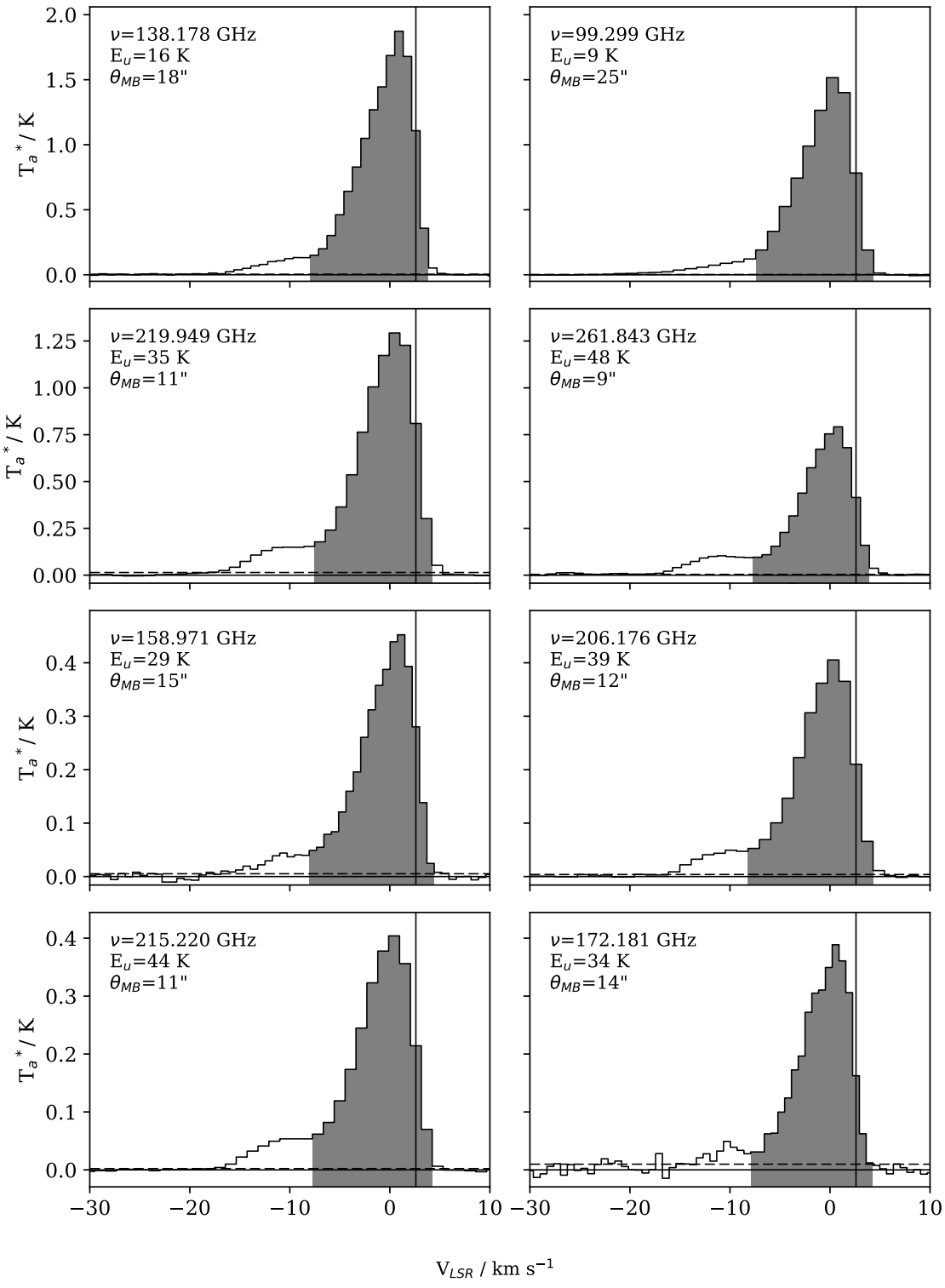

Figure A.8: Detected SO lines. Rows share Y-axis values which are given in antenna temperature. The vertical black line indicates the location of the local standard of rest velocity $-2.6\,\mathrm{km\,s^{-1}}$. The horizontal dashed line shows the 1σ level for that spectrum, and the part of the spectrum plotted in black is the section integrated for use in this work.

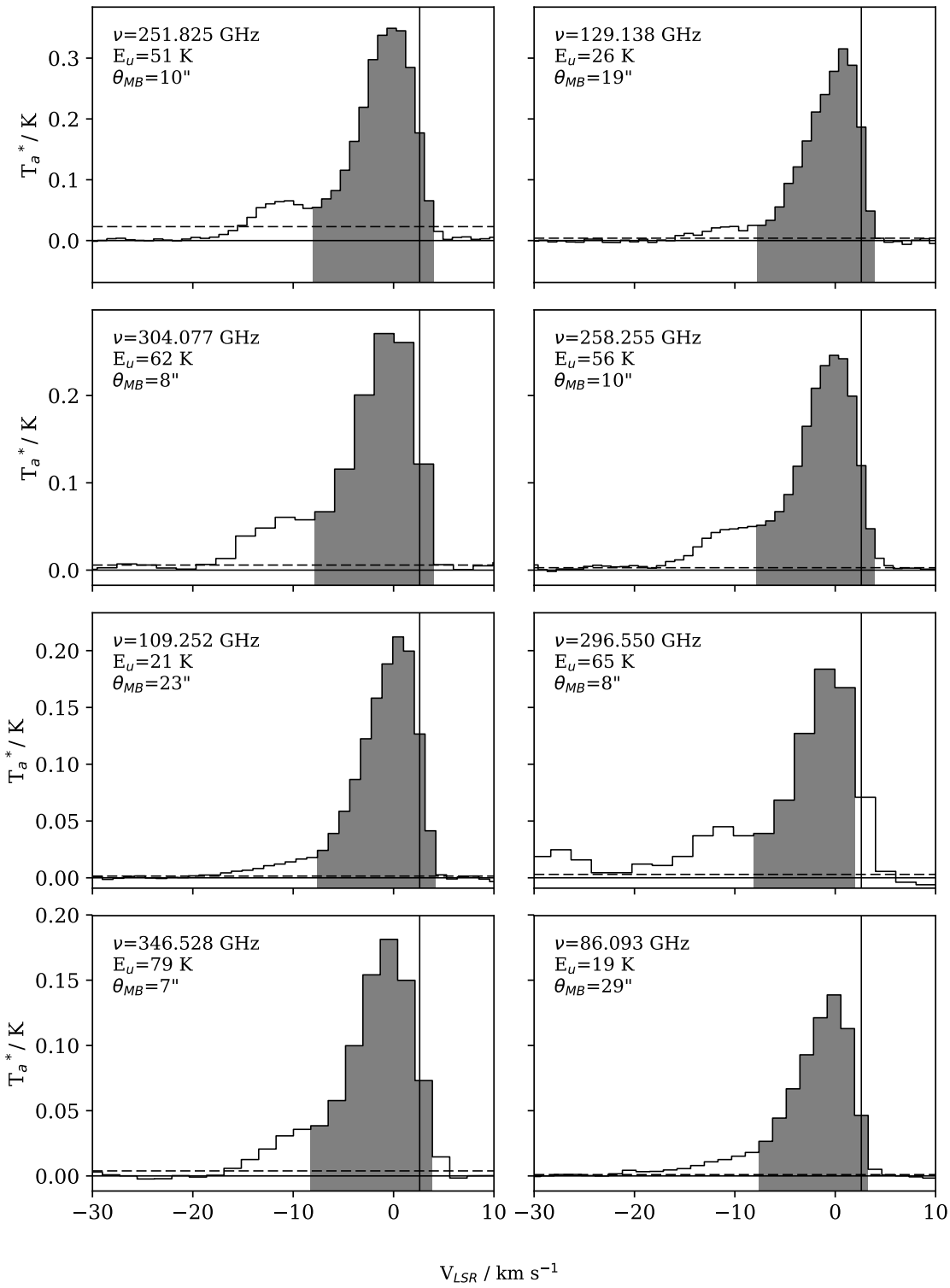

Figure A.9: Detected SO lines cont.

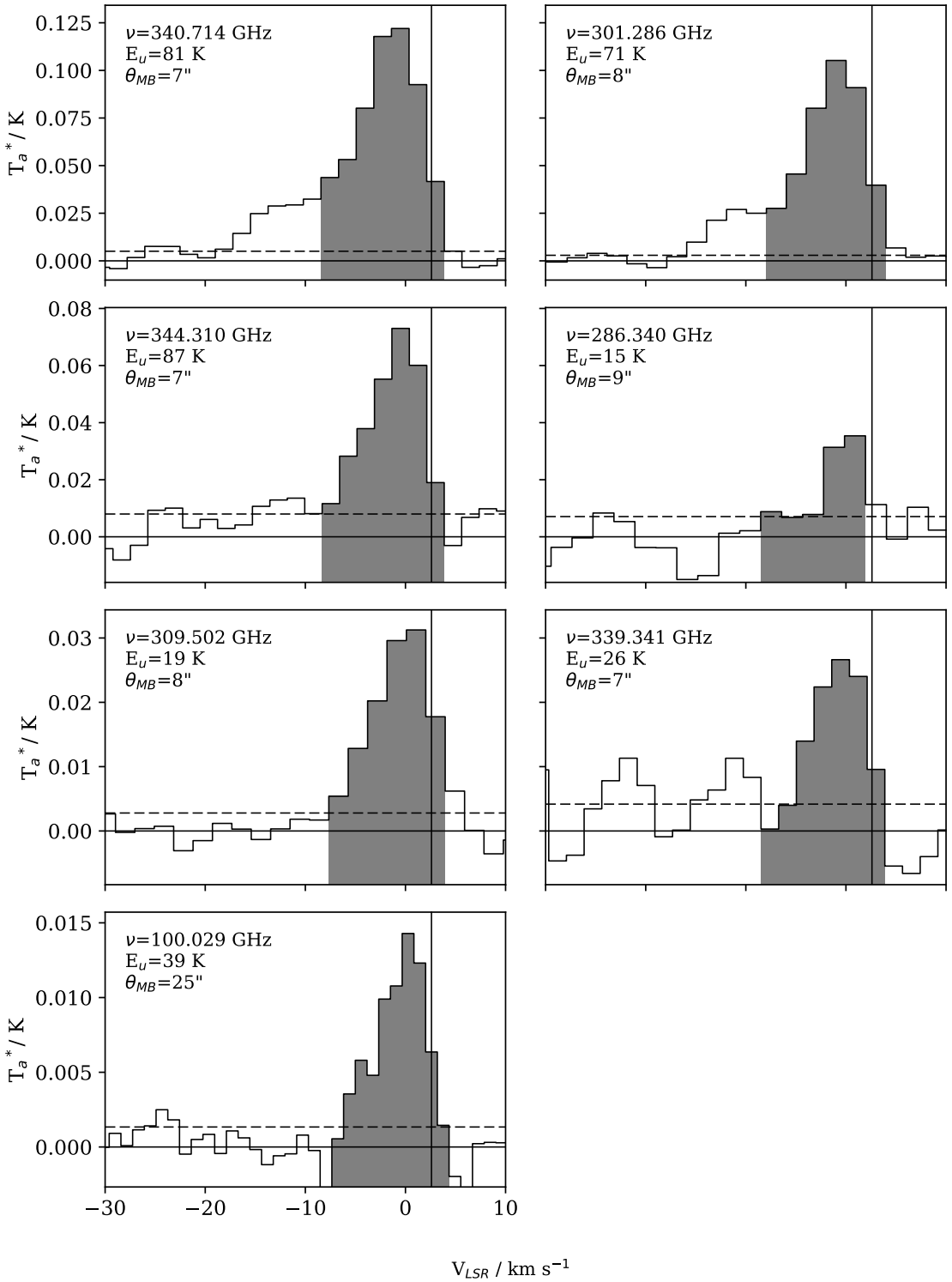

Figure A.10: Detected SO lines cont.

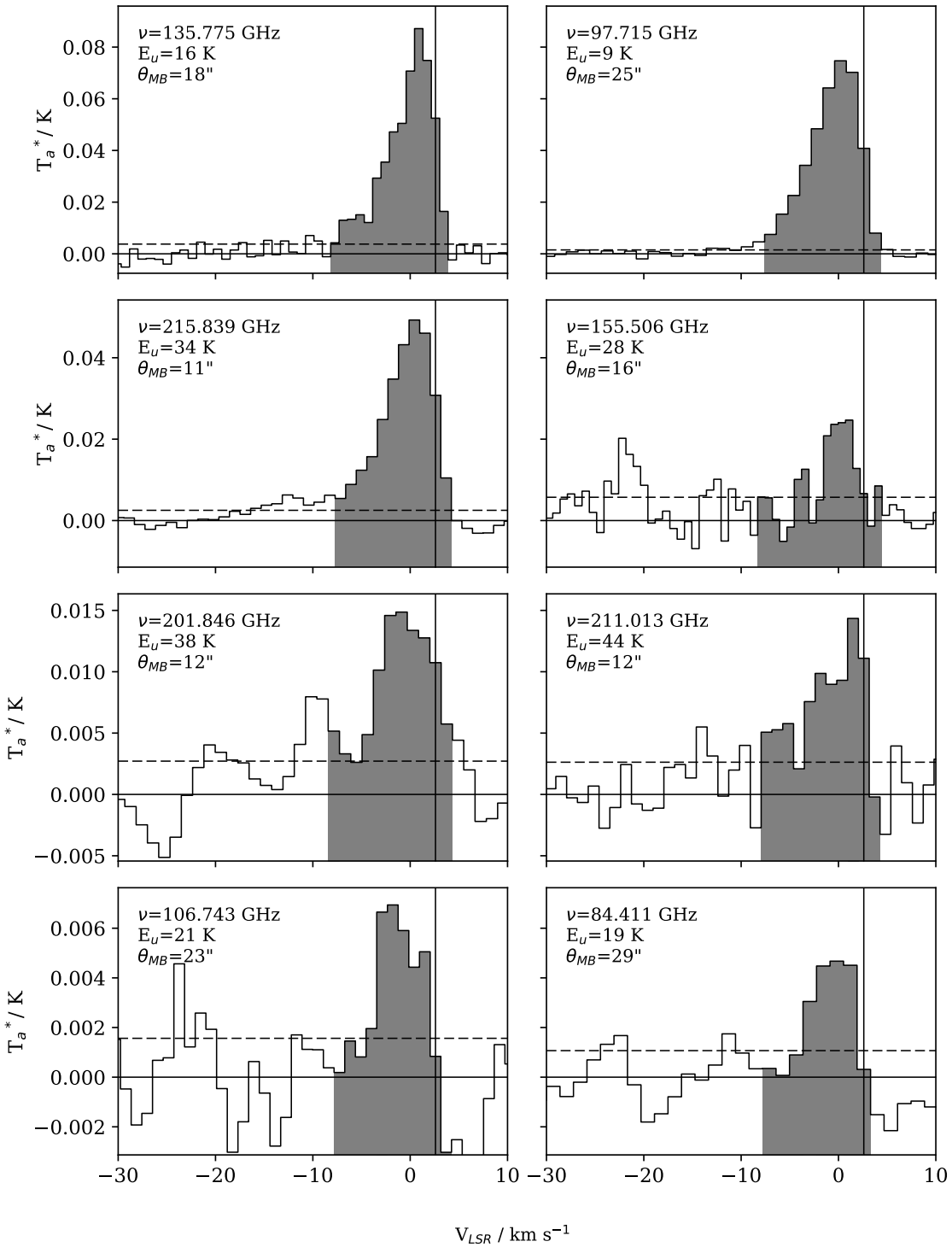

Figure A.11: Detected ^{34}SO lines. Rows share Y-axis values which are given in antenna temperature. The vertical black line indicates the location of the local standard of rest velocity $-2.6\,\mathrm{km\,s^{-1}}$. The horizontal dashed line shows the 1σ level for that spectrum, and the part of the spectrum plotted in black is the section integrated for use in this work.

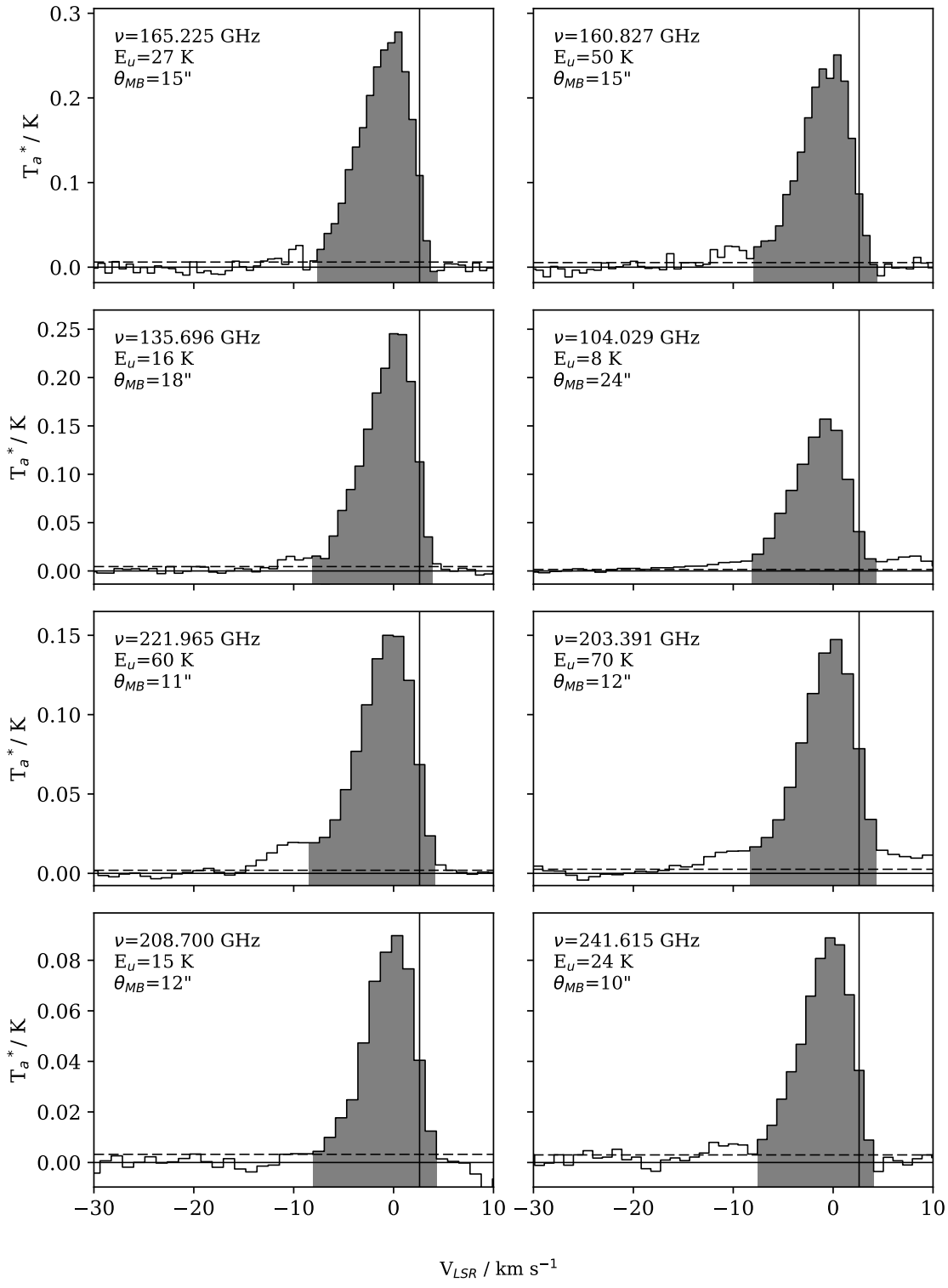

Figure A.12: Detected SO_2 lines. Rows share Y-axis values which are given in antenna temperature. The vertical black line indicates the location of the local standard of rest velocity $-2.6\,\mathrm{km\,s^{-1}}$. The horizontal dashed line shows the 1σ level for that spectrum, and the part of the spectrum plotted in black is the section integrated for use in this work.

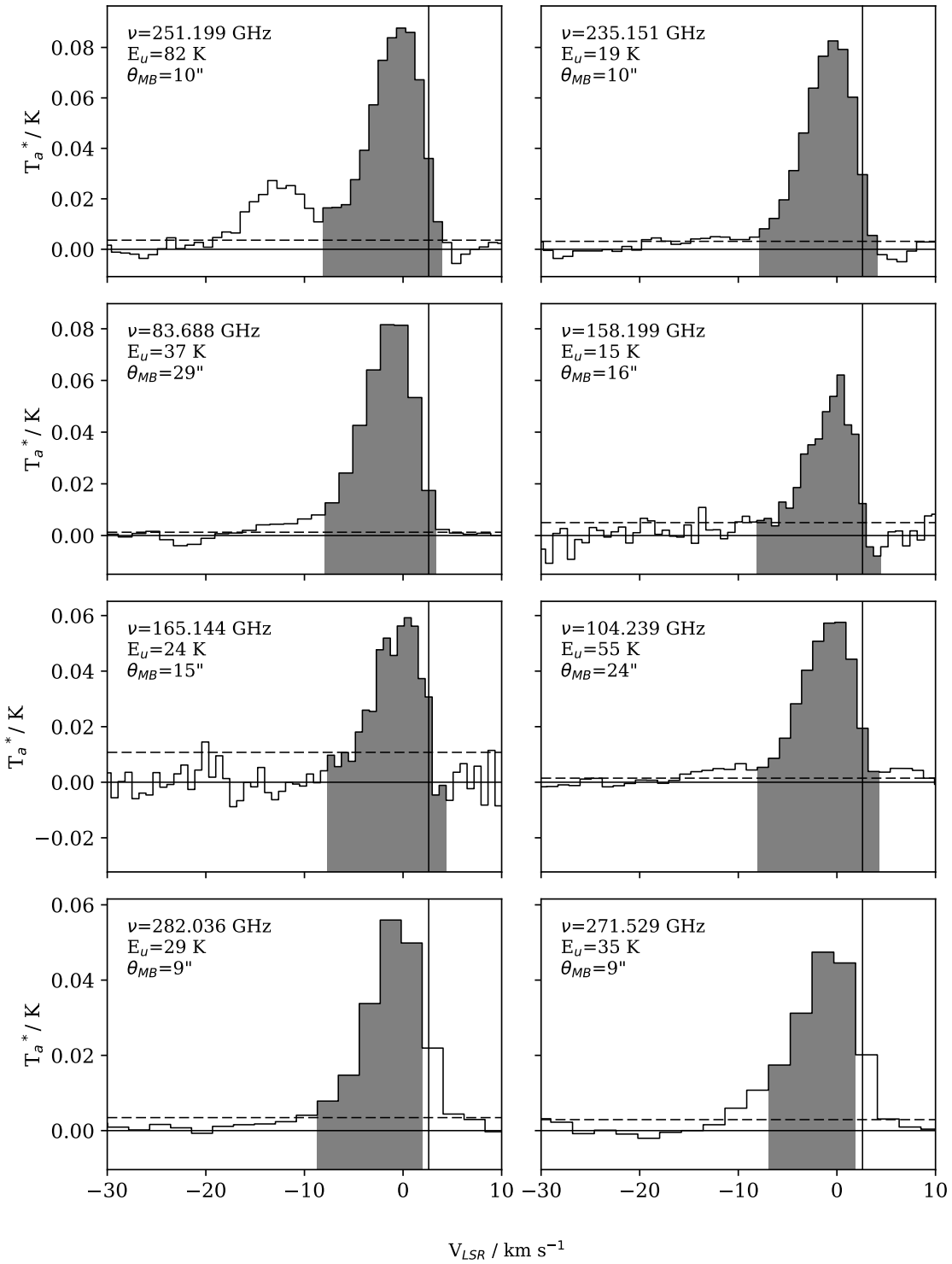

Figure A.13: Detected SO_2 lines cont.

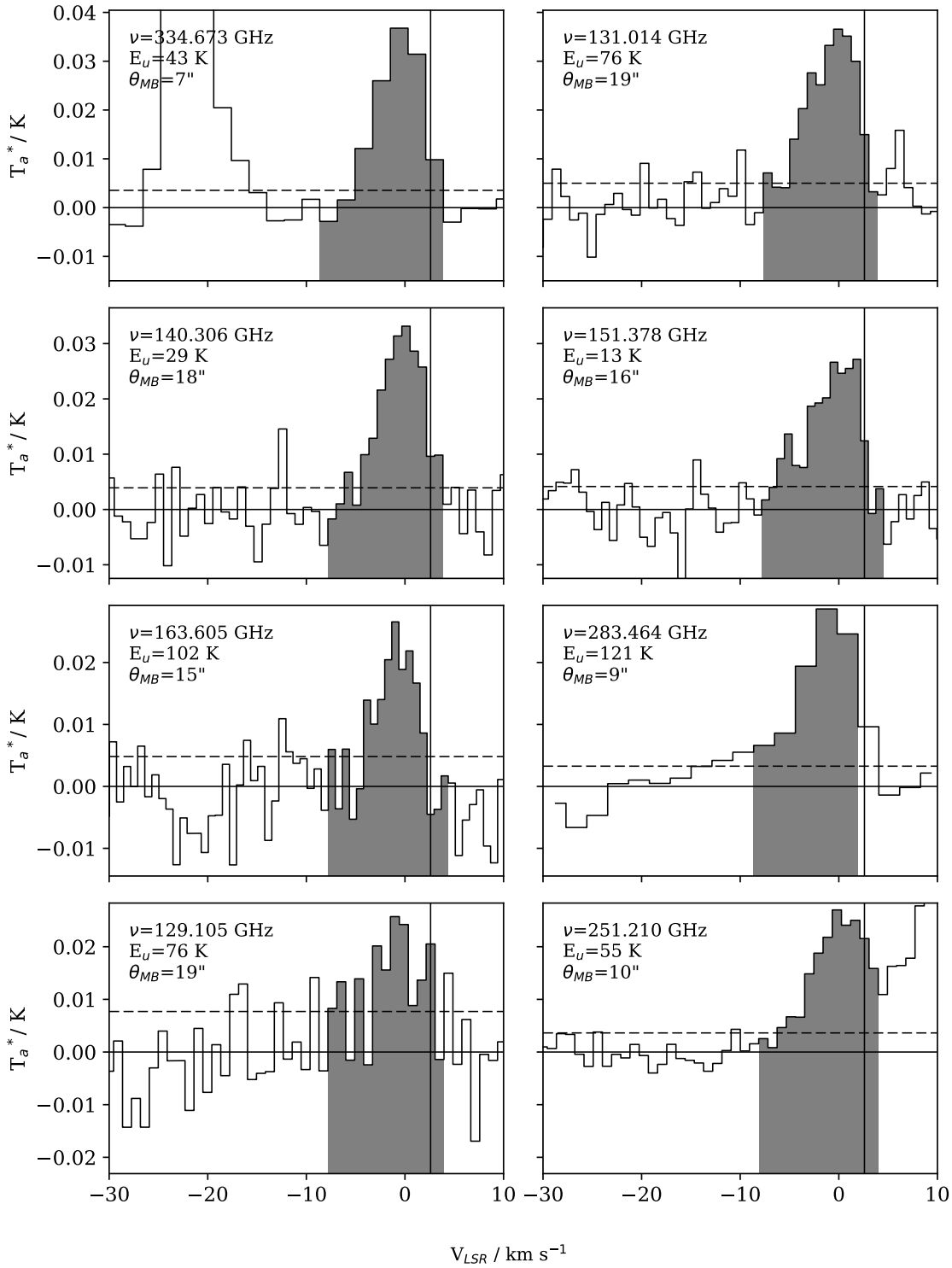

Figure A.14: Detected SO_2 lines cont.

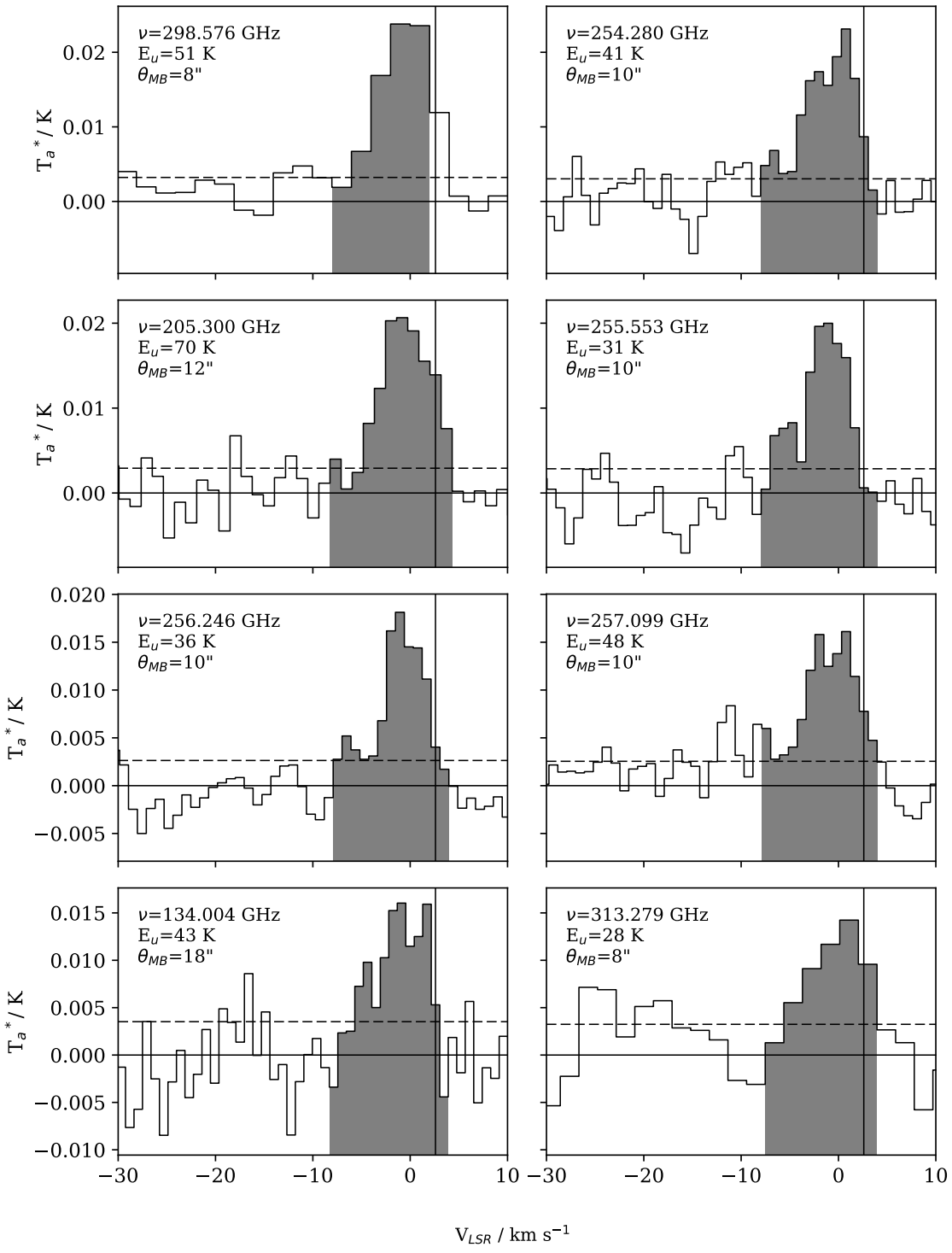

Figure A.15: Detected SO_2 lines cont.

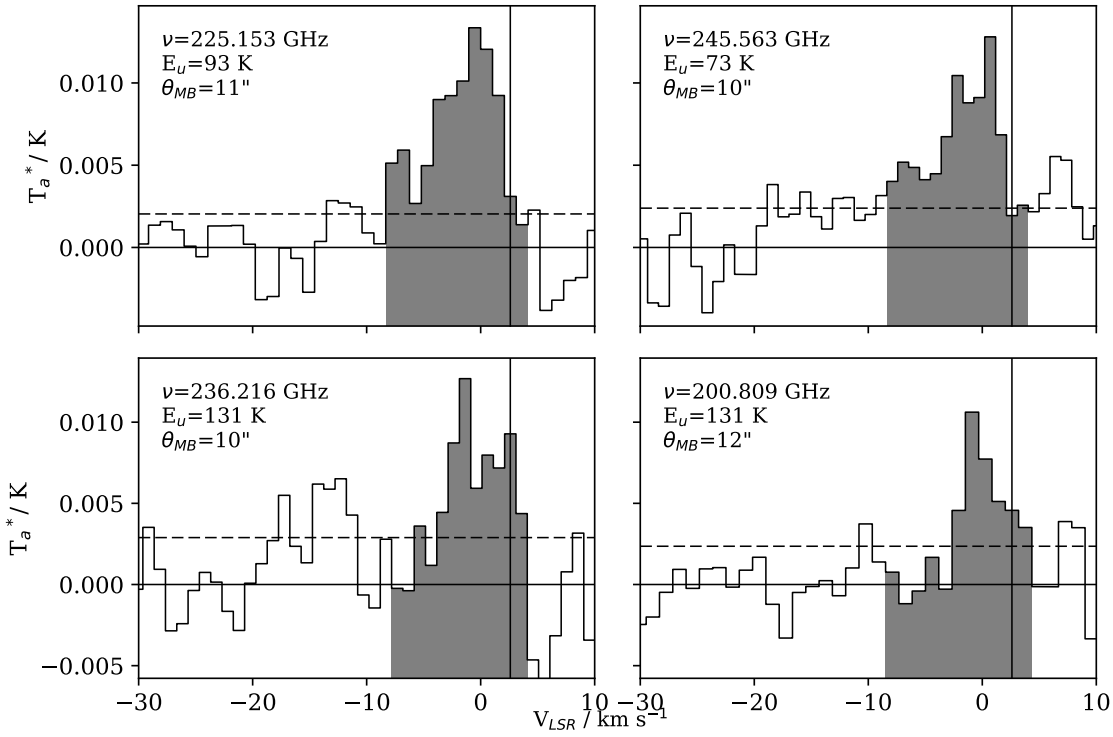

Figure A.16: Detected SO_2 lines cont.

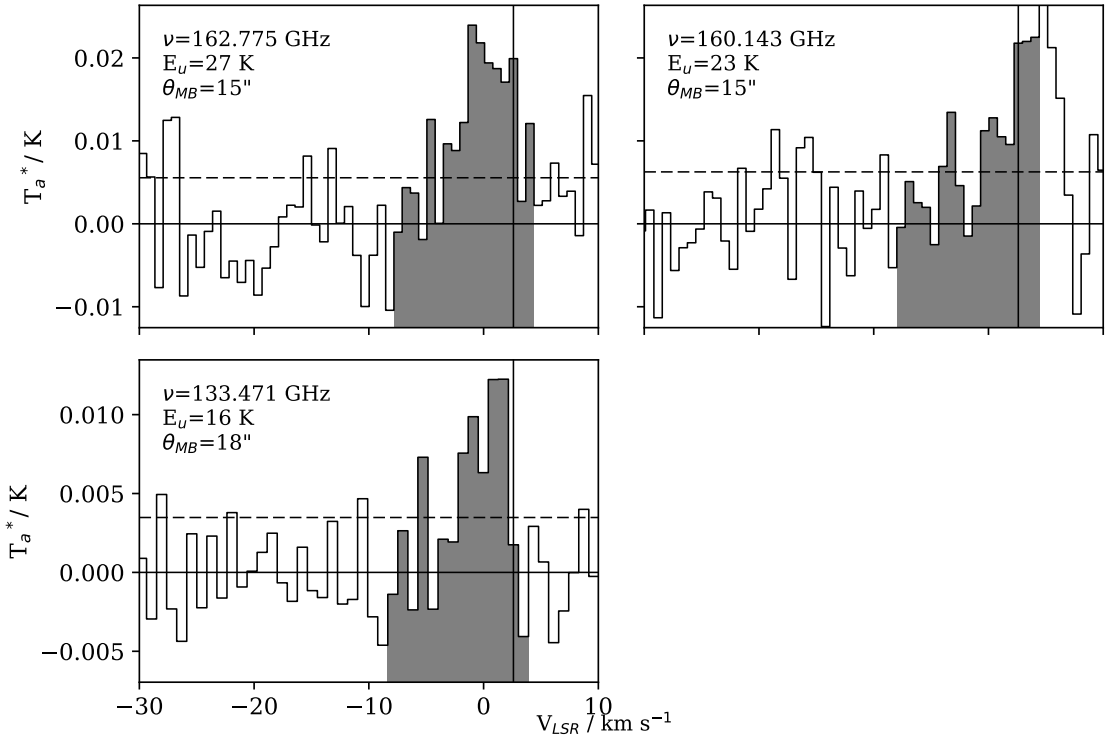

Figure A.17: Detected $^{34}SO_2$ lines. Rows share Y-axis values which are given in antenna temperature. The vertical black line indicates the location of the local standard of rest velocity $-2.6\,\mathrm{km\,s^{-1}}$. The horizontal dashed line shows the 1σ level for that spectrum, and the part of the spectrum plotted in black is the section integrated for use in this work.

Appendix B

Line Properties

Tables B.1 to B.4 give the spectroscopic and measured properties of the detected lines from Chapter 5. Spectroscopic properties are taken from the JPL catalog (Pickett 1985) via splatalogue (http://www.cv.nrao.edu/php/splat/).

Table B.1: Line properties of detected transitions

Freq (GHz)	Transition	E_u (K)	$\log(A_{ij})$	$T_{A*,peak}$ (K)	V_{peak} (km s^{-}1)	V_{min}/V_{max} (km s^{-}1)	$\int T_{MB} dv$ (K km s^{-}1)
				SO			
86.093	2(2)-1(1)	19.3	-5.27	0.139 (0.001)	-0.12	-20.52/3.96	1.07 (0.22)
99.299	3(2)-2(1)	9.2	-4.94	1.516 (0.002)	0.24	-20.99/4.96	11.31 (2.28)
100.029	4(5)-4(4)	38.6	-5.96	0.014 (0.001)	0.26	-4.42/2.60	0.09 (0.02)
109.252	2(3)-1(2)	21.1	-4.96	0.212 (0.002)	0.46	-15.62/3.67	1.64 (0.33)
129.138	3(3)-2(2)	25.5	-4.64	0.315 (0.004)	0.79	-12.79/3.51	2.31 (0.48)
138.178	4(3)-3(2)	15.9	-4.49	1.873 (0.004)	0.91	-16.02/4.29	13.91 (2.80)
158.971	3(4)-2(3)	28.7	-4.36	0.452 (0.005)	1.13	-12.84/4.07	3.67 (0.75)
172.181	4(4)-3(3)	33.8	-4.23	0.389 (0.010)	0.56	-7.59/3.28	3.05 (0.64)
206.176	4(5)-3(4)	38.6	-3.99	0.405 (0.004)	0.33	-14.44/3.74	3.97 (0.81)
215.220	5(5)-4(4)	44.1	-3.91	0.404 (0.002)	0.42	-15.90/3.69	4.09 (0.83)
219.949	6(5)-5(4)	35.0	-3.87	1.293 (0.014)	0.47	-14.44/4.73	13.17 (2.70)
251.825	5(6)-4(5)	50.7	-3.71	0.349 (0.023)	-0.19	-5.77/2.60	4.00 (0.86)
258.255	6(6)-5(5)	56.5	-3.67	0.246 (0.003)	-0.12	-16.45/4.41	2.88 (0.59)
261.843	7(6)-6(5)	47.6	-3.63	0.792 (0.004)	0.81	-16.19/4.39	8.30 (1.68)
286.340	1(1)-1(0)	15.2	-4.84	0.035 (0.007)	0.91	-1.19/0.91	0.39 (0.09)
296.550	6(7)-5(6)	64.9	-3.48	0.184 (0.003)	-1.04	-19.24/3.00	2.69 (0.56)
301.286	7(7)-6(6)	71.0	-3.46	0.105 (0.003)	-0.98	-14.91/3.00	1.64 (0.34)
304.077	8(7)-7(6)	62.1	-3.43	0.271 (0.006)	-0.94	-14.75/3.00	4.27 (0.89)
309.502	2(2)-2(1)	19.3	-4.84	0.031 (0.003)	1.06	-4.75/3.00	0.49 (0.11)
339.341	3(3)-3(2)	25.5	-4.83	0.027 (0.004)	-0.53	-4.07/1.23	0.40 (0.09)
340.714	7(8)-6(7)	81.2	-3.29	0.122 (0.005)	-0.52	-14.60/3.00	2.39 (0.51)
344.310	8(8)-7(7)	87.5	-3.28	0.073 (0.008)	-0.48	-5.71/1.26	1.21 (0.27)
346.528	9(8)-8(7)	78.8	-3.26	0.181 (0.004)	-0.46	-14.30/4.73	2.78 (0.58)

Table B.2: Line properties of detected transitions

Freq (GHz)	Transition	E_u (K)	$\log(A_{ij})$	$T_{A*,peak}$ (K)	V_{peak} (km s^{-}1)	V_{min}/V_{max} (km s^{-}1)	$\int T_{MB} dv$ (K km s^{-}1)
				SO_2			
83.688	8(1,7)-8(0,8)	36.7	-5.17	0.082 (0.001)	-1.60	-14.19/2.60	0.54 (0.11)
104.029	3(1,3)-2(0,2)	7.7	-5.00	0.157 (0.002)	-0.78	-14.28/10.48	1.24 (0.26)
104.239	10(1,9)-10(0,10)	54.7	-4.95	0.058 (0.001)	0.35	-7.51/2.60	0.46 (0.10)
129.105	12(1,11)-11(2,10)	76.4	-5.04	0.026 (0.008)	-1.02	-1.02/-0.12	0.19 (0.04)
131.014	12(1,11)-12(0,12)	76.4	-4.73	0.037 (0.005)	-0.08	-3.65/1.71	0.29 (0.07)
134.004	8(2,6)-8(1,7)	43.1	-4.60	0.016 (0.004)	-0.89	-1.76/1.73	0.11 (0.03)
135.696	5(1,5)-4(0,4)	15.7	-4.66	0.245 (0.005)	0.02	-6.02/3.46	1.83 (0.38)
140.306	6(2,4)-6(1,5)	29.2	-4.60	0.033 (0.004)	0.10	-3.23/1.77	0.22 (0.05)
151.378	2(2,0)-2(1,1)	12.6	-4.73	0.027 (0.004)	1.83	-2.81/1.83	0.21 (0.05)
158.199	3(2,2)-3(1,3)	15.3	-4.60	0.062 (0.005)	0.38	-4.05/1.86	0.39 (0.09)
160.827	10(0,10)-9(1,9)	49.7	-4.40	0.251 (0.005)	0.42	-7.58/3.33	1.95 (0.41)
163.605	14(1,13)-14(0,14)	101.8	-4.52	0.027 (0.005)	-0.98	-1.69/1.17	0.12 (0.03)
165.144	5(2,4)-5(1,5)	23.6	-4.51	0.059 (0.011)	0.48	-2.36/1.89	0.45 (0.11)
165.225	7(1,7)-6(0,6)	27.1	-4.38	0.278 (0.006)	0.48	-7.31/3.31	2.24 (0.46)
200.809	16(1,15)-16(0,16)	130.7	-4.33	0.011 (0.002)	-0.90	-0.90/0.27	0.06 (0.02)
203.391	12(0,12)-11(1,11)	70.1	-4.06	0.147 (0.003)	0.30	-12.37/14.12	1.50 (0.31)
205.300	11(2,10)-11(1,11)	70.2	-4.27	0.021 (0.003)	-0.82	-3.11/2.60	0.21 (0.05)
208.700	3(2,2)-2(1,1)	15.3	-4.17	0.090 (0.003)	0.36	-6.38/3.72	0.81 (0.17)
221.965	11(1,11)-10(0,10)	60.4	-3.94	0.150 (0.002)	-0.57	-13.23/3.66	1.60 (0.33)
225.153	13(2,12)-13(1,13)	93.0	-4.19	0.013 (0.002)	-0.52	-3.64/1.56	0.14 (0.03)
235.151	4(2,2)-3(1,3)	19.0	-4.11	0.083 (0.003)	-0.39	-6.37/2.60	0.81 (0.17)
236.216	16(1,15)-15(2,14)	130.7	-4.12	0.013 (0.003)	-1.37	-2.36/-1.37	0.09 (0.02)
241.615	5(2,4)-4(1,3)	23.6	-4.07	0.089 (0.003)	-0.31	-7.10/2.60	0.88 (0.18)
245.563	10(3,7)-10(2,8)	72.7	-3.92	0.013 (0.002)	0.69	-2.17/0.69	0.14 (0.03)
251.199	13(1,13)-12(0,12)	82.2	-3.76	0.088 (0.004)	-0.20	-16.05/3.53	0.96 (0.21)
251.210	8(3,5)-8(2,6)	55.2	-3.92	0.026 (0.004)	-0.20	-3.00/3.53	0.30 (0.07)
254.280	6(3,3)-6(2,4)	41.4	-3.94	0.023 (0.003)	0.76	-3.85/1.68	0.23 (0.05)
255.553	4(3,1)-4(2,2)	31.3	-4.03	0.020 (0.003)	-1.07	-2.90/0.77	0.18 (0.04)
256.246	5(3,3)-5(2,4)	35.9	-3.97	0.018 (0.003)	-1.06	-1.97/1.69	0.15 (0.04)
257.099	7(3,5)-7(2,6)	47.8	-3.91	0.016 (0.003)	0.78	-2.87/2.60	0.19 (0.04)
271.529	7(2,6)-6(1,5)	35.5	-3.96	0.047 (0.003)	-1.42	-8.04/3.00	0.67 (0.15)
282.036	6(2,4)-5(1,5)	29.2	-4.00	0.056 (0.003)	-1.25	-5.50/3.00	0.73 (0.16)
283.464	16(0,16)-15(1,15)	121.0	-3.57	0.026 (0.003)	-1.23	-3.35/0.88	0.32 (0.07)
298.576	9(2,8)-8(1,7)	51.0	-3.84	0.024 (0.003)	-1.02	-3.02/3.00	0.34 (0.08)
313.279	3(3,1)-2(2,0)	27.6	-3.47	0.014 (0.003)	1.09	-0.83/1.09	0.21 (0.05)
334.673	8(2,6)-7(1,7)	43.1	-3.90	0.037 (0.004)	-0.58	-4.17/1.21	0.46 (0.10)

Table B.3: Line properties of detected transitions

Freq (GHz)	Transition	E_u (K)	$\log(A_{ij})$	$T_{A*,peak}$ (K)	V_{peak} (km s^{-}1)	V_{min}/V_{max} (km s^{-}1)	$\int T_{MB} dv$ (K km s^{-}1)
				H_2CS			
103.039	3(2,2)-2(2,1)	62.6	-5.08	0.058 (0.002)	-1.95	-7.63/1.46	0.47 (0.10)
103.051	3(2,1)-2(2,0)	62.6	-5.08	0.010 (0.002)	0.33	-3.08/0.33	0.07 (0.02)
104.617	3(1,2)-2(1,1)	23.2	-4.86	0.085 (0.002)	-0.76	-7.47/4.84	0.71 (0.15)
135.298	4(1,4)-3(1,3)	29.4	-4.49	0.112 (0.003)	0.00	-6.92/3.47	0.89 (0.19)
137.369	4(3,2)-3(3,1)	134.9	-4.80	0.084 (0.004)	-2.51	-9.33/1.75	0.77 (0.17)
137.371	4(0,4)-3(0,3)	16.5	-4.44	0.084 (0.005)	0.90	-5.07/6.01	0.78 (0.17)
137.382	4(2,3)-3(2,2)	69.2	-4.56	0.018 (0.005)	-0.81	-1.66/-0.81	0.13 (0.03)
139.483	4(1,3)-3(1,2)	29.9	-4.45	0.111 (0.003)	0.08	-5.80/6.80	0.98 (0.21)
169.114	5(1,5)-4(1,4)	37.5	-4.18	0.122 (0.005)	-0.86	-5.71/3.29	1.06 (0.23)
171.688	5(0,5)-4(0,4)	24.7	-4.14	0.069 (0.008)	-0.81	-4.22/1.24	0.43 (0.10)
171.711	5(3,3)-4(3,2)	143.1	-4.33	0.053 (0.009)	-0.13	-0.81/1.24	0.32 (0.07)
205.987	6(0,6)-5(0,5)	34.6	-3.89	0.039 (0.003)	0.33	-5.36/2.60	0.40 (0.09)
206.052	6(3,4)-5(3,3)	153.0	-4.02	0.061 (0.003)	-0.81	-7.63/2.60	0.69 (0.15)
206.054	6(2,5)-5(2,4)	87.3	-3.95	0.061 (0.003)	1.46	-6.50/4.87	0.69 (0.15)
206.158	6(2,4)-5(2,3)	87.3	-3.95	0.021 (0.004)	-1.95	-3.08/1.46	0.19 (0.05)
209.200	6(1,5)-5(1,4)	48.3	-3.89	0.076 (0.003)	-0.76	-6.36/2.60	0.74 (0.16)
240.266	7(0,7)-6(0,6)	46.1	-3.69	0.035 (0.002)	-1.30	-5.20/6.50	0.37 (0.08)
240.382	7(2,6)-6(2,5)	98.9	-3.73	0.013 (0.003)	0.65	0.65/1.63	0.12 (0.03)
240.393	7(3,5)-6(3,4)	164.5	-3.78	0.037 (0.003)	-2.27	-7.14/1.63	0.41 (0.09)
240.549	7(2,5)-6(2,4)	98.9	-3.73	0.017 (0.003)	-1.30	-3.24/1.63	0.17 (0.04)
244.048	7(1,6)-6(1,5)	60.0	-3.68	0.058 (0.003)	-1.24	-7.00/3.56	0.63 (0.13)
270.521	8(1,8)-7(1,7)	71.6	-3.54	0.035 (0.004)	-1.43	-3.65/3.00	0.48 (0.11)
274.732	8(3,6)-7(3,5)	177.7	-3.58	0.022 (0.004)	-1.36	-3.55/0.82	0.32 (0.08)
278.887	8(1,7)-7(1,6)	73.4	-3.50	0.030 (0.004)	-1.30	-3.45/0.85	0.41 (0.09)
				OCS			
85.139	7-6	16.3	-5.77	0.032 (0.001)	-0.15	-7.03/3.98	0.22 (0.05)
97.301	8-7	21.0	-5.59	0.037 (0.001)	0.19	-5.82/3.80	0.30 (0.07)
109.463	9-8	26.3	-5.43	0.045 (0.001)	0.46	-5.96/3.67	0.35 (0.07)
133.785	11-10	38.5	-5.17	0.045 (0.004)	0.85	-5.27/2.60	0.34 (0.08)
145.946	12-11	45.5	-5.05	0.051 (0.003)	0.20	-6.21/3.40	0.44 (0.10)
158.107	13-12	53.1	-4.95	0.066 (0.005)	1.12	-4.79/2.60	0.51 (0.11)
170.267	14-13	61.3	-4.85	0.060 (0.006)	1.91	-3.58/2.60	0.45 (0.10)
206.745	17-16	89.3	-4.59	0.044 (0.002)	1.47	-5.33/2.60	0.45 (0.10)
218.903	18-17	99.8	-4.52	0.043 (0.002)	0.46	-4.89/4.74	0.43 (0.09)
231.060	19-18	110.9	-4.45	0.034 (0.003)	0.57	-4.50/2.60	0.31 (0.07)
243.218	20-19	122.6	-4.38	0.033 (0.003)	0.67	-5.11/2.60	0.33 (0.07)
255.374	21-20	134.8	-4.32	0.028 (0.003)	0.77	-3.82/2.60	0.28 (0.06)
267.530	22-21	147.7	-4.25	0.021 (0.005)	0.76	-1.48/0.76	0.27 (0.07)
291.839	24-23	175.1	-4.14	0.017 (0.003)	-1.11	-3.16/0.95	0.21 (0.05)

Table B.4: Line properties of detected transitions

Freq (GHz)	Transition	E_u (K)	$\log(A_{ij})$	$T_{A*,peak}$ (K)	V_{peak} (km s^{-}1)	V_{min}/V_{max} (km s^{-}1)	$\int T_{MB} dv$ (K km s^{-}1)
				CCS			
81.505	N=6-5,J=7-6	15.4	-4.61	0.033 (0.002)	-0.27	-6.02/2.60	0.19 (0.04)
86.181	N=7-6,J=6-5	23.3	-4.55	0.011 (0.001)	-0.12	-4.19/5.32	0.08 (0.02)
90.686	N=7-6,J=7-6	26.1	-4.48	0.011 (0.002)	0.02	-2.57/2.60	0.08 (0.02)
93.870	N=7-6,J=8-7	19.9	-4.42	0.031 (0.001)	0.11	-4.88/2.60	0.20 (0.04)
99.866	N=8-7,J=7-6	28.1	-4.35	0.011 (0.001)	-0.92	-3.26/1.43	0.07 (0.02)
103.640	N=8-7,J=8-7	31.1	-4.30	0.008 (0.002)	-0.79	-0.79/0.34	0.05 (0.01)
106.347	N=8-7,J=9-8	25.0	-4.25	0.031 (0.002)	0.40	-5.11/2.60	0.20 (0.05)
113.410	N=9-8,J=8-7	33.6	-4.18	0.016 (0.002)	0.53	-2.56/1.57	0.06 (0.02)
131.551	N=10-9,J=11-10	37.0	-3.97	0.024 (0.004)	-0.07	-0.96/1.71	0.12 (0.03)
142.501	N=11-10,J=11-10	49.7	-3.87	0.016 (0.004)	0.14	0.14/0.96	0.10 (0.02)
144.244	N=11-10,J=12-11	43.9	-3.85	0.019 (0.003)	-1.45	-2.26/1.79	0.11 (0.03)
156.981	N=12-11,J=13-12	51.5	-3.74	0.023 (0.006)	-1.12	-1.12/1.86	0.13 (0.03)
166.662	N=13-12,J=12-11	61.8	-3.66	0.024 (0.005)	-0.21	-0.91/0.50	0.08 (0.02)
				$^{34}SO_2$			
133.471	5(1,5)-4(0,4)	15.6	-4.68	0.012 (0.003)	1.72	0.85/1.72	0.06 (0.01)
160.143	5(2,4)-5(1,5)	23.3	-4.55	0.022 (0.006)	3.33	2.60/5.52	0.18 (0.04)
162.775	7(1,7)-6(0,6)	27.0	-4.40	0.024 (0.006)	-0.99	-0.99/2.60	0.17 (0.04)
				^{34}SO			
84.411	2(2)-1(1)	19.2	-5.30	0.005 (0.001)	-0.17	-1.56/1.21	0.02 (0.01)
97.715	3(2)-2(1)	9.1	-4.96	0.075 (0.002)	0.20	-8.19/3.80	0.56 (0.12)
106.743	2(3)-1(2)	20.9	-4.99	0.007 (0.002)	-1.79	-2.89/-0.69	0.03 (0.01)
135.775	4(3)-3(2)	15.6	-4.51	0.087 (0.004)	0.88	-6.87/3.46	0.56 (0.12)
155.506	3(4)-2(3)	28.4	-4.39	0.025 (0.006)	1.10	-1.16/1.10	0.15 (0.04)
201.846	4(5)-3(4)	38.1	-4.02	0.015 (0.003)	-0.88	-3.20/2.60	0.19 (0.05)
211.013	5(5)-4(4)	43.5	-3.94	0.014 (0.003)	1.49	-1.84/2.60	0.13 (0.03)
215.839	6(5)-5(4)	34.4	-3.89	0.049 (0.003)	0.43	-6.08/3.69	0.47 (0.10)

This page was intentionally left blank

Appendix C

RADEX Probability Distributions

Figures C.1 to C.6 show the marginalized probability distributions derived from RADEX for the temperature, gas density and column density for H_2CS, OCS, SO and SO_2 along with the joint probability distributions for each pair of variables. A key result to note from these distributions is the lack of correlation between the column density and the other variables for each species. This indicates that the value derived for the column density is largely independent of the uncertainties in the gas properties. For further details, see Section 5.3.1

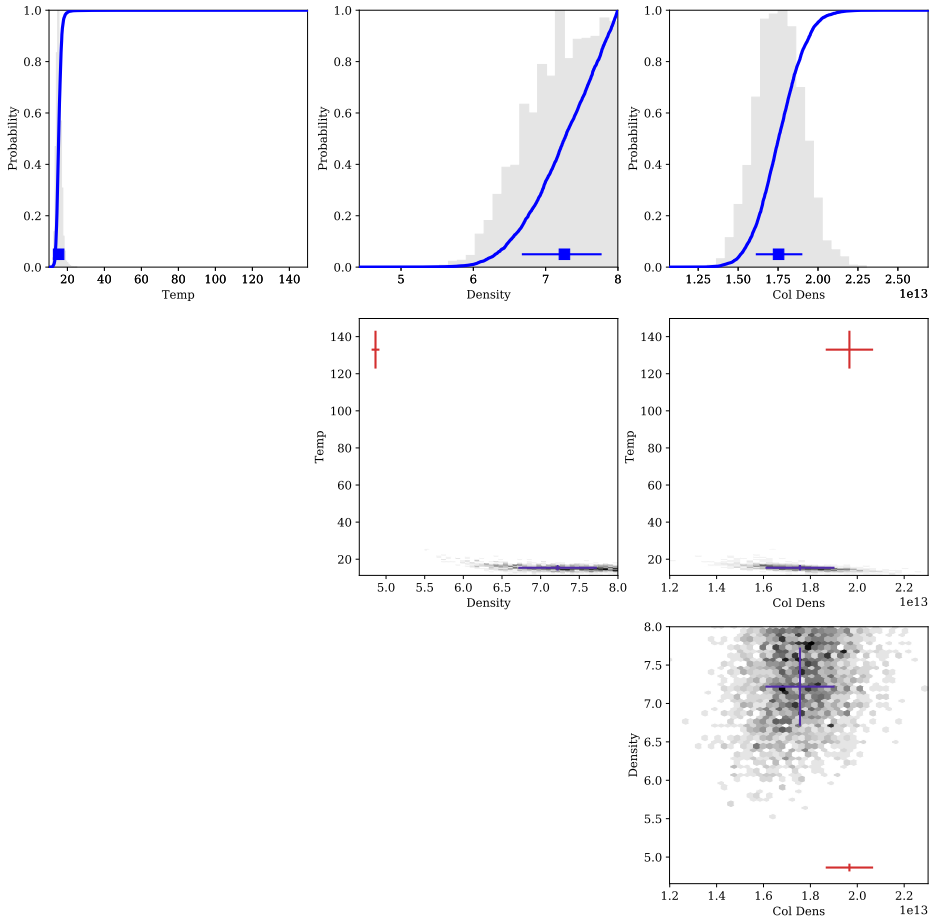

Figure C.1: Probability distributions for o-H_2CS, the only species not to constrain the temperature. o-H_2CS is also unique in the particularly low density. The column densities demonstrate the general trend of having a most likely value that is not strongly dependent on density and temperature. The orange and blue crosses represent the 67% confidence intervals of peaks in the probabilty distribution. Whilst technically a peak, the orange cross contains much less of the total probability density and so is not visible in the grey scale.

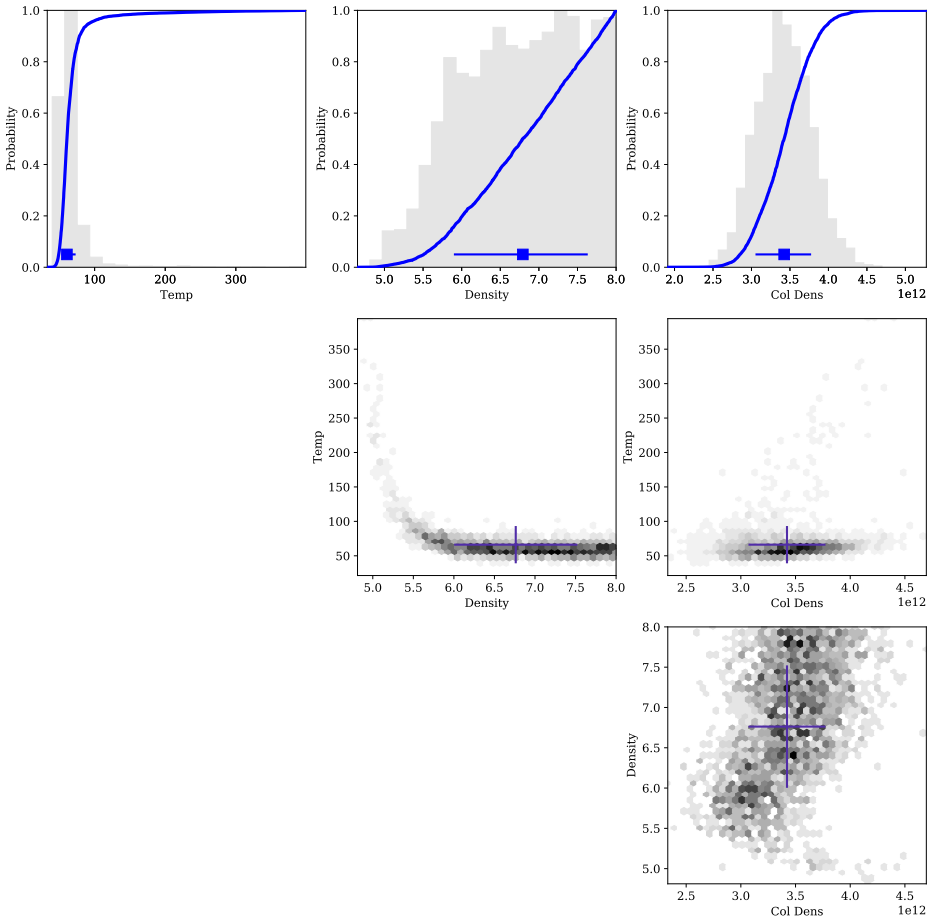

Figure C.2: Probability distributions for p-H_2CS, favouring temperatures ∼60 K which is consistent with the gas temperature derived for CS in L1157-B1 (Gómez-Ruiz et al. 2015). The density tends towards high values which is a trend seen in many species but the column density appears to be largely uncorrelated with the density. The blue cross represent the 67% confidence intervals of the probabilty distribution.

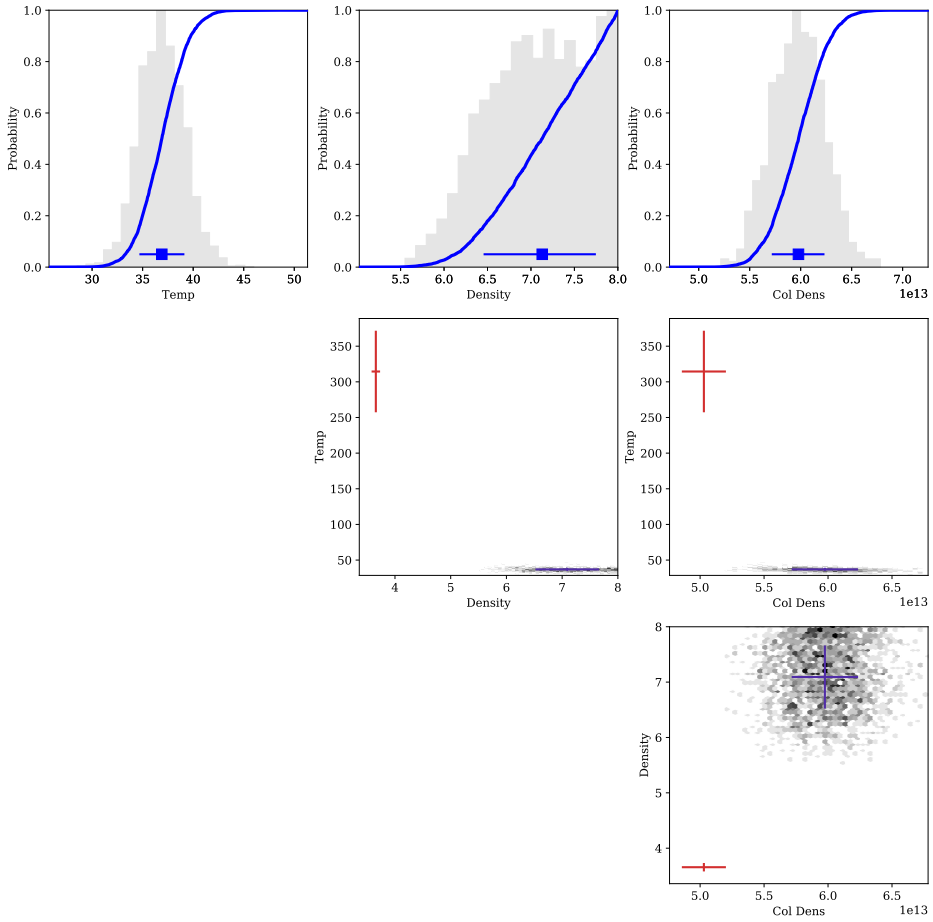

Figure C.3: Probability distributions for OCS. Demonstrating a tendency towards higher densities and a strong peak at low temperatures. However, once again showing a clear column density peak regardless of density. The orange and blue crosses represent the 67% confidence intervals of peaks in the probabilty distribution. Whilst technically a peak, the orange cross contains much less of the total probability density and so is not visible in the grey scale.

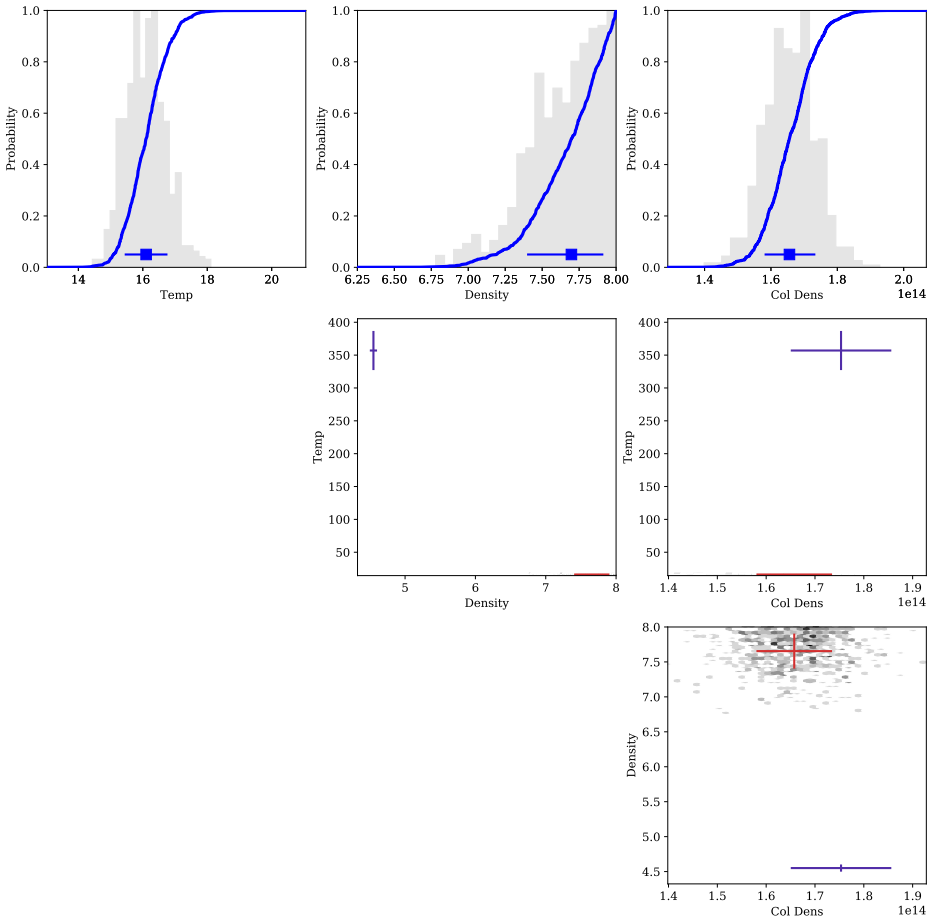

Figure C.4: Probability distributions for SO. Similar to OCS, SO shows no strong constraint on the density. Nevertheless, the SO column density has a clear most likely value. It also gives a strong peak at temperatures much lower than other molecules.

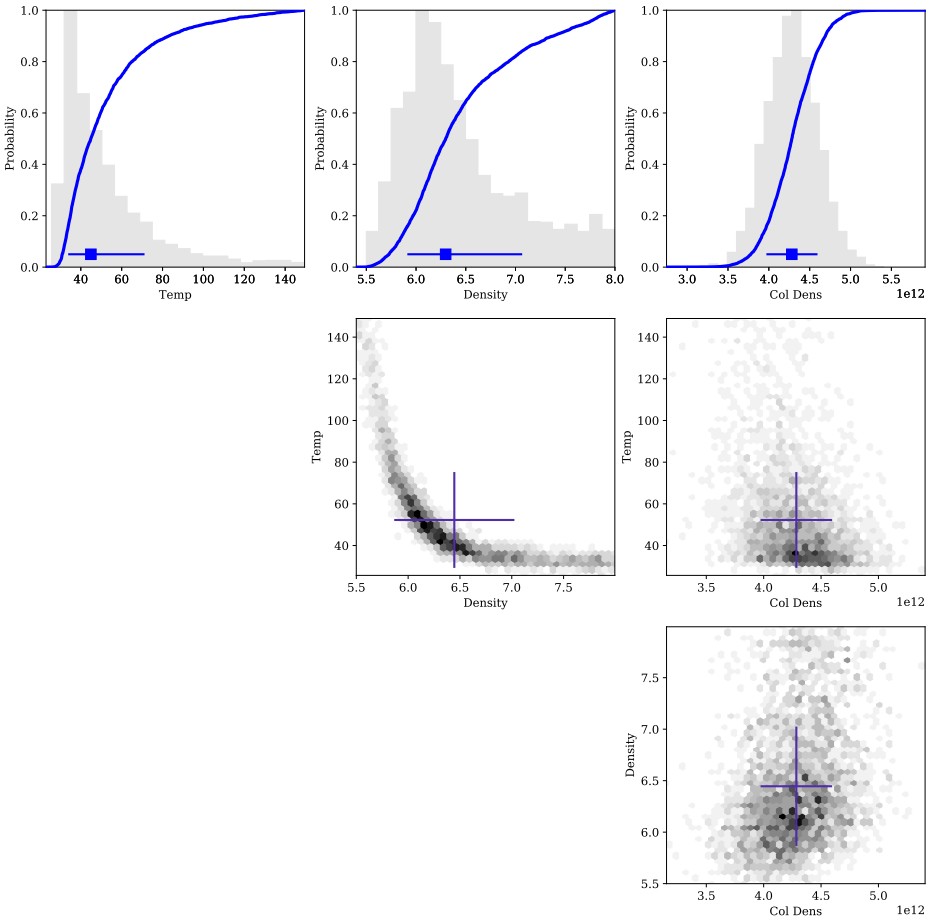

Figure C.5: Probability distributions for secondary SO emission. The temperature is poorly constrained but has a lower limit of ∼50K. Nevertheless, the gas density and molecular column density are well constrained. The central panel shows the joint probability distribution of the gas temperature and density, it is similar to the χ^2 distribution for the secondary emission of CS in B1a shown in Figure 7 of Benedettini et al. (2013), possibly indicating the secondary SO emission comes from the same region (See Section 5.3.3.

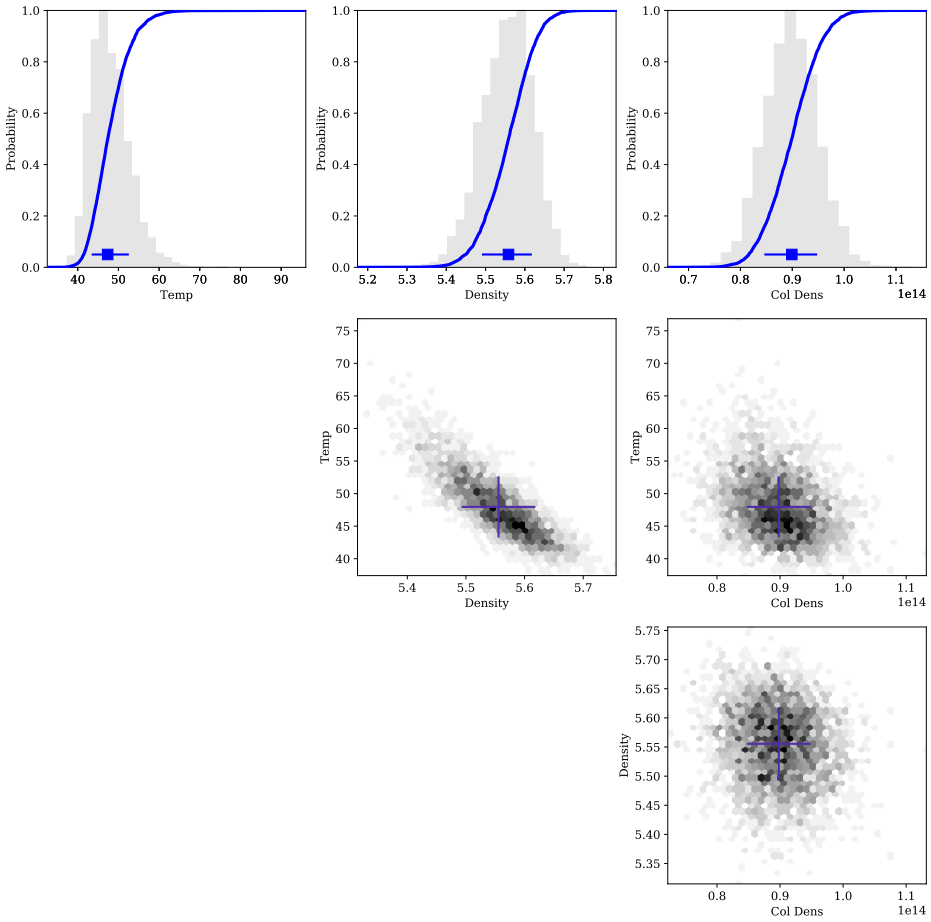

Figure C.6: Probability distributions for SO_2. SO_2 is unique in that it shows a single peak distribution for all input parameters. There are noisy sections of the distributions where random combinations of temperature and density give acceptable models but there are very strong central peaks for each parameter.

This page was intentionally left blank

Bibliography

S. Anderl, V. Guillet, A. P. Jones, and G. Pineau des Forêts. Shocks in dense clouds. *Astron. Astrophys.*, 497(1):145–153, jul 2009. ISSN 0004-6361. doi: 10.1051/0004-6361/200811115.

Dana E Anderson, Edwin A Bergin, Sébastien Maret, and Valentine Wakelam. New Constraints On The Sulfur Reservoir In The Dense Interstellar Medium Provided By Spitzer Observations Of Si In Shocked Gas. *Astrophys. J.*, 779:141–16, 2013. ISSN 0004-637X. doi: 10.1088/0004-637X/779/2/141.

Philippe André, A. Men'shchikov, Sylvain Bontemps, V. Könyves, F. Motte, N. Schneider, Pierre Didelon, V. Minier, P. Saraceno, Derek Ward-Thompson, James Di Francesco, G. White, S. Molinari, L. Testi, A. Abergel, M. Griffin, Th. Henning, P. Royer, B. Merín, R. Vavrek, M. Attard, Doris Arzoumanian, C. D. Wilson, P. Ade, H. Aussel, J.-P. Baluteau, M. Benedettini, Jean-Philippe Bernard, J. a. D. L. Blommaert, L. Cambrésy, P. Cox, A. M. Di Giorgo, P. Hargrave, M. Hennemann, M. Huang, J. Kirk, O. Krause, R. Launhardt, S. Leeks, J. Le Pennec, J. Z. Li, P. G. Martin, A. Maury, G. Olofsson, A. Omont, N. Peretto, S. Pezzuto, T. Prusti, H. Roussel, D. Russeil, M. Sauvage, B. Sibthorpe, A. Sicilia-Aguilar, L. Spinoglio, C. Waelkens, A. Woodcraft, A. Zavagno, and J. Le Pennec. From filamentary clouds to prestellar cores to the stellar IMF: Initial highlights from the Herschel Gould Belt Survey. *Astron. Astrophys.*, 518:L102, jul 2010. ISSN 0004-6361. doi: 10.1051/0004-6361/201014666.

Philippe André, Derek Ward-Thompson, and J. Greaves. Interferometric Identification of a Pre-Brown Dwarf. *Science (80-.).*, 337:69–72, jul 2012. ISSN 0036-8075. doi: 10.1126/science.1222602.

Martin Asplund, Nicolas Grevesse, A. Jacques Sauval, and Pat Scott. The Chemical

Composition of the Sun. *Annu. Rev. Astron. Astrophys.*, 47(1):481–522, sep 2009. ISSN 0066-4146. doi: 10.1146/annurev.astro.46.060407.145222.

Zainab Awad, Serena Viti, Mark P. Collings, and David A. Williams. Warm cores around regions of low-mass star formation. *Mon. Not. R. Astron. Soc.*, 407(4):2511–2518, 2010. ISSN 00358711. doi: 10.1111/j.1365-2966.2010.17077.x.

Patrick Ayotte, R. Scott Smith, K. P. Stevenson, Zdenek Dohnálek, Greg A. Kimmel, and Bruce D. Kay. Effect of porosity on the adsorption, desorption, trapping, and release of volatile gases by amorphous solid water. *J. Geophys. Res. E*, 106(E12):33387–33392, dec 2001. ISSN 01480227. doi: 10.1029/2000JE001362.

R. Bachiller, M. Pérez Gutiérrez, M. S. N. Kumar, and M. Tafalla. Chemically active outflow L 1157. *Astron. Astrophys.*, 372(3):899–912, jun 2001. ISSN 0004-6361. doi: 10.1051/0004-6361:20010519.

Rafael Bachiller and M. Pérez Gutiérrez. Shock Chemistry in the Young Bipolar Outflow L1157. *Astrophys. J.*, 487(1):L93–L96, sep 1997. ISSN 0004637X. doi: 10.1086/310877.

M. Barsony. Class 0 Protostars. In *Clouds, Cores Low Mass Stars*, page 167, 1994.

Matthew R. Bate. Stellar, brown dwarf and multiple star properties from a radiation hydrodynamical simulation of star cluster formation. *Mon. Not. R. Astron. Soc.*, 419 (4):3115–3146, feb 2012. ISSN 00358711. doi: 10.1111/j.1365-2966.2011.19955.x.

A. Belloche, A. A. Meshcheryakov, R. T. Garrod, V. V. Ilyushin, E. A. Alekseev, R. A. Motiyenko, L. Margulès, H. S. P. Müller, and K. M. Menten. Rotational spectroscopy, tentative interstellar detection, and chemical modeling of N-methylformamide. *Astron. Astrophys.*, 601:A49, may 2017. ISSN 0004-6361. doi: 10.1051/0004-6361/201629724.

M. Benedettini, S. Viti, Claudio Codella, R. Bachiller, Fréderic Gueth, M. T. Beltrán, A. Dutrey, and S. Guilloteau. The clumpy structure of the chemically active L1157 outflow. *Mon. Not. R. Astron. Soc.*, 381(3):1127–1136, nov 2007. ISSN 00358711. doi: 10.1111/j.1365-2966.2007.12300.x.

M. Benedettini, G. Busquet, Bertrand Lefloch, Claudio Codella, S. Cabrit, Cecilia Ceccarelli, T. Giannini, B. Nisini, M. Vasta, J. Cernicharo, A. Lorenzani, and A. M. di Giorgio. The CHESS survey of the L1157-B1 shock: the dissociative jet shock as revealed

by HerschelPACS. *Astron. Astrophys.*, 539(A116):L3, mar 2012a. ISSN 0004-6361. doi: 10.1051/0004-6361/201118732.

M. Benedettini, S. Pezzuto, M. G. Burton, S. Viti, S. Molinari, P. Caselli, and L. Testi. Multiline spectral imaging of dense cores in the Lupus molecular cloud. *Mon. Not. R. Astron. Soc.*, 419(1):238–250, jan 2012b. ISSN 00358711. doi: 10.1111/j.1365-2966.2011.19687.x.

M. Benedettini, S. Viti, Claudio Codella, Fréderic Gueth, A. I. Gómez-Ruiz, R. Bachiller, M. T. Beltrán, G. Busquet, Cecilia Ceccarelli, and Bertrand Lefloch. The B1 shock in the L1157 outflow as seen at high spatial resolution. *Mon. Not. R. Astron. Soc.*, 436 (1):179–190, nov 2013. ISSN 00358711. doi: 10.1093/mnras/stt1559.

W. B. Bonnor. Boyle's Law and gravitational instability. *Mon. Not. R. Astron. Soc.*, 116 (3):351, jun 1956. ISSN 0035-8711. doi: 10.1051/0004-6361.

A C A Boogert, W A Schutte, F P Helmich, A G G M Tielens, and D H Wooden. Infrared observations and laboratory simulations of interstellar CH4 and SO2. *Astron. Astrophys.*, 317:929–941, 1997. ISSN 00046361.

Peter N Brown, George D Byrne, and Alan C Hindmarsh. Vode: a Variable-Coeffcient ODE solver. *SIAM J. Sci. Stat. Comput.*, 10(5):1038–1051, 1989. ISSN 0196-5204. doi: 10.1137/0910062.

J. Buchner, a. Georgakakis, K. Nandra, L. Hsu, C. Rangel, M. Brightman, a. Merloni, M. Salvato, J. Donley, and D. Kocevski. X-ray spectral modelling of the AGN obscuring region in the CDFS: Bayesian model selection and catalogue. *Astron. Astrophys.*, 564: A125, apr 2014. ISSN 0004-6361. doi: 10.1051/0004-6361/201322971.

Daren J Burke and Wendy a Brown. Ice in space: surface science investigations of the thermal desorption of model interstellar ices on dust grain analogue surfaces. *Phys. Chem. Chem. Phys.*, 12(23):5947–5969, 2010. ISSN 1463-9076. doi: 10.1039/b917005g.

G. Busquet, Bertrand Lefloch, M. Benedettini, Cecilia Ceccarelli, Claudio Codella, S. Cabrit, B. Nisini, S. Viti, A. I. Gómez-Ruiz, A. Gusdorf, A. M. di Giorgio, and L. Wiesenfeld. The CHESS survey of the L1157-B1 bow-shock: high and low excitation water vapor. *Astron. Astrophys.*, 561:A120, jan 2014. ISSN 0004-6361. doi: 10.1051/0004-6361/201322347.

G Busquet, Francesco Fontani, S Viti, Claudio Codella, Linda Podio, Bertrand Lefloch, M Benedettini, Cecilia Ceccarelli, and G Busquet. The L1157-B1 astrochemical laboratory: testing the origin of DCN. *ArXiv e-prints*, jun 2017. ISSN 14320746. doi: 10.1051/0004-6361/201730422.

S. B. Charnley. Sulfuretted Molecules in Hot Cores. *Astrophys. J.*, 481(1):396–405, may 1997. ISSN 0004-637X. doi: 10.1086/304011.

Claudio Codella, Cecilia Ceccarelli, Bertrand Lefloch, Francesco Fontani, G. Busquet, P. Caselli, C. Kahane, D. Lis, V. Taquet, M. Vasta, S. Viti, and L. Wiesenfeld. Iram Chess Spectral Surveys of the Protostellar Shock L1157-B1: Fossil Deuteration. *Astrophys. J.*, 759(2):L45, sep 2012. ISSN 2041-8205. doi: 10.1088/2041-8205/759/2/L45.

Claudio Codella, S. Viti, Cecilia Ceccarelli, Bertrand Lefloch, M. Benedettini, G. Busquet, P. Caselli, Francesco Fontani, A. Gómez-Ruiz, Linda Podio, and M. Vasta. Broad N2H+ Emission Toward The Protostellar Shock L1157-B1. *Astrophys. J.*, 776(1):52, oct 2013. ISSN 0004-637X. doi: 10.1088/0004-637X/776/1/52.

Mark P. Collings, Mark A. Anderson, Rui Chen, John W. Dever, Serena Viti, David A. Williams, and Martin R S McCoustra. A laboratory survey of the thermal desorption of astrophysically relevant molecules. *Mon. Not. R. Astron. Soc.*, 354(4):1133–1140, 2004. ISSN 00358711. doi: 10.1111/j.1365-2966.2004.08272.x.

Th. de Graauw, F. P. Helmich, T. G. Phillips, J. Stutzki, E. Caux, N. D. Whyborn, P. Dieleman, P. R. Roelfsema, H. Aarts, R. Assendorp, R. Bachiller, W. Baechtold, A. Barcia, D. A. Beintema, V. Belitsky, A. O. Benz, R. Bieber, A. Boogert, C. Borys, B. Bumble, P. Caïs, M. Caris, P. Cerulli-Irelli, G. Chattopadhyay, S. Cherednichenko, M. Ciechanowicz, O. Coeur-Joly, C. Comito, A. Cros, A. de Jonge, G. de Lange, B. Delforges, Y. Delorme, T. den Boggende, J.-M. Desbat, C. Diez-González, A. M. Di Giorgio, L. Dubbeldam, K. Edwards, M. Eggens, N. Erickson, J. Evers, M. Fich, T. Finn, B. Franke, T. Gaier, C. Gal, J. R. Gao, J.-D. Gallego, S. Gauffre, J. J. Gill, S. Glenz, H. Golstein, H. Goulooze, T. Gunsing, R. Güsten, P. Hartogh, W. A. Hatch, R. Higgins, E. C. Honingh, R. Huisman, B. D. Jackson, H. Jacobs, K. Jacobs, C. Jarchow, H. Javadi, W. Jellema, M. Justen, A. Karpov, C. Kasemann, J. Kawamura, G. Keizer, D. Kester, T. M. Klapwijk, Th. Klein, E. Kollberg, J. Kooi, P.-P. Kooiman, B. Kopf, M. Krause, J.-M. Krieg, C. Kramer, B. Kruizenga, T. Kuhn, W. Laauwen, R. Lai, B. Larsson, H. G.

Leduc, C. Leinz, R. H. Lin, R. Liseau, G. S. Liu, A. Loose, I. López-Fernandez, S. Lord, W. Luinge, A. Marston, J. Martín-Pintado, A. Maestrini, F. W. Maiwald, C. McCoey, I. Mehdi, A. Megej, M. Melchior, L. Meinsma, H. Merkel, M. Michalska, C. Monstein, D. Moratschke, P. Morris, H. Muller, J. A. Murphy, A. Naber, E. Natale, W. Nowosielski, F. Nuzzolo, M. Olberg, M. Olbrich, R. Orfei, P. Orleanski, V. Ossenkopf, T. Peacock, J. C. Pearson, I. Peron, S. Phillip-May, L. Piazzo, P. Planesas, M. Rataj, L. Ravera, C. Risacher, M. Salez, L. A. Samoska, P. Saraceno, R. Schieder, E. Schlecht, F. Schlöder, F. Schmülling, M. Schultz, K. Schuster, O. Siebertz, H. Smit, R. Szczerba, R. Shipman, E. Steinmetz, J. A. Stern, M. Stokroos, R. Teipen, D. Teyssier, T. Tils, N. Trappe, C. van Baaren, B.-J. van Leeuwen, H. van de Stadt, H. Visser, K. J. Wildeman, C. K. Wafelbakker, J. S. Ward, P. Wesselius, W. Wild, S. Wulff, H.-J. Wunsch, X. Tielens, P. Zaal, H. Zirath, J. Zmuidzinas, and F. Zwart. The Herschel-Heterodyne Instrument for the Far-Infrared (HIFI). *Astron. Astrophys.*, 518:L6, jul 2010. ISSN 0004-6361. doi: 10.1051/0004-6361/201014698.

Turlough P. Downes and Sylvie Cabrit. Jet-accelerated molecular outflows: The mass-velocity and intensity-velocity relations. *Rev. Mex. Astron. y Astrofis. Ser. Conf.*, 15 (1):120–122, may 2003. ISSN 14052059. doi: 10.1051/0004-6361:20030363.

Bruce T. Draine. Photoelectric Heating of Interstellar Gas. *Astrophys. J. Suppl. Ser.*, 36: 595–619, 1978. ISSN 0067-0049. doi: 10.1086/190513.

Bruce T. Draine. Interstellar shock waves with magnetic precursors. *Astrophys. J.*, 241 (1):1021, nov 1980. ISSN 0004-637X. doi: 10.1086/158416.

Bruce T. Draine. *The physics of the insterstellar and intergalactic medium.* 2011. ISBN 9780691122137.

Bruce T. Draine, W. G. Roberge, and A Dalgarno. Magnetohydrodynamic shock waves in molecular clouds. *Astrophys. J.*, 264:485, jan 1983. ISSN 0004-637X. doi: 10.1086/160617.

W. W. Duley and D. A. Williams. The formation of interstellar H2 on amorphous silicate grains. *Mon. Not. R. Astron. Soc.*, 223(1):177–182, nov 1986. ISSN 13652966. doi: 10.1093/mnras/223.1.177.

John Edward Dyson and David Arnold Williams. Physics of the interstellar medium, 1980.

Bruce G Elmegreen and John Scalo. INTERSTELLAR TURBULENCE I: Observations and Processes. *Annu. Rev. Astron. Astrophys*, 42:211–73, 2004. ISSN 0066-4146. doi: 10.1146/annurev.astro.41.011802.094859.

Melissa L Enoch, Jeong-Eun Lee, Paul Harvey, Michael M Dunham, and Scott Schnee. A CANDIDATE DETECTION OF THE FIRST HYDROSTATIC CORE. *Astrophys. J. Lett.*, 722:33–38, 2010. doi: 10.1088/2041-8205/722/1/L33.

D. R. Flower and G. Pineau des Forêts. The influence of grains on the propagation and structure of C-type shock waves in interstellar molecular clouds. *Mon. Not. R. Astron. Soc.*, 343(2):390–400, aug 2003. ISSN 0035-8711. doi: 10.1046/j.1365-8711.2003.06716.x.

D. R. Flower and G. Pineau des Forêts. Time-dependent modelling of the molecular line emission from shock waves in outflow sources. *Mon. Not. R. Astron. Soc.*, 421(4): 2786–2797, 2012. ISSN 00358711. doi: 10.1111/j.1365-2966.2012.20481.x.

D. R. Flower and G. Pineau des Forêts. Interpreting observations of molecular outflow sources: the MHD shock code mhd_vode. *Astron. Astrophys.*, 578:A63, jun 2015. ISSN 0004-6361. doi: 10.1051/0004-6361/201525740.

Francesco Fontani, Claudio Codella, Cecilia Ceccarelli, Bertrand Lefloch, S. Viti, and M. Benedettini. the L1157-B1 Astrochemical Laboratory: Measuring the True Formaldehyde Deuteration on Grain Mantles. *Astrophys. J.*, 788(2):L43, jun 2014. ISSN 2041-8205. doi: 10.1088/2041-8205/788/2/L43.

M. Garozzo, D. Fulvio, Z. Kanuchova, M. E. Palumbo, and G. Strazzulla. The fate of S-bearing species after ion irradiation of interstellar icy grain mantles. *Astron. Astrophys.*, 509:A67, jan 2010. ISSN 0004-6361. doi: 10.1051/0004-6361/200913040.

T. R. Geballe, F. Baas, J. M. Greenberg, and W. Schutte. New infrared absorption features due to solid phase molecules containing sulfur in W 33A. *Astron. Astrophys.*, 146:L6–L8, 1985.

Marla Geha, Thomas M. Brown, Jason Tumlinson, Jason S. Kalirai, Joshua D. Simon, Evan N. Kirby, Don A. VandenBerg, Ricardo R. Muñoz, Roberto J. Avila, Puragra Guhathakurta, and Henry C. Ferguson. the Stellar Initial Mass Function of Ultra-Faint Dwarf Galaxies: Evidence for Imf Variations With Galactic Environment. *Astrophys. J.*, 771(1):29, 2013. ISSN 0004-637X. doi: 10.1088/0004-637X/771/1/29.

E. L. Gibb, D. C. B. Whittet, W. a. Schutte, a. C. a. Boogert, J. E. Chiar, P. Ehrenfreund, P. a. Gerakines, J. V. Keane, a. G. G. M. Tielens, E. F. van Dishoeck, and O. Kerkhof. An Inventory of Interstellar Ices toward the Embedded Protostar W33A. *Astrophys. J.*, 536(1):347–356, jun 2000. ISSN 0004-637X. doi: 10.1086/308940.

P.F. Goldsmith and W.D. Langer. Population Diagram Analysis of Molecular Line Emission. *Astrophys. J.*, 517(1979):209–225, may 1999. ISSN 0004-637X. doi: 10.1086/307195.

A. I. Gómez-Ruiz, Claudio Codella, Bertrand Lefloch, M. Benedettini, G. Busquet, Cecilia Ceccarelli, B. Nisini, Linda Podio, and S. Viti. The density structure of the L1157 molecular outflow. *Mon. Not. R. Astron. Soc.*, 446(4):3346–3355, dec 2015. ISSN 13652966. doi: 10.1093/mnras/stu2311.

A. I. Gómez-Ruiz, Claudio Codella, Serena Viti, Izaskun Jiménez-Serra, G. Navarra, Rafael Bachiller, Paola Caselli, A. Fuente, A. Gusdorf, Bertrand Lefloch, A. Lorenzani, and B. Nisini. Diagnosing shock temperature with NH 3 and H 2 O profiles. *Mon. Not. R. Astron. Soc.*, 462(2):2203–2217, oct 2016. ISSN 0035-8711. doi: 10.1093/mnras/stw1811.

A. Greve, C. Kramer, and W. Wild. The beam pattern of the IRAM 30-m telescope. *Astron. Astrophys. Suppl. Ser.*, 133(2):271–284, 1998. ISSN 0365-0138. doi: 10.1051/aas:1998454.

C Gry, F Boulanger, C Nehmé, G des Forêts, E Habart, and E Falgarone. H_2 formation and excitation in the diffuse interstellar medium. *Aap*, 391(2):675–680, aug 2002. ISSN 0004-6361. doi: 10.1051/0004-6361:20020691.

Fréderic Gueth, S Guilloteau, and R. Bachiller. A precessing jet in the L 1157 molecular outflow. *Astron. Astrophys.*, 307:891–897, mar 1996. ISSN 00046361.

Fréderic Gueth, S Guilloteau, A Dutrey, and R Bachiller. Structure and kinematics of a protostar: mm-interferometry of L 1157. *Astron. Astrophys.*, 323:943–952, jul 1997. ISSN 00046361.

Fréderic Gueth, S Guilloteau, and R Bachiller. SiO shocks in the L1157 molecular outflow. *Astron. Astrophys.*, 333(333):287–297, 1998.

V. Guillet, G. Pineau des Forêts, and A. P. Jones. Shocks in dense clouds: III. Dust processing and feedback effects in C-type shocks. *Astron. Astrophys.*, 527:A123, 2011. ISSN 0004-6361. doi: 10.1051/0004-6361/201015973.

A. Gusdorf, S. Cabrit, D. R. Flower, and G. Pineau des Forêts. SiO line emission from C-type shock waves: interstellar jets and outflows. *Astron. Astrophys.*, 482(3):809–829, 2008. ISSN 0004-6361. doi: 10.1051/0004-6361:20078900.

a. Hacar, M. Tafalla, J. Kauffmann, and a. Kovacs. Cores, filaments, and bundles: hierarchical core formation in the L1495/B213 Taurus region. *Astron. Astrophys.*, 554:A55, jun 2013. ISSN 0004-6361. doi: 10.1051/0004-6361/201220090.

J. Hatchell, M. A. Thompson, T. J. Millar, and G. H. Macdonald. Sulphur Chemistry and Evolution in Hot Cores. *Astron. Astrophys.*, 338:713–722, 1998. ISSN 00046361.

J. Hatchell, G. A. Fuller, and J. S. Richer. Star formation in Perseus. *Astron. Astrophys.*, 472(1):187–198, sep 2007. ISSN 0004-6361. doi: 10.1051/0004-6361:20066467.

Patrick Hennebelle and Gilles Chabrier. Analytical theory for the initial mass function: CO clumps and prestellar cores. *Astrophys. J.*, 684(1):395–410, sep 2008. ISSN 0004-637X. doi: 10.1086/589916.

Thomas Henning. Cosmic Silicates. *Annu. Rev. Astron. Astrophys*, 48:21–46, 2010. doi: 10.1146/annurev-astro-081309-130815.

Eric Herbst and Ewine F. van Dishoeck. Complex Organic Interstellar Molecules. *Annu. Rev. Astron. Astrophys.*, 47:427–480, 2009. ISSN 0066-4146. doi: 10.1146/annurev-astro-082708-101654.

J.˜J. Hester, P.˜A. Scowen, R Sankrit, T.˜R. Lauer, E.˜A. Ajhar, W.˜A. Baum, A Code, D.˜G. Currie, G.˜E. Danielson, S.˜P. Ewald, S.˜M. Faber, C.˜J. Grillmair, E.˜J. Groth, J.˜A. Holtzman, D.˜A. Hunter, J Kristian, R.˜M. Light, C.˜R. Lynds, D.˜G. Monet, E.˜J. O'Neil Jr., E.˜J. Shaya, P.˜K. Seidelmann, and J.˜A. Westphal. Hubble Space Telescope WFPC2 Imaging of M16: Photoevaporation and Emerging Young Stellar Objects. *aj*, 111:2349, jun 1996.

Jonathan Holdship and Serena Viti. Chemical tracers of pre-brown dwarf cores formed through turbulent fragmentation. *Mon. Not. R. Astron. Soc.*, 455(3):2371–2376, nov 2016. ISSN 13652966. doi: 10.1093/mnras/stv2460.

Jonathan Holdship, Serena Viti, Izaskun Jiménez-Serra, Bertrand Lefloch, Claudio Codella, Linda Podio, Milena Benedettini, Francesco Fontani, Rafael Bachiller, Mario Tafalla, and Cecilia Ceccarelli. H2S in the L1157-B1 Bow shock. *Mon. Not. R. Astron. Soc.*, 10(June):10, aug 2016. doi: 10.1093/mnras/stw1977.

Jonathan Holdship, Serena Viti, Izaskun Jiménez-Serra, Antonios Makrymallis, and Felix Priestley. UCLCHEM: A Gas-Grain Chemical Code. *Astron. J.*, 154(1):38, jul 2017. ISSN 1538-3881. doi: 10.3847/1538-3881/aa773f.

S. Ioppolo, H. M. Cuppen, C. Romanzin, E. F. van Dishoeck, and H. Linnartz. Laboratory evidence for efficient water formation in interstellar ices. *Astrophys. J.*, 686(2):1474, oct 2008. ISSN 0004-637X. doi: 10.1086/591506.

Izaskun Jiménez-Serra, P. Caselli, J. Martín-Pintado, and T.W. Hartquist. Parametrization of C-shocks. Evolution of the sputtering of grains. *Astron. Astrophys.*, 482(2): 549–559, 2008. ISSN 0004-6361. doi: 10.1051/0004-6361:20078054.

M. Jura. Interstellar clouds containing optically thin H2. *Astrophys. J.*, 197:575, may 1975. ISSN 0004-637X. doi: 10.1086/153545.

J. Kauffmann, F. Bertoldi, and N. J. Evans. Spitzer discovery of very low luminosity objects. *Astron. Nachrichten*, 326(10):878–881, dec 2005. ISSN 00046337. doi: 10.1002/asna.200510446.

J. Kauffmann, F. Bertoldi, T. L. Bourke, P. C. Myers, C. W. Lee, and T. L. Huard. Confirmation of the VeLLO L1148-IRS: Star formation at very low (column) density. *Mon. Not. R. Astron. Soc.*, 416(3):2341–2358, 2011. ISSN 00358711. doi: 10.1111/j.1365-2966.2011.19205.x.

Michael J. Kaufman and David A. Neufeld. Far-Infrared Water Emission from Magnetohydrodynamic Shock Waves. *Astrophys. J.*, 456:611, jan 1996. ISSN 0004-637X. doi: 10.1086/176683.

V. Konyves, Philippe André, A. Men'shchikov, P. Palmeirim, D. Arzoumanian, N. Schneider, A. Roy, P. Didelon, A. Maury, Y. Shimajiri, J. Di Francesco, S. Bontemps, N. Peretto, M. Benedettini, J. Ph. Bernard, D. Elia, M. J. Griffin, T. Hill, J. Kirk, B. Ladjelate, K. Marsh, P. G. Martin, F. Motte, Q. Nguyen Luong, S. Pezzuto, H. Roussel, K. L. J. Rygl, S. I. Sadavoy, E. Schisano, L. Spinoglio, Derek Ward-Thompson, and

G. J. White. A census of dense cores in the Aquila cloud complex: SPIRE/PACS observations from the Herschel Gould Belt survey. *Astron. Astrophys.*, 91:1–35, dec 2015. ISSN 14320746. doi: 10.1051/0004-6361/201525861.

J D Kraus. Radio Astronomy,(; Powell: Cygnus-Quasar), 1982.

C. J. Lada. Star formation: from OB associations to protostars. In *IAU Symp.*, volume 115, page 1, 1987.

R. B. Larson. Numerical Calculations of the Dynamics of a Collapsing Proto-Star*. *Mon. Not. R. Astron. Soc.*, 145(3):271–295, aug 1969. ISSN 0035-8711. doi: 10.1093/mnras/145.3.271.

Jacques Le Bourlot, G. Pineau des Forêts, D. R. Flower, and S. Cabrit. New determinations of the critical velocities of C-type shock waves in dense molecular clouds: Application to the outflow source in Orion. *Mon. Not. R. Astron. Soc.*, 332(4):985–993, jun 2002. ISSN 00358711. doi: 10.1046/j.1365-8711.2002.05373.x.

Bertrand Lefloch, S. Cabrit, Claudio Codella, G. Melnick, J. Cernicharo, E. Caux, Milena Benedettini, A. Boogert, Paola Caselli, Cecilia Ceccarelli, Fréderic Gueth, A. Lorenzani, D. Neufeld, B. Nisini, S. Pacheco, L. Pagani, J. R. Pardo, B. Parise, M. Salez, K. Schuster, Serena Viti, A. Bacmann, A. Baudry, T. A. Bell, E.˜A. A. Bergin, G. Blake, S. Bottinelli, A. Castets, C. Comito, A. Coutens, N. Crimier, C. Dominik, K. Demyk, P. Encrenaz, E. Falgarone, A. Fuente, M. Gerin, P. Goldsmith, F. Helmich, Patrick Hennebelle, Th. Henning, Eric Herbst, T. Jacq, C. Kahane, M. Kama, A. Klotz, W. Langer, D. Lis, S. Lord, Sébastien Maret, J C Pearson, T. Phillips, P. Saraceno, P. Schilke, X. Tielens, Van Der Tak F, Van Der Wiel M, C. Vastel, V. Wakelam, A. Walters, F. Wyrowski, H. Yorke, Rafael Bachiller, C. Borys, De Lange G, Y. Delorme, Carsten Kramer, B. Larsson, R. Lai, F.˜W. W. Maiwald, I. Mehdi, V. Ossenkopf, P. Siegel, J. Stutzki, J.˜H. H. Wunsch, P. Hily-Blant, F. F. S. van der Tak, M. van der Wiel, G. de Lange, and J. Martin-Pintado. Special feature L etter to the E ditor The CHESS spectral survey of star forming regions : Peering into the protostellar shock L1157-B1. *Astron. Astrophys.*, 518:4–8, 2010. ISSN 0004-6361. doi: 10.1051/0004-6361/201014630.

Bertrand Lefloch, S Cabrit, G Busquet, Claudio Codella, Cecilia Ceccarelli, J Cernicharo, J R Pardo, M Benedettini, D C Lis, and B Nisini. the Chess Survey of the L1157-B1

Shock Region: Co Spectral Signatures of Jet-Driven Bow Shocks. *Astrophys. J. Lett.*, 757:25–5, oct 2012. ISSN 2041-8205. doi: 10.1088/2041-8205/757/2/L25.

Bertrand Lefloch, C. Vastel, S. Viti, Izaskun Jiménez-Serra, Claudio Codella, Linda Podio, Cecilia Ceccarelli, E. Mendoza, J. R.D. Lepine, and R. Bachiller. Phosphorus-bearing molecules in solar-type star-forming regions: First PO detection. *Mon. Not. R. Astron. Soc.*, 462(4):3937–3944, nov 2016. ISSN 13652966. doi: 10.1093/mnras/stw1918.

Tie Liu, Yuefang Wu, and Huawei Zhang. GASEOUS CO ABUNDANCEAN EVOLUTIONARY TRACER FOR MOLECULAR CLOUDS. *Astrophys. J. Lett.*, 775(8pp), 2013. doi: 10.1088/2041-8205/775/1/L2.

Jean Christophe Loison, Philippe Halvick, Astrid Bergeat, Kevin M. Hickson, and Valentine Wakelam. Review of OCS gas-phase reactions in dark cloud chemical models. *Mon. Not. R. Astron. Soc.*, 421(2):1476–1484, apr 2012. ISSN 00358711. doi: 10.1111/j.1365-2966.2012.20412.x.

O. Lomax, A. P. Whitworth, and D. A. Hubber. Forming isolated brown dwarfs by turbulent fragmentation. *Mon. Not. R. Astron. Soc.*, 458(2):1242–1252, 2016. ISSN 13652966. doi: 10.1093/mnras/stw406.

M. Lombardi, J. Alves, and C. J. Lada. 2MASS wide field extinction maps. *Astron. Astrophys.*, 535(3):A16, aug 2006. ISSN 0004-6361. doi: 10.1051/0004-6361/201116915.

L W Looney, John J Tobin, and W Kwon. A Flattened Protostellar Envelope in Absorption around L1157. *Astrophys. J. Lett.*, 670(2):L131–L134, dec 2007. ISSN 0004-637X. doi: 10.1086/524361;.

Beverly T. Lynds. Catalogue of Dark Nebulae. *Astrophys. J. Suppl. Ser.*, 7:1, may 1962. doi: 10.1086/190072.

Sébastien Maret and Edwin A. Bergin. Astrochem: Abundances of chemical species in the interstellar medium. *Astrophys. Source Code Libr. Rec. ascl1507.010*, 2015.

Tomoaki Matsumoto, Kazuhito Dobashi, and Tomomi Shimoikura. Star Formation in Turbulent Molecular Clouds With Colliding Flow. *Astrophys. J.*, 801(2):77, dec 2015. ISSN 1538-4357. doi: 10.1088/0004-637X/801/2/77.

Yuko Matsushita, Masahiro N. Machida, Yuya Sakurai, and Takashi Hosokawa. Massive Outflows Driven by Magnetic Effects in Star Forming Clouds with High Mass Accretion Rates. *arXiv Prepr.*, 000(April):1026–1049, sep 2017. ISSN 13652966. doi: 10.1093/mnras/stx893.

P. W. May, G. Pineau des Forêts, D. R. Flower, D. Field, N. L. Allan, and J. A. Purton. Sputtering of grains in C-type shocks. *Mon. Not. R. Astron. Soc.*, 318(3):809–816, 2000. ISSN 00358711. doi: 10.1046/j.1365-8711.2000.03796.x.

Christopher F. McKee. Photoionization-regulated star formation and the structure of molecular clouds. *Astrophys. J.*, 345:782–801, 1989. ISSN 0004-637X. doi: 10.1086/167950.

Paul W Merrill, Roscoe F Sanford, O C Wilson, and Cora G Burwell. INTENSITIES AND DISPLACEMENTS OF INTERSTELLAR LINES*. *Astrophys. J.*, 86:274, 1937.

T J Millar, P R A Farquhar, and K Willacy. The UMIST database for astrochemistry 1995. *Ser. Astron. Astrophys. Suppl. Ser*, 139(121):139–185, jan 1997. ISSN 0004-6361. doi: 10.1051/0004-6361:20064981.

Telemachos Ch. Mouschovias and Lyman Spitzer. NOTE ON THE COLLAPSE OF MAGNETIC INTERSTELLAR CLOUDS. *Astrophys. J.*, 210:326–327, 1976.

Philip C. Myers. Filamentary Condensations in a Young Cluster. *Astrophys. J.*, 735(2):82, jul 2011. ISSN 0004-637X. doi: 10.1088/0004-637X/735/2/82.

A. Occhiogrosso, A. Vasyunin, Eric Herbst, S. Viti, M. D. Ward, S. D. Price, and W. A. Brown. Ethylene oxide and acetaldehyde in hot cores. *Astron. Astrophys.*, 564(2011):A123, 2014. ISSN 0004-6361. doi: 10.1051/0004-6361/201322598.

Stella S. R. Offner and Héctor G. Arce. Investigations of Protostellar Outflow Launching and Gas Entrainment: Hydrodynamic Simulations and Molecular Emission. *Astrophys. J.*, 784(1):61, 2014. ISSN 0004-637X. doi: 10.1088/0004-637X/784/1/61.

Stephan Ott, Herschel Science Centre, and European Space Agency. The Herschel Data Processing System - HIPE and Pipelines - Up and Running Since the Start of the Mission. In Y Mizumoto, K.-I. Morita, and M Ohishi, editors, *arXiv Prepr. arXiv1011.1209*, volume 434 of *Astronomical Society of the Pacific Conference Series*, pages 139–142, dec 2010.

Paolo Padoan and AAke Nordlund. The "Mysterious" Origin of Brown Dwarfs. *Astrophys. J.*, 617(2002):6, dec 2004. ISSN 0004-637X. doi: 10.1086/345413.

Paolo Padoan and Åke Nordlund. The Stellar Initial Mass Function from Turbulent Fragmentation. *Astrophys. J.*, 576(2):870–879, sep 2002. ISSN 0004-637X. doi: 10.1086/341790.

Aina Palau, Luis A. Zapata, Luis F. Rodríguez, Hervé Bouy, David Barrado, María Morales-Calderón, Philip C. Myers, Nicholas Chapman, Carmen Juárez, and Di Li. IC 348-SMM2E: A Class 0 proto-brown dwarf candidate forming as a scaled-down version of low-mass stars. *Mon. Not. R. Astron. Soc.*, 444(1):833–845, oct 2014. ISSN 13652966. doi: 10.1093/mnras/stu1461.

M. E. Palumbo, A. G. G. M. Tielens, and A. T. Tokunaga. Solid Carbonyl Sulphide (OCS) in W33A. *Astrophys. J.*, 449:674–680, aug 1995. ISSN 0004-637X. doi: 10.1086/176088.

M E P Palumbo, T. R. Geballe, and Alexander G G M Tielens. Solid Carbonyl Sulfide (OCS) in Dense Molecular Clouds. *Astrophys. J.*, 479(2):839–844, apr 1997. ISSN 0004-637X. doi: 10.1086/303905.

H M Pickett. Submillimeter, millimeter, and microwave spectral line catalog. *Appl. Opt.*, 24(14):2235, 1985. ISSN 0003-6935. doi: 10.1364/AO.24.002235.

G. L. Pilbratt, J. R. Riedinger, T. Passvogel, G. Crone, D. Doyle, U. Gageur, a. M. Heras, C. Jewell, L. Metcalfe, S. Ott, and M. Schmidt. Herschel Space Observatory. *Astron. Astrophys.*, 518:L1, jul 2010. ISSN 0004-6361. doi: 10.1051/0004-6361/201014759.

Linda Podio, Bertrand Lefloch, Cecilia Ceccarelli, Claudio Codella, and R. Bachiller. Molecular ions in the protostellar shock L1157-B1. *Astron. Astrophys.*, 565:A64, may 2014. ISSN 0004-6361. doi: 10.1051/0004-6361/201322928.

Linda Podio, Claudio Codella, Fréderic Gueth, S. Cabrit, R. Bachiller, A. Gusdorf, C. F. Lee, Bertrand Lefloch, S. Leurini, B. Nisini, and Mario Tafalla. The jet and the disk of the HH 212 low-mass protostar imaged by ALMA: SO and SO 2 emission. *Astron. Astrophys.*, 581:A85, sep 2015. ISSN 0004-6361. doi: 10.1051/0004-6361/201525778.

Linda Podio, Claudio Codella, Fréderic Gueth, S. Cabrit, A. Maury, B. Tabone, C. Lefèvre, S. Anderl, Philippe André, A. Belloche, S. Bontemps, P. Hennebelle, Bertrand Lefloch,

Sébastien Maret, and L. Testi. First image of the L1157 molecular jet by the CALYPSO IRAM-PdBI survey. *Astron. Astrophys.*, 4(ii):1–5, sep 2016. ISSN 14320746. doi: 10.1051/0004-6361/201628876.

Linda Podio, Claudio Codella, Bertrand Lefloch, N. Balucani, Cecilia Ceccarelli, R. Bachiller, M. Benedettini, J. Cernicharo, N. Faginas-Lago, Francesco Fontani, A. Gusdorf, and M. Rosi. Silicon-bearing molecules in the shock L1157-B1: first detection of SiS around a Sun-like protostar. *MNRAS*, 6(May):1–6, 2017. ISSN 1745-3925. doi: 10.1093/mnrasl/slx068.

Jonathan Rawlings, T.W. Hartquist, K.˜M. Menten, and J. M. C. Williams, D.˜A. Direct diagnosis of infall in collapsing protostars. *Mon. Not. R. Astron. Soc.*, 255:471–485, 1992.

Rafael Rebolo, Maria Rosa Zapatero Osorio, and Eduardo Martín. Discovery of a brown dwarf in the Pleiades star cluster. *Nature*, 377:129–131, sep 1995. ISSN 0028-0836. doi: 10.1038/377129a0.

B Reipurth and C Clarke. The Formation of Brown Dwarfs as Ejected Stellar Embryos. *Astron. J.*, 122(1999):432, jul 2001. ISSN 00046256. doi: 10.1086/321121.

Megan Reiter, Megan M. Kiminki, Nathan Smith, and John Bally. Proper motions of collimated jets from intermediate-mass protostars in the Carina Nebula. *Mon. Not. R. Astron. Soc.*, 470(4):4671–4697, oct 2017. ISSN 0035-8711. doi: 10.1093/mnras/stx1489.

L. Ricci, L. Testi, A. Natta, A. Scholz, I. de Gregorio-Monsalvo, and A. Isella. Brown Dwarf Disks With Alma. *Astrophys. J.*, 791(1):20, aug 2014. ISSN 0004-637X. doi: 10.1088/0004-637X/791/1/20.

W. K M Rice, P. J. Armitage, I. A. Bonnell, M. R. Bate, S. V. Jeffers, and S. G. Vine. Substellar companions and isolated planetary-mass objects from protostellar disc fragmentation. *Mon. Not. R. Astron. Soc.*, 346(3):L36–L40, dec 2003. ISSN 00358711. doi: 10.1111/j.1365-2966.2003.07317.x.

J. F. Roberts, Jonathan Rawlings, S. Viti, and D. A. Williams. Desorption from interstellar ices. *Mon. Not. R. Astron. Soc.*, 382(2):733–742, dec 2007. ISSN 00358711. doi: 10.1111/j.1365-2966.2007.12402.x.

J F Roberts, I Jiménez-Serra, J Martín-Pintado, S Viti, A Rodríguez-Franco, A Faure, and J Tennyson. The magnetic precursor of L1448-mm: excitation differences between ion and neutral fluids. *A&A*, 513, 2010. doi: 10.1051/0004-6361/200913086.

P R Roelfsema, F P Helmich, D Teyssier, V Ossenkopf, P Morris, Michael Olberg, R Shipman, C Risacher, M Akyilmaz, and R. Assendorp. In-orbit performance of Herschel-HIFI. *Astron. Astrophys.*, 537:A17, 2012.

M Röllig, N P Abel, T Bell, F Bensch, J Black, G J Ferland, B Jonkheid, I Kamp, M J Kaufman, Jacques Le Bourlot, F Le Petit, R Meijerink, O Morata, V Ossenkopf, E Roueff, G Shaw, M Spaans, A Sternberg, J Stutzki, W F Thi, E F van Dishoeck, P A M van Hoof, S Viti, and M G Wolfire. A photon dominated region code comparison study. *Astron. Astrophys. (ISSN 0004-6361)*, 467(1):187–206, 2007. ISSN 0004-6361. doi: 10.1051/0004-6361:20065918.

K J R Rosman and P D P Taylor. Isotopic compositions of the elements 1997 (Technical Report). *Pure Appl. Chem.*, 70(1):217–235, 1998. ISSN 0033-4545. doi: 10.1351/pac199870010217.

B D Savage and John S Mathis. Observed Properties of Interstellar Dust. *Annu. Rev. Astron. Astrophys.*, 17(1):73–111, 1979. ISSN 0066-4146. doi: 10.1146/annurev.aa.17.090179.000445.

M. Schmalzl, R. Visser, C. Walsh, T. Albertsson, E. F. van Dishoeck, L. E. Kristensen, and J. C. Mottram. Water in low-mass star-forming regions with Herschel. *Astron. Astrophys.*, 572:A81, 2014. ISSN 0004-6361. doi: 10.1051/0004-6361/201424236.

N. Schneider, T. Csengeri, M. Hennemann, F. Motte, P. Didelon, C. Federrath, S. Bontemps, J. Di Francesco, D. Arzoumanian, V. Minier, Philippe André, T. Hill, A. Zavagno, Q. Nguyen-Luong, M. Attard, J. Ph. Bernard, D. Elia, C. Fallscheer, M. Griffin, J. Kirk, R. S. Klessen, V. Könyves, P. Martin, A. Men'shchikov, P. Palmeirim, N. Peretto, M. Pestalozzi, D. Russeil, S. Sadavoy, T. Sousbie, L. Testi, P. Tremblin, Derek Ward-Thompson, and G. White. Cluster-formation in the Rosette molecular cloud at the junctions of filaments. *Astron. Astrophys.*, 540:L11, apr 2012. ISSN 0004-6361. doi: 10.1051/0004-6361/201118566.

F. L. Schöier, F. F. S. van der Tak, E. F. van Dishoeck, and J. H. Black. An atomic and

molecular database for analysis of submillimetre line observations. *Astron. Astrophys.*, 432(1):369–379, mar 2005. ISSN 0004-6361. doi: 10.1051/0004-6361:20041729.

Young Min Seo, Yancy L. Shirley, Paul Goldsmith, Derek Ward-Thompson, Jason M. Kirk, Markus Schmalzl, Jeong-Eun Lee, Rachel Friesen, Glen Langston, Joe Masters, and Robert W. Garwood. an Ammonia Spectral Map of the L1495-B218 Filaments in the Taurus Molecular Cloud. I. Physical Properties of Filaments and Dense Cores. *Astrophys. J.*, 805(2):185, mar 2015. ISSN 1538-4357. doi: 10.1088/0004-637X/805/2/185.

Lyman Spitzer and Thomas T. Arny. Physical Processes in the Interstellar Medium. *Am. J. Phys.*, 46(11):1201–1201, nov 1978. ISSN 0002-9505. doi: 10.1119/1.11466.

A. N. Suutarinen, L. E. Kristensen, J. C. Mottram, H. J. Fraser, and E. F. Van Dishoeck. Water and methanol in low-mass protostellar outflows: Gas-phase synthesis, ice sputtering and destruction. *Mon. Not. R. Astron. Soc.*, 440(2):1844–1855, apr 2014. ISSN 13652966. doi: 10.1093/mnras/stu406.

M. Tafalla, Y. N. Su, H. Shang, D. Johnstone, Q. Zhang, J. Santiago-Garcia, C. F. Lee, N. Hirano, and L. Y. Wang. Anatomy of the internal bow shocks in the IRAS 04166+2706 protostellar jet. (29493):12, oct 2016. ISSN 14320746. doi: 10.1051/0004-6361/201629493.

Mario Tafalla and Rafael Bachiller. Ammonia emission from bow shocks in the L1157 outflow. *Astrophys. J.*, 443:L37, apr 1995. ISSN 0004-637X. doi: 10.1086/187830.

Kohji Tomisaka. Collapse of Rotating Magnetized Molecular Cloud Cores and Mass Outflows. *ApJS*, 575(Tomisaka 1998):306–326, aug 2002. ISSN 0004-637X. doi: 10.1086/341133.

T Umemoto, T Iwata, Y Fukui, H Mikami, S Yamamoto, O Kameya, and N Hirano. The outflow in the L1157 dark cloud - Evidence for shock heating of the interacting gas. *Astrophys. J.*, 392:L83, jun 1992. ISSN 0004-637X. doi: 10.1086/186431.

F. F. S. van der Tak, J.˜H. H. Black, F.˜L. L. Schöier, D.˜J. J. Jansen, and Ewine F. van Dishoeck. A computer program for fast non-LTE analysis of interstellar line spectra. *Astron. Astrophys.*, 468(2):627–635, jun 2007. ISSN 0004-6361. doi: 10.1051/0004-6361:20066820.

Ewine F. van Dishoeck and Geoffrey A. Blake. Chemical Evolution of Star-Forming Regions. *Annu. Rev. Astron. Astrophys.*, 36(1):317–368, sep 1998. ISSN 0066-4146. doi: 10.1146/annurev.astro.36.1.317.

S. Van Loo, I. Ashmore, P. Caselli, S. A E G Falle, and T.W. Hartquist. Time-dependent simulations of steady C-type shocks. *Mon. Not. R. Astron. Soc.*, 395(1):319–327, may 2009. ISSN 00358711. doi: 10.1111/j.1365-2966.2009.14515.x.

S. Van Loo, I. Ashmore, P. Caselli, S. A.E.G. Falle, and T.W. Hartquist. Sputtering in oblique C-type shocks. *Mon. Not. R. Astron. Soc.*, 428(1):381–388, oct 2013. ISSN 00358711. doi: 10.1093/mnras/sts030.

Gianfranco Vidali. H2 formation on interstellar grains. *Chem. Rev.*, 113(12):8762–8782, 2013. ISSN 00092665. doi: 10.1021/cr400156b.

S. Viti, E. Roueff, T.W. Hartquist, G. Pineau des Forts, and D. A. Williams. Interstellar oxygen chemistry. *Astron. Astrophys.*, 370(2):557–569, may 2001. ISSN 0004-6361. doi: 10.1051/0004-6361:20010246.

S. Viti, Izaskun Jiménez-Serra, J. A. Yates, Claudio Codella, M. Vasta, P. Caselli, Bertrand Lefloch, and Cecilia Ceccarelli. L1157-B1: Water and Ammonia As Diagnostics of Shock Temperature. *Astrophys. J.*, 740(1):L3, 2011. ISSN 2041-8205. doi: 10.1088/2041-8205/740/1/L3.

Serena Viti and Da Williams. Time-dependent evaporation of icy mantles in hot cores. *Mon. Not. R. Astron. Soc.*, 305(4):755–762, 1999. ISSN 0035-8711. doi: 10.1046/j.1365-8711.1999.02447.x.

Serena Viti, Mark P. Collings, John W. Dever, Martin R S McCoustra, and David A. Williams. Evaporation of ices near massive stars: Models based on laboratory temperature programmed desorption data. *Mon. Not. R. Astron. Soc.*, 354(4):1141–1145, 2004. ISSN 00358711. doi: 10.1111/j.1365-2966.2004.08273.x.

V. Wakelam, P. Caselli, Cecilia Ceccarelli, Eric Herbst, and A. Castets. Resetting chemical clocks of hot cores based on S-bearing molecules. *Astron. Astrophys.*, 422(1):159–169, jul 2004. ISSN 0004-6361. doi: 10.1051/0004-6361:20047186.

V. Wakelam, Eric Herbst, J-C J.-C. Loison, I. W. M. Smith, V. Chandrasekaran, B. Pavone, N. G. Adams, M-C M.-C. Bacchus-Montabonel, A. Bergeat, K. Béroff,

V. M. Bierbaum, M. Chabot, A. Dalgarno, E. F. van Dishoeck, A. Faure, W. D. Geppert, D. Gerlich, D. Galli, E. Hébrard, F. Hersant, K. M. Hickson, P. Honvault, S. J. Klippenstein, S. Le Picard, G. Nyman, P. Pernot, S. Schlemmer, F. Selsis, I. R. Sims, D. Talbi, J. Tennyson, J. Troe, R. Wester, and L. Wiesenfeld. a Kinetic Database for Astrochemistry (Kida). *Astrophys. J. Suppl. Ser.*, 199(1):21, mar 2012. ISSN 0067-0049. doi: 10.1088/0067-0049/199/1/21.

Michael D Ward, Isobel a. Hogg, and Stephen D Price. Thermal reactions of oxygen atoms with CS2 at low temperatures on interstellar dust. *Mon. Not. R. Astron. Soc.*, 425(2): 1264–1269, sep 2012. ISSN 00358711. doi: 10.1111/j.1365-2966.2012.21520.x.

M. Wardle and Arieh Konigl. The structure of protostellar accretion disks and the origin of bipolar flows. *Astrophys. J.*, 410:218–238, jun 1993. ISSN 15384357. doi: 10.1086/172739.

Naoki Watanabe and Akira Kouchi. Efficient formation of formaldehyde and methanol by the addition of hydrogen atoms to CO in H2O-CO ice at 10 K. *Astrophys. J.*, 571(2): L173–L176, jun 2002. ISSN 0004637X. doi: 10.1086/341412.

a. Whitworth, Matthew R. Bate, Å. Nordlund, B. Reipurth, and H. Zinnecker. The Formation of Brown Dwarfs: Theory. *Protostars Planets V*, pages 459–476, 2007. doi: 10.1017/S174392130999113X.

K Willacy and W. D. Langer. The Importance of Photoprocessing in Protoplanetary Disks. *Astrophys. J.*, 544:903–920, 2000. ISSN 0004-637X. doi: 10.1086/317236.

David A. Williams and Serena Viti. *Observational Molecular Astronomy*, volume 1. dec 2013. ISBN 9781139087445. doi: 10.1017/CBO9781139087445.

T. L. Wilson and R. T. Rood. Abundances in the Interstellar Medium. *Annu. Rev. Astron. Astrophys.*, 32(1):191–226, sep 1994. ISSN 0066-4146. doi: 10.1146/annurev.aa.32.090194.001203.

Paul M. Woods, A. Occhiogrosso, S. Viti, Z. Kauchová, M. E. Palumbo, and S. D. Price. A new study of an old sink of sulphur in hot molecular cores: The sulphur residue. *Mon. Not. R. Astron. Soc.*, 450(2):1256–1267, jun 2015. ISSN 13652966. doi: 10.1093/mnras/stv652.